

MEASUREMENT OF THE DOUBLE HELICITY ASYMMETRY IN INCLUSIVE  $\pi^0$   
PRODUCTION IN POLARIZED PROTON-PROTON COLLISIONS AT  $\sqrt{s} = 510$  GeV

by

HARI GURAGAIN

Under the Direction of Murad Sarsour, PhD

ABSTRACT

One of the biggest quests in nuclear and particle physics in the last three decades is to unravel the spin structure of hadrons like protons and neutrons. Spin not only plays a central role in the strong force connecting the elementary constituents of matter, but is also responsible for many of its fundamental properties including the magnetic moment which defines the magnetic properties, the different phases in low temperature physics, and the stability of the universe in general. The origin of the spin of particles like protons and neutrons, which make up to 99.9% of the visible universe, has been the focus of experimental and theoretical efforts. Experiments at European Muon Collaboration (EMC) found that our knowledge of how the spin of the nucleon is derived from its elementary constituents is naive, and our interpretations are not valid. This was termed the spin crisis, an outstanding puzzle for more than three decades and is still not solved. Deciphering the spin puzzle requires knowing the spin of elementary constituents of these particles, quarks and gluons.

One of the major objectives of the Relativistic Heavy Ion Collider (RHIC) spin program at Brookhaven National Laboratory is the measurement of the gluon helicity contribution to the proton spin via measuring the double helicity asymmetry ( $A_{LL}$ ) in various channels. In Pioneering High Energy Nuclear Interaction eXperiment (PHENIX) we measure  $A_{LL}$  in  $\pi^0$  meson production. The  $\pi^0$  meson is reconstructed through its di-photon decay channel. The photons are detected by the PHENIX Electromagnetic Calorimeter, which consists of lead glass and lead scintillator detectors and covers a rapidity of  $|\eta| < 0.35$  and azimuthal angle of  $180^\circ$ .

In this dissertation, the results of  $A_{LL}$  in  $\pi^0$  production from the data collected in 2013 at center of mass energy = 510 GeV are presented. In 2013, the total integrated luminosity is  $150 \text{ pb}^{-1}$  which is almost ten times the total luminosity recorded in 2009 at  $\sqrt{s} = 200$  GeV. Due to the increase in the center of mass energy and integrated luminosity, these measurements cover the Bjorken  $x$  range down to  $\sim 0.01$ . A non-zero  $A_{LL}$  result is observed that is consistent with positive gluon polarization in the probed kinematics.

INDEX WORDS: RHIC, PHENIX, Electromagnetic Calorimeter, double helicity asymmetry, gluon polarization

MEASUREMENT OF THE DOUBLE HELICITY ASYMMETRY IN INCLUSIVE  $\pi^0$   
PRODUCTION IN POLARIZED PROTON-PROTON COLLISIONS AT  $\sqrt{s} = 510$  GeV

by

HARI GURAGAIN

A Dissertation Submitted in Partial Fulfillment of the Requirements for the Degree of

Doctor of Philosophy  
in the College of Arts and Sciences  
Georgia State University  
2015

Copyright by  
Hari Guragain  
2015

TITLE: MEASUREMENT OF THE DOUBLE HELICITY ASYMMETRY IN  
INCLUSIVE  $\pi^0$  PRODUCTION IN POLARIZED PROTON-PROTON COLLISIONS at

$$\sqrt{s} = 510 \text{ GeV}$$

by

HARI GURAGAIN

Committee Chair: Murad Sarsour

Committee: Xiaochun He

Douglas R. Gies

A. G. Unil Perera

Megan Connors

Raphael Tieulent

Electronic Version Approved:

Office of Graduate Studies

College of Arts and Sciences

Georgia State University

December 2015

## DEDICATION

To my parents  
and  
wife Shristi

## ACKNOWLEDGEMENTS

First of all, I would like to express my sincere gratitude to my advisor Dr. Murad Sarsour for the continuous support of my PhD study and research, for his patience, motivation, enthusiasm, and immense knowledge of the subject matter. Honestly, I knew very little about the research in high energy physics when I first joined Dr. Sarsour's research group. He encouraged me constantly to be an independent research scientist and helped me working in different projects. He was always ready to explain and help me when I had questions in writing the codes, conducting experiments and analyzing data. I could not have imagined having a better advisor and mentor than him for my PhD study.

I would like to thank my committee members: Dr. Xiaochun He, Dr. Douglas R. Gies, Dr. Unil Perera, Dr. Raphael Tieulent and Dr. Megan Connors for their encouragement, insightful comments and hard questions.

I would also like to thank the Nuclear Physics Group at GSU for their constant help and support through-out the research period. I would like to thank my parents and my wife for all their support, encouragement, quiet patience and unconditional support throughout my endeavour. Finally, I want to thank all of my family members and colleagues who have helped me during the course of my PhD study.

## TABLE OF CONTENTS

	<b>Page</b>
<b>ACKNOWLEDGEMENTS . . . . .</b>	<b>v</b>
<b>LIST OF TABLES . . . . .</b>	<b>x</b>
<b>LIST OF FIGURES . . . . .</b>	<b>xi</b>
<b>LIST OF ABBREVIATIONS . . . . .</b>	<b>xix</b>
<b>CHAPTER 1 INTRODUCTION: STRUCTURE OF THE PROTON . . . . .</b>	<b>1</b>
<b>1.1 Brief History . . . . .</b>	<b>1</b>
<b>1.2 Experimental Techniques: Studying the Structure of Hadrons . . . . .</b>	<b>3</b>
1.2.1 Deeply Inelastic Scattering (DIS) and Proton Structure . . . . .	3
1.2.2 Semi Inclusive Deep Inelastic Scattering (SIDIS) . . . . .	7
1.2.3 Hadron-Hadron Scattering . . . . .	8
1.2.4 Quark Model and QCD (Quantum Chromodynamics) . . . . .	9
<b>1.3 Structure of Proton . . . . .</b>	<b>13</b>
1.3.1 Parton density functions . . . . .	13
1.3.2 Polarized Deep Inelastic Scattering . . . . .	14
1.3.3 Polarized Partons and high-energy proton-proton collisions . . . . .	16
1.3.4 Spin Structure of the Proton . . . . .	18
1.3.5 Longitudinal Double Spin Asymmetry . . . . .	23
<b>1.4 Neutral Pion <math>A_{LL}</math> . . . . .</b>	<b>25</b>
<b>CHAPTER 2 EXPERIMENT . . . . .</b>	<b>26</b>
<b>2.1 Relativistic Heavy Ion Collider (RHIC) Complex . . . . .</b>	<b>26</b>
2.1.1 Polarized Proton Source and Booster . . . . .	27

2.1.2	LINAC . . . . .	28
2.1.3	From Polarized Proton Source to Accelerator . . . . .	28
<b>2.2</b>	<b>Beam Instrumentation</b> . . . . .	29
2.2.1	Siberian Snakes and Spin Rotators . . . . .	29
2.2.2	RHIC Polarimeters . . . . .	32
2.2.3	Spin Rotators . . . . .	34
2.2.4	Different Spin Patterns used in Run 13 . . . . .	34
<b>2.3</b>	<b>PHENIX Detector</b> . . . . .	35
2.3.1	Central Arm Detectors . . . . .	37
2.3.2	Beam-Beam Counters . . . . .	38
2.3.3	Zero Degree Calorimeter and Shower Max Detectors . . . . .	39
2.3.4	EMCal RICH Trigger . . . . .	41
<b>2.4</b>	<b>Tracking</b> . . . . .	41
<b>2.5</b>	<b>Data Acquisition System</b> . . . . .	42
<b>CHAPTER 3 DATA ANALYSIS</b>	. . . . .	<b>44</b>
<b>3.1</b>	<b>Quality Assurance (QA) of Data</b> . . . . .	44
3.1.1	Data Acquisition (DAQ) Condition . . . . .	44
3.1.2	Spin Database . . . . .	44
3.1.3	Polarization . . . . .	45
<b>3.2</b>	<b>EMCal Calibration</b> . . . . .	45
<b>3.3</b>	<b>Event Selection</b> . . . . .	46
<b>3.4</b>	<b>Cluster Rejection Due to Electronic Noise</b> . . . . .	46
3.4.1	Minimum Energy Cut . . . . .	46
3.4.2	Warn/Deadmap . . . . .	47
<b>3.5</b>	<b><math>\pi^0</math> Reconstruction</b> . . . . .	48
<b>3.6</b>	<b>Di-photon Cuts</b> . . . . .	48
<b>3.7</b>	<b>Relative Luminosity</b> . . . . .	51
<b>3.8</b>	<b>Asymmetry Calculations</b> . . . . .	53

3.8.1	Background Fraction . . . . .	55
3.8.2	Luminosity Calculations . . . . .	58
3.8.3	Polarization . . . . .	62
3.8.4	Local Polarimetry at PHENIX . . . . .	66
3.9	Prescales and Run-by-Run Analysis . . . . .	67
<b>CHAPTER 4 SYSTEMATIC UNCERTAINTIES AND CROSS CHECKS</b>		<b>68</b>
4.1	Single Spin Asymmetry . . . . .	68
4.2	Relative Luminosity . . . . .	70
4.2.1	Pileup Correction . . . . .	71
4.2.2	Width Correction . . . . .	73
4.2.3	Residual Rate Correction . . . . .	74
4.2.4	$\Delta A_{LL}$ due to Relative Luminosity . . . . .	76
4.2.5	Summary of Corrections . . . . .	76
4.3	Bunch Shuffling . . . . .	76
4.4	Systematic Uncertainty due to Background Fraction . . . . .	78
4.5	Summary . . . . .	79
<b>CHAPTER 5 RESULTS AND DISCUSSION</b> . . . . .		<b>88</b>
5.1	Signal and Background Yield . . . . .	89
5.1.1	Spin Pattern Separated Yields and Background Fraction . . . . .	89
5.2	Results and Discussion . . . . .	96
5.2.1	Cross-Section . . . . .	96
5.2.2	Double Helicity Asymmetry ( $A_{LL}$ ) Results . . . . .	97
<b>CHAPTER 6 SUMMARY AND CONCLUSION</b> . . . . .		<b>103</b>
6.1	Outlook . . . . .	104
<b>Appendix A DOUBLE HELICITY ASYMMETRY PLOTS</b> . . . . .		<b>113</b>
A.1	Spin Pattern Separated Asymmetries Results . . . . .	113

A.2 Trigger Separated $A_{LL}$ Results . . . . .	118
--	-----

## LIST OF TABLES

Table 2.1	The different spin patterns used in run 13. . . . .	35
Table 3.1	Number of non-edge (hot, dead and uncalibrated) and edge masked towers from “Or” triggered data. The number in the parenthesis is the percentage of the total. W0 to W3 are the sectors in west arm and E0 to E3 are the sectors in east arm. . . . .	47
Table 4.1	Single spin asymmetry values for blue and yellow beams. . . . .	69
Table 4.2	Summary table of all the corrections in the calculation of the uncertainty in relative luminosity. . . . .	77
Table 4.3	Systematic uncertainty due to background fraction calculation: $A_{LL}^{\pi^0}$ at $\sqrt{s} = 510$ GeV. Lower and upper values of systematic uncertainty from background fraction are listed. . . . .	79
Table 4.4	Summary of non-negligible systematic uncertainites in the $A_{LL}$ measurements is presented. The systematic uncertainty due to bunch shuffling with $p_T$ below 12 GeV is negligible. . . . .	84
Table 5.1	Di-photon yields and background fractions for even crossings for different spin patterns. . . . .	89
Table 5.2	Di-photon yields and background fractions for odd crossings for different spin patterns. . . . .	92
Table 5.3	$\kappa$ -factors for the $\pi^0 + BG$ and BG region. . . . .	95
Table 5.4	Mean $p_T$ for each $p_T$ bin. . . . .	96
Table 5.5	Background fraction, $r$ , in the $\pi^0 + BG$ region for even and odd bunch	97
Table 5.6	$A_{LL}^{\pi^0}$ at $\sqrt{s} = 510$ GeV . . . . .	102

## LIST OF FIGURES

Figure 1.1 Parton distribution function for the quarks and gluon. The green dotted line represent the $\bar{u}$ quark, blue dash dotted line represent the $\bar{d}$ quark, red dash line represent the d quark, lower solid line represents the u quark and upper solid line represents the gluon distribution. The data was compiled by particle data group (PDG) [36]. . . . .	2
Figure 1.2 Feynmann diagram of deep inelastic scattering. Here the lepton $l^-$ scattered off the quark of the proton ( $p$ ). . . . .	6
Figure 1.3 Coupling constant $\alpha_s$ corresponding to four flavours and a scale parameter $\Gamma = 0.2 \pm 0.1 \text{ GeV}/c$ ; the dashed, solid and dot-dashes curves correspond to $\Gamma = 0.1, 0.2$ and $0.3$ , respectively. This figure is taken from [19]. . . . .	11
Figure 1.4 Structure function ( $F_2(x, Q^2)$ ) of proton measured from DIS. The data are compiled by particle data group (PDG) [36]. . . . .	12
Figure 1.5 Unpolarized parton distribution function obtained in Next to Next to leading order global analysis at scales $\mu^2 = 10 \text{ GeV}^2$ and $\mu^2 = 10^4 \text{ GeV}^2$ . The data are compiled by particle data group (PDG) [36].	16
Figure 1.6 The world data on $xg_1$ as a function of Bjorken $x$ . The data are compiled by particle data group (PDG) [36] . . . . .	17
Figure 1.7 The parton distribution function for different quarks. The triangle data points are from HERMES experiment, the empty square box data points are from SMC experiment and the filled square box data points are from COMPASS experiment. Similarly, the solid lines are from DSSV2008 [63], the dash lines are from LSS2010 [64] and dot lines are from AAC2008 [65]. . . . .	21

Figure 1.8 NLO polarized parton distributions at the input scale $Q_0^2 = 4.0 \text{ GeV}^2$ (solid line) compared to results obtained by GRSV (dashed-dotted line [47]), DSSV (long dashed-dotted line) [63], AAC (dashed line [49], LSS (long dashed line) [71]. The shaded areas represent the $1\sigma$ bands calculated by Gaussian error propagation. “This fit” represents the fit from [16]. . . . .	22
Figure 1.9 Relative fraction of $\pi^0$ production as a function of $p_T$ in $p+p$ collisions at mid-rapidity. The solid red (online) represents the contribution from the gluon-gluon scattering, dashed black represents the contribution from the gluon-quark scattering and dotted green (online) represents the contribution from the quark-quark scattering. The figure is from [52]. . . . .	25
Figure 2.1 Sketch of the Relativistic Heavy Ion Collider complex including AGS Booster, the AGS, and the RHIC [25]. . . . .	27
Figure 2.2 View of RHIC ring showing the location of the Siberian Snakes and the spin rotators placed around the collider experiments STAR and PHENIX. The polarization directions around the rings and around the detectors for collisions with longitudinal polarization are also shown [17]. . . . .	29
Figure 2.3 The polarization direction and path of a polarized proton bunch passing through a full Siberian snake [17]. . . . .	31
Figure 2.4 Beam view of $pC$ polarimeter. The center is the carbon target and the beam is incident into it. Recoil Carbon atoms are measured with 6 silicon strip detectors (red) online [74]. . . . .	33
Figure 2.5 General layout of H-Jet polarimeter. This figure is taken from [74].	33
Figure 2.6 Layout of Phenix Detector. Top is the central arm and the bottom is the muon arm. . . . .	36

Figure 2.7 Mechanical design of the Tungsten Modules of Zero Degree Calorimeter [32]. . . . .	40
Figure 3.1 Time of flight distribution before and after applying the cuts. . . . .	50
Figure 3.2 Charge veto angle as a function of energy of cluster. Red full circles are for large veto angle and blue empty circles are for small veto angle. The solid red and dashed blue curves are from fit. The clusters within the two curves are excluded in this analysis. . . . .	52
Figure 3.3 Invariant mass spectrum of $\pi^0$ . The signal region is represented by solid red region ( $0.112 \leq M_{\gamma\gamma} \leq 0.162 \text{ GeV}/c^2$ ). The background region is represented by shaded blue pattern region ( $0.047 \leq M_{\gamma\gamma} \leq 0.097 \text{ GeV}/c^2$ and $0.177 \leq M_{\gamma\gamma} \leq 0.227 \text{ GeV}/c^2$ ) . . . . .	54
Figure 3.4 BW method to calculate the background fraction for even crossing. Here red dashed curve is the Gaussian + BW function and blue dotted line is the third order polynomial function. . . . .	56
Figure 3.5 BW method to calculate the background fraction for odd crossing. Here red dashed curve is the Gaussian + BW function and blue dotted line is the third order polynomial function. . . . .	57
Figure 3.6 GPR approach to calculate the background fraction for even crossing. Here the solid blue circles represent the invariant mass histogram, the empty green circles represent the extrapolate/interpolate values using GPR and the red square boxes represent the input data points. . . . .	58
Figure 3.7 GPR approach to calculate the background fraction for odd crossing. Here the solid blue circles represent the invariant mass histogram, the empty green circles represent the extrapolate/interpolate values using GPR and the red square boxes represent the input data points. . . . .	59

Figure 3.8 Comparison of the background fraction calculated by using GPR and Breit Weigner method for even crossing as a function of $p_T$ . Here the red solid circles are from GPR method and the empty blue circles are from the Breit Weigner method. . . . .	60
Figure 3.9 Comparison of the background fraction calculated by using GPR and Breit Weigner method for odd crossing as a function of $p_T$ . Here the red solid circles are from GPR method and the empty blue circles are from the Breit Weigner method. . . . .	61
Figure 3.10 Polarization calculation procedure at mid-time of the run. . . . .	63
Figure 3.11 Blue beam polarization as a function of run number. . . . .	64
Figure 3.12 Yellow beam polarization as a function of run number. . . . .	65
Figure 4.1 Single spin asymmetry as function of $p_T$ for blue and yellow beams.	69
Figure 4.2 $A_{LL}^{ZDC}$ as a function of run number. The central red line is a fit with a zeroth-order polynomial. No corrections have been applied in this plot. . . . .	71
Figure 4.3 BBC rate with and without Pileup correction. For BBC, scaler undercounting is dominant at high rate. . . . .	72
Figure 4.4 ZDC rate with and without Pileup correction. For ZDC, scaler overcounting is dominant at high rate. . . . .	72
Figure 4.5 $A_{LL}^{ZDC/BBC}$ as a function of run number with pileup correction. Both $A_{LL}^{ZDC/BBC}$ and $\chi^2_{re}$ are reduced compared with no corrections as shown in the Figure 4.2. . . . .	73
Figure 4.6 $A_{LL}^{ZDC/BBC}$ as a function of run number with pileup and width correction. Both $A_{LL}^{ZDC/BBC}$ and $\chi^2_{re}$ are reduced compared with no corrections as shown in Figure 4.2. . . . .	74
Figure 4.7 $C_{res}$ of BBC as a function of observed vertex cut rate of BBC. . .	76
Figure 4.8 $C_{res}$ of ZDC as a function of observed vertex cut rate of ZDC. . .	76

Figure 4.9 $A_{LL}^{ZDC/BBC}$ as a function of run number with pileup, width and residual rate corrections. $A_{LL}^{ZDC/BBC}$ is a bit increased. However $\chi^2_{re}$ are dramatically reduced compared with no corrections as shown in Figure 4.2.	77
Figure 4.10 $\chi^2/NDF$ from 600000 bunch shuffled samples from even bunches for $A_{LL}^{\pi^0+BG}$ . The red dash curves are from the theoretical $\chi^2$ fit.	80
Figure 4.11 $\chi^2/NDF$ results from 600000 bunch shuffled samples from odd bunches for $A_{LL}^{\pi^0+BG}$ . The red dash curves are from the theoretical $\chi^2$ fit.	81
Figure 4.12 $\chi^2/NDF$ results from 600000 bunch shuffled samples from even bunches for $A_{LL}^{BG}$ . The red dash curves are the from the theoretical $\chi^2$ fit.	82
Figure 4.13 $\chi^2/NDF$ results from 600000 bunch shuffled samples from odd bunches for $A_{LL}^{BG}$ . The red dash curves are from the theoretical $\chi^2$ fit.	83
Figure 4.14 The distribution of $A_{LL}^{\pi^0+BG}/\sigma$ for even bunches from the bunch shuffling. The red dash curves show Gaussian fit.	84
Figure 4.15 The distribution of $A_{LL}^{\pi^0+BG}/\sigma$ for odd bunches from the bunch shuffling. The red dash curves show Gaussian fit.	85
Figure 4.16 The distribution of $A_{LL}^{BG}/\sigma$ for even bunches from the bunch shuffling. The red dash curves show Gaussian fit.	86
Figure 4.17 The distribution of $A_{LL}^{BG}/\sigma$ for odd bunches from the bunch shuffling. The red dash curves show Gaussian fit.	87

Figure 5.1 (color online). The neutral pion production cross section at $\sqrt{s} = 510$ GeV as a function of $p_T$ and the results of NLO pQCD calculations for theory scales $\mu = p_T / 2$ (dotted line), $p_T$ (solid line) and $2p_T$ (dashed line), with $\mu$ representing equal factorization, renormalization, and fragmentation scales. Note that the error bars, representing the combined statistical and point-to-point systematic uncertainties, are smaller than the points. The bottom panel shows the relative difference between the data and theory for the three theory scales. Experimental uncertainties are shown for the $\mu = p_T$ curve. . . . .	98
Figure 5.2 $A_{LL}$ vs $p_T$ for $\pi^0$ production at mid-rapidity at $\sqrt{s} = 510$ GeV from run 13. . . . .	99
Figure 5.3 $A_{LL}$ vs $p_T$ for $\pi^0$ production at mid-rapidity at $\sqrt{s} = 510$ GeV. Shift uncertainty from relative luminosity is shown at $A_{LL} = 0$ . Theoretical curve with 90% C.L. band is DSSV14 calculation [70]. . . . .	100
Figure 5.4 $A_{LL}$ vs $x_T$ for $\pi^0$ production at mid-rapidity at $\sqrt{s} = 200$ GeV from [68] and $\sqrt{s} = 510$ GeV from this analysis. Note that the shift uncertainties from two data samples are about the same, hence indistinguishable in this plot. Theoretical curves are from recent NLO global analyses [64, 59, 70]. . . . .	101
Figure 6.1 Gluon helicity distribution at $Q^2 = 10$ GeV $^2$ . The dotted lines represent the gluon densities for alternative fits that are within the 90% C.L. limit [70]. . . . .	104
Figure 6.2 Change of the $\Delta\chi^2$ profile of the truncated first moment of $\Delta g$ in the $x$ -range with $Q^2$ . The solid lines at the base of the plot indicate the 90% C.L. interval [70]. . . . .	105

Figure 6.3 Variation of total $\chi^2$ of the fit as a function of the truncated first moment of $\Delta g$ in the $x$ -range $\sim [0.01 - 0.05]$ . The results obtained from $\sqrt{s} = 510$ GeV is compared with the DSSV14 results [70]. This calculation is from [77]. . . . .	106
Figure 6.4 Accuracies for the correlated truncated integrals of $\Delta\Sigma$ and $\Delta g$ over $0.001 \leq x \leq 1$ , on the basis of the DSSV+ analysis (outer area) and projected for an EIC (inner areas) [78]. . . . .	107
Figure A.1 Double spin asymmetry for spin patterns SOOSSO and even crossing, signal region. . . . .	114
Figure A.2 Double spin asymmetry for spin patterns SOOSSO and even crossing, background region. . . . .	115
Figure A.3 Double spin asymmetry for spin patterns SOOSSO and odd crossing, signal region. . . . .	116
Figure A.4 Double spin asymmetry for spin patterns SOOSSO and odd crossing, background region. . . . .	117
Figure A.5 Double spin asymmetry for spin patterns OSSOOSS and even crossing, signal region. . . . .	119
Figure A.6 Double spin asymmetry for spin patterns OSSOOSS and even crossing, background region. . . . .	120
Figure A.7 Double spin asymmetry for spin patterns OSSOOSS and odd crossing, signal region. . . . .	121
Figure A.8 Double spin asymmetry for spin patterns OSSOOSS and odd crossing, background region. . . . .	122
Figure A.9 Double spin asymmetry for spin patterns SSOO and even crossing, signal region. . . . .	123
Figure A.10 Double spin asymmetry for spin patterns SSOO and even crossing, background region. . . . .	124

Figure A.11 Double spin asymmetry for spin patterns SSOO and odd crossing, signal region. . . . .	125
Figure A.12 Double spin asymmetry for spin patterns SSOO and odd crossing, background region. . . . .	126
Figure A.13 Double spin asymmetry for spin patterns OOSS and even crossing, signal region. . . . .	127
Figure A.14 Double spin asymmetry for spin patterns OOSS and even crossing, background region. . . . .	128
Figure A.15 Double spin asymmetry for spin patterns OOSS and odd crossing, signal region. . . . .	129
Figure A.16 Double spin asymmetry for spin patterns OOSS and odd crossing, background region. . . . .	130
Figure A.17 Double spin asymmetry for different spin patterns for 4x4a trigger and even crossing. . . . .	131
Figure A.18 Double spin asymmetry for different spin patterns for 4x4a trigger and odd crossing. . . . .	132
Figure A.19 Double spin asymmetry for different spin patterns for 4x4b trigger and even crossing. . . . .	133
Figure A.20 Double spin asymmetry for different spin patterns for 4x4b trigger and odd crossing. . . . .	134
Figure A.21 Double spin asymmetry for different spin patterns for 4x4c trigger and even crossing. . . . .	135
Figure A.22 Double spin asymmetry for different spin patterns for 4x4c trigger and odd crossing. . . . .	136

## LIST OF ABBREVIATIONS

- GSU - Georgia State University
- BNL - Brookhaven National Laboratory
- PHENIX - Pioneering High Energy Nuclear Interaction Experiment
- RHIC - Relativistic Heavy Ion Collider
- COMPASS - COmmon Muon Proton Apparatus for Structure and Spectroscopy
- DESY - Deutsches Elektronen-Synchrotron
- QCD - Quantum Chromodynamics
- QED - Quantum Electrodynamics
- SLAC - Stanford Linear Accelerator Center
- CERN - European Organization for Nuclear Research
- EMC - European Muon Collaboration
- DIS - Deep Inelastic Scattering
- $p_T$  - Transverse Momentum
- PDG - Particle Data Group
- LHC - Large Hadron Collider
- $p + p$  - proton-proton
- STAR - Solenoidal Tracker at RHIC

## CHAPTER 1

### INTRODUCTION: STRUCTURE OF THE PROTON

#### 1.1 Brief History

The history of the strong interaction begun in mid 1960, when quarks were introduced to explain the group of strongly interacting particles that had been discovered from accelerator experiments [1]. The color quantum number was needed to describe particles such as the  $\Omega^-$ , a state of three strange quarks, each with the same spin  $\frac{1}{2}$  adding to a total spin of  $\frac{3}{2}$  [3]. In late 1960, an experiment at the Stanford Linear Accelerator Center (SLAC) showed that these quarks were real [4, 5, 6]. In the early 1970s, the theory of Quantum Chromodynamics (QCD) was developed with quarks, gluons, and color charge; perturbative QCD could be used for precise calculations of hard scattering. From the 1980s to the present, electron-proton and antiproton-proton colliders have carried out beautiful precision tests of unpolarized perturbative QCD predictions. Similarly the polarized studies of the strong interaction is also closely related to SLAC. In the 1960s, a polarized electron source, PEGGY, which was developed at Yale University, was brought to SLAC to initiate a program to explore the structure of the proton with the polarized beam and target [7]. A polarized electron probes a polarized proton through the absorption of polarized photons with known helicity<sup>1</sup>. Quarks in the proton with opposite helicity to that of the photon flip spin when the photon is absorbed. Quarks with the same helicity cannot absorb the photon. Thus, one accesses the spin structure of the proton. The first results showed a strong correlation of the quark spins with that of the proton [7]. This was expected from the simple quark model of the proton developed in 1970s [8]. These experiments studied quarks which carried a large fraction ( $x$ ) of the momentum of the protons. Later, in 1988, the European Muon Collaboration at CERN reported this correlation for lower  $x$  quarks [9]. The EMC experiment discovered

---

<sup>1</sup>Projection of spin along the direction of momentum

that little of the proton spin was carried by the quarks, on average, which was a major surprise. Measurements with electron and muon probes continue through today from several experiments [11, 12, 13, 14]. These experiments have confirmed that only a small fraction of the proton spin is carried by the quarks. The distribution functions for quarks and gluons at different momentum fraction are shown in Figure 1.1. From this figure, it can be seen that

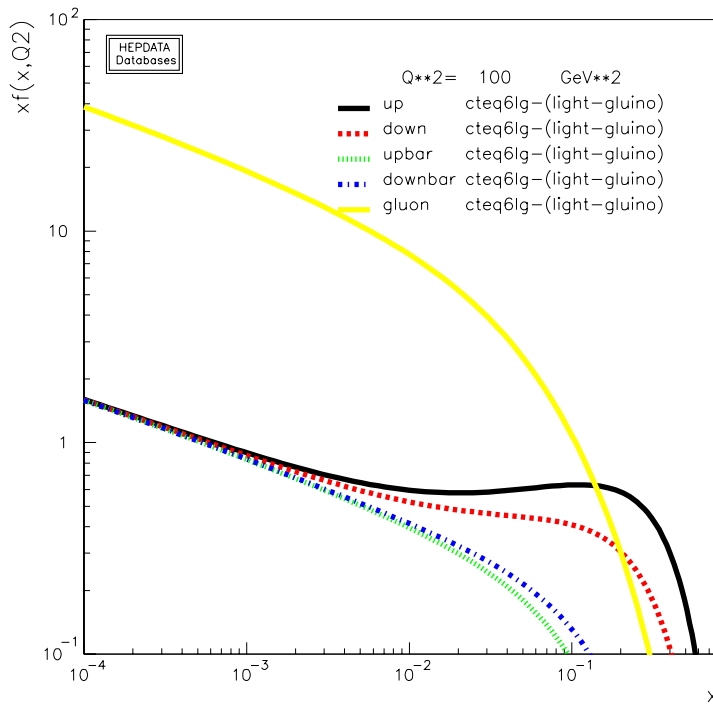


Figure (1.1) Parton distribution function for the quarks and gluon. The green dotted line represent the  $\bar{u}$  quark, blue dash dotted line represent the  $\bar{d}$  quark, red dash line represent the d quark, lower solid line represents the u quark and upper solid line represents the gluon distribution. The data was compiled by particle data group (PDG) [36].

at lower  $x$ , the gluonic distribution function dominates. The focus was then diverted to the gluonic contribution to the total spin of proton. Starting in 2001, the Relativistic Heavy Ion Collider (RHIC) at Brookhaven National Laboratory (BNL) collided polarized protons to measure the gluonic contribution to the spin of the proton. The polarized protons provided strongly interacting probes which can interact directly with the gluons as well as the quarks in the proton and allow direct measurement of the gluon contribution [15, 17].

## 1.2 Experimental Techniques: Studying the Structure of Hadrons

Understanding the proton structure requires understanding of the basic properties of the proton such as charge, momentum, spin, etc. Since quarks and gluons are the constituents of the proton, understanding those properties necessitate understanding the quarks and gluons which make up the proton. In order to achieve this goal, several experimental techniques are employed.

### 1.2.1 Deeply Inelastic Scattering (DIS) and Proton Structure

The first of a long series of experiments on highly inelastic electron scattering was carried out in late 60s at SLAC using liquid hydrogen and, later, liquid deuterium targets. The primary objective of this experiment was to look at the energy transfer during the scattering of electrons from the nucleon. This process is termed as deep inelastic scattering. Deep inelastic scattering has been described in numerous text books: [2, 19, 20]. The original experiments of this type in particle physics were done in the 1960s and showed that nucleons have a sub-structure of point-like charged constituents; the first evidence for the existence of quarks [18]. The idea behind the deep inelastic scattering is to accelerate electrons to a very high energies, then allow them to interact with stationary protons and neutrons.

At high energies, the wavelengths associated with the electrons are much smaller than size of a proton. This allows probing distances that are small compared with the proton, that is, deep inside the proton. But due to the high energies the proton will be broken apart

and produce several new particles called hadrons. Since the target has been changed in this process it is called inelastic scattering.

To find the amplitude of the electron-nucleus scattering, we should in principle solve the Schrodinger (or Dirac) equation using a Hamiltonian that includes the full electromagnetic interaction and use nuclear wavefunctions. The Rutherford cross-section, which comes from the electron-nucleon scattering, in its relativistic form may be written in the following Equation:

$$\frac{d\sigma}{d\Omega_{Rutherford}} = \frac{Z^2 \alpha^2 (\hbar c)^2}{4E^2 \sin^4(\frac{\theta}{2})}, \quad (1.1)$$

where  $E$  is the total initial energy of the projectile,  $\theta$  is the angle through which it is scattered,  $Z$  is the atomic number and  $\alpha = \frac{e^2}{4\pi\epsilon_0\hbar c}$ ,  $e$  is the charge,  $\hbar$  is the plank's constant and  $c$  is the speed of light.

Equation 1.1 represents the scattering of a spinless (spin 0) point - like projectile of unit charge from a fixed point-like target with electric charge  $Ze$ , i.e., the charge distribution of the target is neglected. In order to take the electron's helicity state into account Equation 1.1 can be modified into Mott cross-section [10]:

$$\frac{d\sigma}{d\Omega_{Mott}} = \frac{d\sigma}{d\Omega_{Rutherford}} [1 - \beta^2 \sin^2(\frac{\theta}{2})], \quad (1.2)$$

where  $\sin^2(\theta/2)$  arises from averaging the spin over all the electrons,  $\beta = \frac{v}{c}$  and  $v$  is the velocity of the initial electron. At higher energies the recoil of the target needs to be taken into account and this introduces a factor of  $\frac{E'}{E}$  on the right-hand side of Equation 1.2, where  $E'$  is the final energy of the electron. We also need to account for interaction with the magnetic moment of the target in addition to its charge. With this the final form of the differential cross-section is:

$$\frac{d\sigma}{d\Omega} = \frac{d\sigma}{d\Omega_{Mott}} \frac{E'}{E} [1 + 2\tau \tan^2 \frac{\theta}{2}], \quad (1.3)$$

where

$$\tau = -\frac{q^2}{4M^2c^2} \quad (1.4)$$

and  $M$  is the mass of the target. Because the energy loss of the electron to the recoiling nucleus is no longer negligible, the momentum transfer ( $\mathbf{q}$ ), has been replaced by the four-momentum transfer  $\mathbf{q}$  whose square is

$$\mathbf{q}^2 = (\mathbf{p} - \mathbf{p}')^2 = 2m_e^2c^2 - 2(EE'/c^2 - |\mathbf{p}'| |\mathbf{p}| \cos \theta) \approx -\frac{4EE'}{c^2} \sin^2(\frac{\theta}{2}), \quad (1.5)$$

where  $\mathbf{p}$  ( $\mathbf{p}'$ ) is the four-momentum before (after) scattering. (Because  $\mathbf{q}^2 \leq 0$ , it is common practice to replace it with  $Q^2 = -q^2$  so as to work with positive quantities). The final modification is due to the spatial extension of the nucleus. If the spatial charge distribution within the nucleus is written as  $f(\mathbf{x})$  then we define the form factor  $F(q^2)$  [2] by

$$F(\mathbf{q}^2) \equiv \frac{1}{Ze} \int e^{iq \cdot \mathbf{x}/\hbar} f(\mathbf{x}) d^3\mathbf{x} \text{ with } Ze = \int f(\mathbf{x}) d^3\mathbf{x}, \quad (1.6)$$

i.e., the Fourier transform of the charge distribution. In the case of a spherically symmetric charge distribution, the angular integrations in Equation 1.6 may be done using spherical polar coordinates to give

$$F(\mathbf{q}^2) = \frac{4\pi\hbar}{Zeq} \int_0^\infty r \rho(r) \sin(\frac{qr}{\hbar}) dr, \quad (1.7)$$

where  $q = |\mathbf{q}|$  and  $\rho(r)$  is the radial charge distribution. The final form of the experimental cross-section in this approximation is given by

$$(\frac{d\sigma}{d\Omega})_{exp} = (\frac{d\sigma}{d\Omega})_{Mott} |F(\mathbf{q}^2)|^2. \quad (1.8)$$

The above procedure is good for a low energy lepton scattered off a proton in which the determination of the radial charge distributions is made. In a similar way we can use high-energy inelastic scattering to investigate the charge distribution within nucleons. This is

referred to as deep inelastic scattering (DIS), because the projectiles probe deep into the internal structure of the nucleon. The dominant one-photon contribution to the inelastic scattering of a charged lepton from a proton in the spectator quark model<sup>2</sup> is illustrated in Figure 1.2. Unlike elastic scattering where at a given lepton energy  $E$  there is only one

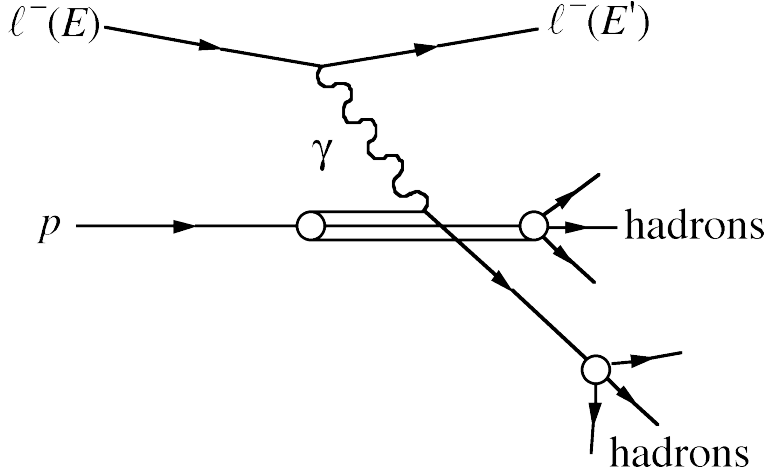


Figure (1.2) Feynmann diagram of deep inelastic scattering. Here the lepton  $l^-$  scattered off the quark of the proton ( $p$ ).

free variable (e.g. the scattering angle), in inelastic scattering the excitation energy of the nucleon adds more degrees of freedom, so we can define two independent variables  $v$  and  $x$  that are given by Equations 1.9 and 1.10 [36]

$$2Mv \equiv W^2c^2 + Q^2 - M^2c^2, \quad (1.9)$$

$$x \equiv Q^2/2Mv. \quad (1.10)$$

where,  $M$  is the proton mass,  $W$  is the invariant mass of the final-state hadrons and  $Q^2$  is the squared energy-momentum transfer:

$$Q^2 = (E - E')^2/c^2 - (\mathbf{p} - \mathbf{p}')^2. \quad (1.11)$$

---

<sup>2</sup>In this model, a baryon is described as a three-constituent quark system where one quark is free to interact with the photon field, and a pair of noninteracting quarks is treated as a single on-mass-shell spectator diquark with certain effective mass

In the rest frame of the initial proton,  $v$  reduces to

$$v = E - E' \quad (1.12)$$

which is the Lorentz-invariant generalization for the energy transferred from the lepton to the proton.

In case of low energy scattering experiments, we have considered different factors which contribute to the cross section calculation. The magnetic interaction also introduces another form factor in case of high energy scattering.

The differential cross-section in terms of form factors can be written as

$$\frac{d^2\sigma}{d\Omega dE'} = \left(\frac{d\sigma}{d\Omega}\right)_{Mott} [W_2(Q^2, v) + 2W_1(Q^2, v) \tan^2(\theta/2)], \quad (1.13)$$

The two form factors denoted by  $W_1$  and  $W_2$  in Equation 1.13 are called structure functions, also,  $\theta$  is the lepton scattering angle. For values of  $W \leq 2.5$  GeV/ $c^2$ , the cross-sections show considerable structure due to the excitation of nucleon resonances, but above this mass they are smoothly varying. In the latter region, the values of the structure functions can be extracted from the data by choosing suitable parameterizations and fitting the available data in an analogous way to the way charge distributions of nuclei were deduced. However, additional information is needed to learn about the struck quark in the hadron. This is achieved by what is called semi inclusive deep inelastic scattering.

### 1.2.2 Semi Inclusive Deep Inelastic Scattering (SIDIS)

Semi-inclusive DIS (SIDIS) is similar to DIS, except that (at least) one hadron in the final state is observed. Since the leading hadrons from any fragmentation are detected, it can give a clue about the struck quark within the hadron. In this process, it is assumed that

the timescale for the absorption of a virtual photon is very short compared to the timescale needed for the quark to fragment into a hadron. The fragmentation process is not calculable in perturbative Quantum Chromodynamics (pQCD) since it involves long distance processes and thus corresponds to very low  $Q^2$  values where pQCD techniques cannot be used.

The fragmentation process in semi-inclusive scattering is parameterized by fragmentation functions  $D_f^h(Q^2, z)$ , which represent the probability that a quark of flavor  $f$  fragments into a hadron of type  $h$  with a fraction  $z$  of the virtual photon energy ( $E_h = zv$ ). The kinematic dependence of the fragmentation function involves only  $Q^2$ , which represents the effect arising from gluon radiation of the struck quark, similar to the scaling violations for the structure functions. In the quasiparticle-phonon model (QPM) the cross section for the process  $e + N \rightarrow e + h + X$  is assumed to be the product of the differential inclusive cross section and the fragmentation probability of finding a hadron  $h$  originating from a quark of any flavor  $f$  [21].

$$\frac{d^3\sigma(eN \rightarrow ehX)}{dxdQ^2dz} = \frac{d^2\sigma(eN \rightarrow eX)}{dxdQ^2} \frac{\Sigma_f e_f^2 q_f(x, Q^2) D_f^h(Q^2, z)}{\Sigma_f e_f^2 q_f(x, Q^2)}, \quad (1.14)$$

Here, it is assumed that the quasi-free scattering process (related to the quark momentum distribution  $q_f(x)$  and the fragmentation process (described by the fragmentation function,  $D_f^h(z)$ ) enter as two independent factors in the cross section (at the flavor level). This is known as factorization.

### 1.2.3 Hadron-Hadron Scattering

Hadron-hadron scattering is another approach to understand the nucleon structure. In this process, quarks and gluons interact at leading order. The basic interaction considered in this work is  $p + p \rightarrow X$ . However, in proton-proton ( $p + p$ ) inelastic scattering, as neither the proton nor the remnant is measured, a final state created in the interaction (for example, a hadron  $h$ , a jet, or a direct photon) is observed. In all measurements discussed in this work,

we assume only one final state particle (or jet), and so  $D_D^d(z, Q^2)$  is included in the sum over  $X$ . As both incoming particles are protons, there are two PDFs contributing to the cross section

$$\sigma^{p+p \rightarrow h+X} = \sum_{f_{a,b}=q,\bar{q},g} f_a(x_a, Q^2) \otimes f_b(x_b, Q^2) \otimes \hat{\sigma}^{a+b \rightarrow c+X}(x_a P_1, x_b P_2, q, z P_c) \otimes D_h^c(z, Q^2). \quad (1.15)$$

In this equation, the observable in final state is assumed to be a hadron. In this work, the final state observable is neutral pion ( $\pi^0$ ). A drawback of  $p+p$  collisions is that neither  $x$  nor  $Q^2$  are directly measured in the interaction. Instead, for the requisite hard scale needed for theoretical interpretation (normally  $\mu^2 = Q^2$  in DIS and SIDIS), the transverse momentum,  $p_T$ , of the measured probe is used.

#### 1.2.4 Quark Model and QCD (Quantum Chromodynamics)

**Asymptotic Freedom and QCD** The strong interaction derives its name from the force that, among other things, binds quarks into hadrons. However, some remarkable phenomena depend on the fact that the interaction gets weaker at short distances; that is, on asymptotic freedom which can be interpreted as “quarks are born free, but everywhere they are in chains”. The short-distance interactions lead to large momentum transfers  $|\mathbf{q}|$  between the particles, with  $|\mathbf{q}| = O(\hbar/r)$ , where  $r$  is the distance at which the interaction occurs. The strength of the interaction, in general depends on the four-momentum transfer as:

$$Q^2 \approx E_q^2/c^2 - q^2, \quad (1.16)$$

In QCD, the coupling constant  $\alpha_s$  is given by [23]

$$\alpha_s(Q^2) = \frac{12\pi}{(33 - 2N_f) \ln(Q^2/\Gamma^2)}, \quad (1.17)$$

where  $N_f$  is the number of quark flavours up: ( $u$ ), down ( $d$ ), charm ( $c$ ), strange ( $s$ ), top ( $t$ ) and bottom ( $b$ ) with  $4m_q^2 c^4 < Q^2$ , and  $Q^2 \gg \Gamma^2$ .  $\Gamma$  is a constant called the scale parameter

and is determined from experiments. From Equation 1.17, it is seen that  $\alpha_s$  is not constant but has inverse relationship with  $Q^2$ .

If the distance between the two quarks is increased, the force between them increases which is different behaviour from that of a force between particles connected by a spring. If the force applied to the two particles is sufficiently large, the spring will break and the particles will be free. But in case of hadrons, the energy stored in the color field increases until it becomes sufficiently large to create  $q\bar{q}$  pairs and eventually combinations of these will appear as physical hadrons. This process is called fragmentation and is of immense interest for the physicists who study the strong interaction. Quantum fluctuations also exist in QCD and give rise to variation in the interaction strength with distance of the interaction. As antiscreening effect<sup>3</sup> is larger than the screening effect so the net effect is that the interaction grows weaker at short distances hence the term asymptotic freedom. With this effect, the strong interaction coupling  $\alpha_s$  given by Equation 1.17 is now modified as [2]:

$$\alpha_s(Q^2) = \frac{\alpha_s(\mu^2)}{1 + \frac{\alpha_s(\mu^2)}{12\pi}(33 - 2N_f)\ln(Q^2/\mu^2)}, \quad (1.18)$$

where  $\mu^2$  is a low-energy value of  $Q^2$  at which the value of  $\alpha_s$  is known and  $N_f$  is the number of quark flavors that take part in the interaction. The coupling constant of the proton as a function of  $Q^2$  is shown in Figure 1.3. Similarly, the structure function of proton measured from Deep Inelastic Scattering (DIS) is shown in Figure 1.5. Here the values are for different Bjorken  $x$ -ranges. In the parton model, we imagine hadrons as extended objects, made up of constituents (partons) held together by their mutual interactions. Of course, these partons are the quarks and gluons in the real world, as described by QCD, but we do not use this fact yet. At the level of the parton model, we assume that the hadrons can be described in terms of virtual partonic states, but that we are not in a position to calculate the structure of

---

<sup>3</sup>In the vicinity of a charge, any vacuum surrounding it becomes polarized: virtual particles of opposing charge are attracted to the charge, and virtual particles of like charge are repelled. The net effect is to partially cancel out the field at any finite distance. Getting closer and closer to the central charge, one sees less and less of the effect of the vacuum, and the effective charge increases. In QCD the virtual quark-antiquark pairs tend to screen the color charge.

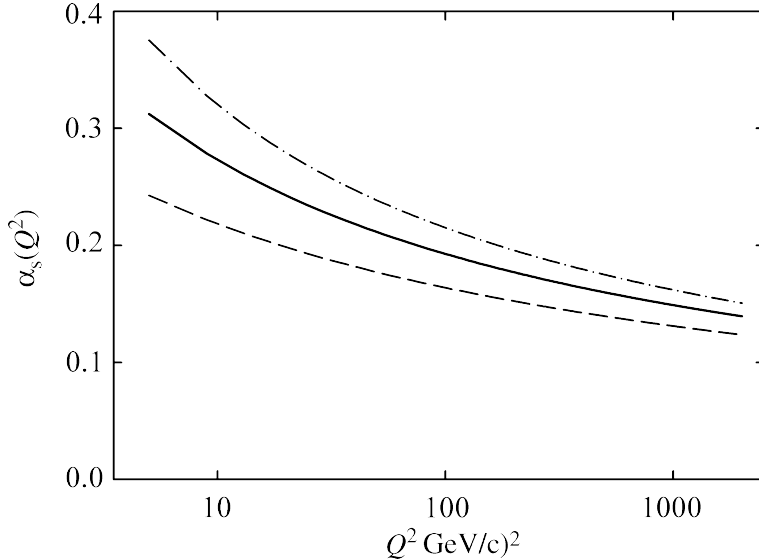


Figure (1.3) Coupling constant  $\alpha_s$  corresponding to four flavours and a scale parameter  $\Gamma = 0.2 \pm 0.1$  GeV/c; the dashed, solid and dot-dashes curves correspond to  $\Gamma = 0.1, 0.2$  and  $0.3$ , respectively. This figure is taken from [19].

these states. On the other hand, we assume that we do know how to compute the scattering of a free parton by, say, an electron. By free, we simply mean that we neglect parton-parton interactions. This dichotomy of ignorance and knowledge corresponds to our inability to compute perturbatively at long distances in QCD, while having asymptotic freedom at short distances. To be specific, consider inclusive electron-hadron scattering by virtual photon exchange at high energy and momentum transfer. Consider how this scattering looks in the center-of-mass frame, where two important things happen to the hadron. It is Lorentz contracted in the direction of the collision, and its internal interactions are time dilated. So, as the center-of-mass energy increases the lifetime of any virtual partonic state is lengthened, while the time it takes the electron to traverse the hadron is shortened. When the latter is much shorter than the former, the hadron will be in a single virtual state characterized by a definite number of partons during the entire time the electron takes to cross it. Since the partons do not interact during this time, each one may be thought of as carrying a definite fraction  $x$  of the hadron's momentum in the center of mass frame. We expect  $x$  to satisfy  $0 < x < 1$ , otherwise one or more partons would have to move in the opposite direction to the

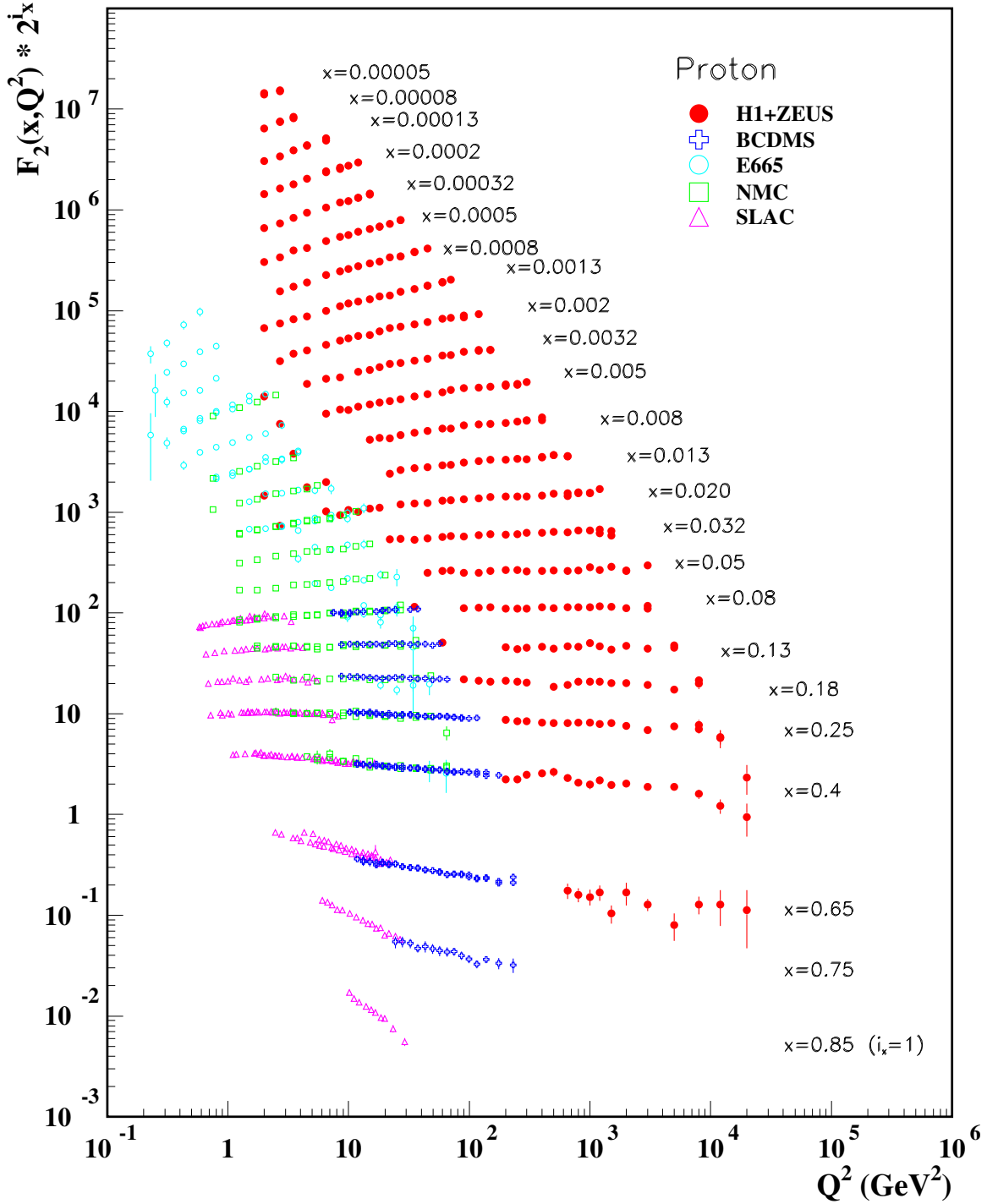


Figure (1.4) Structure function ( $F_2(x, Q^2)$ ) of proton measured from DIS. The data are compiled by particle data group (PDG) [36].

hadron, an unlikely configuration. It now makes sense to talk about the electron interacting with partons of definite momentum, rather than with the hadron as a whole. In addition, when the momentum transfer is very high, the virtual photon which mediates electron-parton scattering cannot travel far. Then, if the density of partons is not too high, the electron will be able to interact with only a single parton. Also, interactions which occur in the final state, after the hard scattering, are assumed to occur on time scales too long to interfere with it. With these assumptions, the high energy scattering process becomes essentially classical and incoherent. That is, the interactions of the partons among themselves, which occur at time-dilated time scales before or after the hard scattering, cannot interfere with the interaction of a parton with the electron. The cross section for hadron scattering may thus be computed by combining probabilities, rather than amplitudes. We define a parton distribution  $f_{a/H}(\xi)$  as the probability that the electron will encounter a frozen, non-interacting parton of species  $a$  with fraction  $\xi$  of the hadron's momentum. We take the cross section for the electron to scatter from such a parton with momentum transfer  $Q^2$  as the Börn cross section  $\sigma_B(Q^2, \xi)$ . Straightforward kinematics shows that for free partons  $\xi > x \equiv 2 p q / Q^2$ , and the total cross section for deeply inelastic scattering of a hadron by an electron is

$$\sigma_{eH}(x, Q^2) = \sum_a \int_x^1 d\xi f_{a/H}(\xi) \sigma_B(x/\xi, Q^2). \quad (1.19)$$

### 1.3 Structure of Proton

To understand the structure of the proton, the experimental techniques described in the previous sections are used. In the coming sections, the charge, momentum and spin of the proton will be discussed.

#### 1.3.1 Parton density functions

The proton is composed of three valence quarks which are denoted by  $q_v$ . Two of them are known as up quarks and one is the down quark. They are primarily responsible for determining the properties of a hadron. It can however occur (in particular at high  $Q^2$ ,

corresponding to a high resolution) that a valence quark radiates a gluon which then splits into a quark-antiquark pair which is then probed by the virtual photon. These quarks are referred to as sea quarks and are denoted by  $q_s$ . Summing over the measured momenta of the partons should give the proton momentum.

$$\int_0^1 dx x(u + \bar{u} + d + \bar{d} + s + \bar{s}) = 1, \quad (1.20)$$

But experimental data [20], neglecting the contribution of strange quarks, show that,

$$\int_0^1 dx F_2^{ep} = \frac{4}{9}\epsilon_u + \frac{1}{9}\epsilon_d = 0.18, \quad (1.21)$$

$$\int_0^1 dx F_2^{en} = \frac{1}{9}\epsilon_u + \frac{4}{9}\epsilon_d = 0.12 \quad (1.22)$$

where  $F_2^{ep}$  and  $F_2^{en}$  are the structure functions of proton and neutron, respectively. By solving the above equations we can see that:  $\epsilon_u = 0.36$  and  $\epsilon_d = 0.18$ , and the fraction of the momentum of the proton not carried by quarks is:  $\epsilon_g = 1 - \epsilon_u - \epsilon_d = 0.46$ . Almost half of the proton momentum is carried by electrically uncharged partons. By repeating the scattering experiments with neutrinos instead of electrons, one observes that these uncharged partons do not interact weakly either. The parton carrying the missing momentum is now known as the gluon, the gauge boson of QCD. Thus, the new momentum formula for the quarks and gluons is written as

$$\int_0^1 dx x(u + \bar{u} + d + \bar{d} + s + \bar{s}) + \int_0^1 dx x g(x) = 1. \quad (1.23)$$

### 1.3.2 Polarized Deep Inelastic Scattering

Another method to study the structure of a nucleon is via the polarized deep inelastic scattering. A dimensionless physical quantity, called scaling, is introduced to understand this process. Scaling of a large class of dimensionless physical quantities in elementary particles strongly suggests that experimentally observed strongly interacting particles (hadrons)

behave as collections of point-like constituents when probed at high energies. A property of hadrons probed in high-energy scattering experiments is said to scale when it is determined not by the absolute energy of an experiment but by dimensionless kinematic quantities, such as a scattering angle or the ratio of the energy to a momentum transfer. Because increasing energy implies potentially improved spatial resolution, scaling implies independence of the absolute resolution scale, and hence effectively point-like substructure. In high  $Q^2$  deep inelastic scattering the structure functions exhibit approximate scaling as follows:

$$MW_1(v, Q^2) \rightarrow F_1(x, Q^2), \quad (1.24a)$$

$$vW_2(v, Q^2) \rightarrow F_2(x, Q^2), \quad (1.24b)$$

$$\frac{v}{M}G_1(v, Q^2) \rightarrow g_1(x, Q^2), \quad (1.24c)$$

$$\frac{v^2}{M^2}G_2(v, Q^2) \rightarrow g_2(x, Q^2). \quad (1.24d)$$

where  $W_1$  and  $W_2$  are the structure functions and  $G_1$  and  $G_2$  are the spin dependent structure functions. These variables are scaled to new variables like:  $F_1$ ,  $F_2$ ,  $g_1$  and  $g_2$ . For a longitudinally polarized proton target, the polarized differential cross-section is

$$\left( \frac{d^2\sigma \uparrow\uparrow}{d\Omega d\zeta} - \frac{d^2\sigma \uparrow\downarrow}{d\Omega d\zeta} \right) = \frac{4\alpha^2\zeta}{MvQ^2E} \left[ (E + \zeta \cos\theta)g_1(x, Q^2) - 2xMg_2(x, Q^2) \right]. \quad (1.25)$$

where  $E$  and  $\zeta$  are the energies of the source and the target. Applying the Equations 1.24 to the cross-section Equation 1.25 for the longitudinally polarized target, we can find the  $g_2$  contribution to the differential cross section and the longitudinal spin asymmetry is suppressed relative to the  $g_1$  contribution by the kinematic factor  $\frac{M}{E} \sim 0$  [20],

$$A_1 = \frac{\sigma_{\frac{1}{2}} - \sigma_{\frac{3}{2}}}{\sigma_{\frac{1}{2}} + \sigma_{\frac{3}{2}}} = \frac{MvG_1 - Q^2G_2}{M^3W_1} = \frac{g_1 - \gamma^2g_2}{F_1} \rightarrow \frac{g_1}{F_1} \quad (1.26)$$

where

$$\gamma = \frac{2Mx}{\sqrt{Q^2}} = \frac{\sqrt{Q^2}}{v} \quad (1.27)$$

The world data on the polarized structure function for the proton, deuteron and neutron

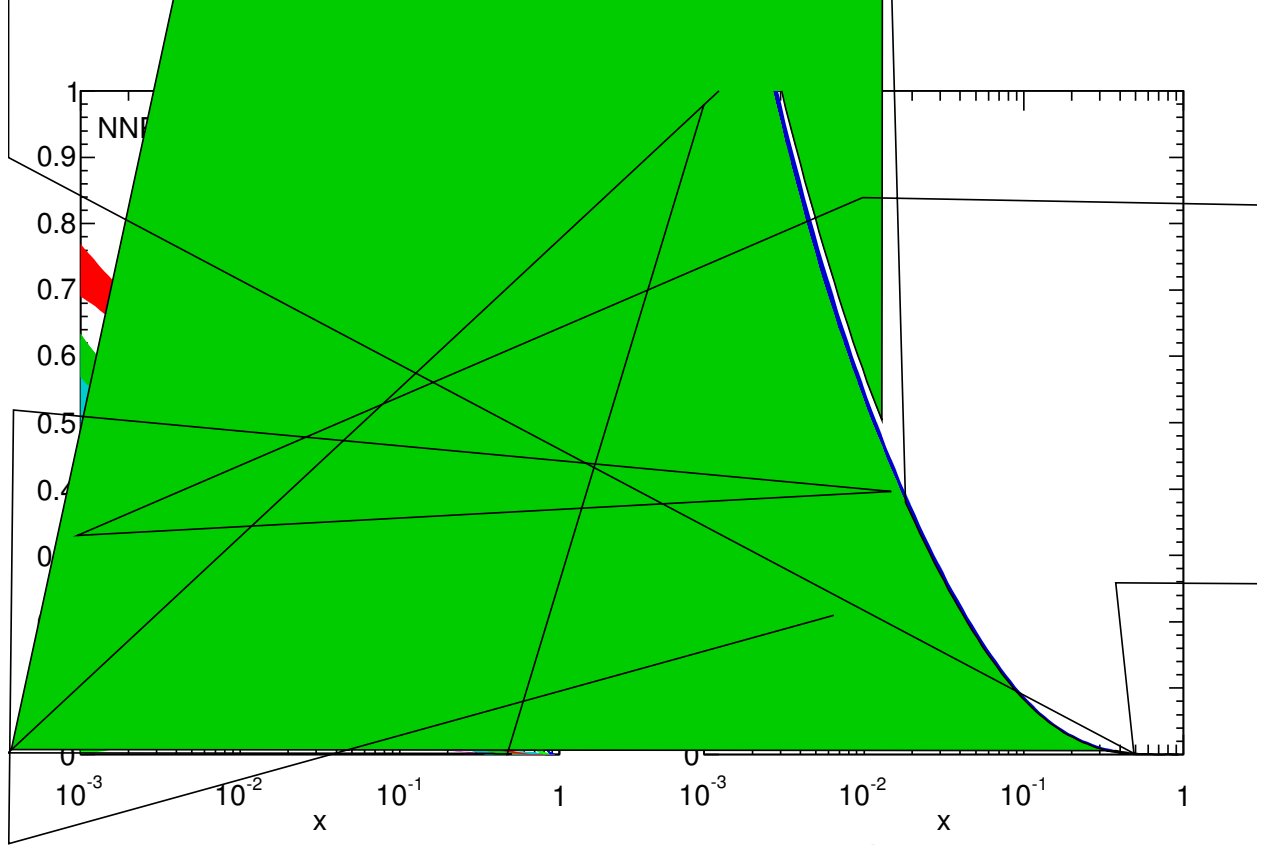


Figure (1.5) Unpolarized parton distribution function obtained in Next to Next to leading order global analysis at scales  $\mu^2 = 10 \text{ GeV}^2$  and  $\mu^2 = 10^4 \text{ GeV}^2$ . The data are compiled by particle data group (PDG) [36].

are shown in Figure 1.6.

### 1.3.3 Polarized Partons and high-energy proton-proton collisions

Before discussing polarized partons collisions, let us see the results for the unpolarized scattering. Figure 1.5 shows the unpolarized parton distribution function obtained in next to next to leading order (NNLO NNPDF2.3) global analysis. Now going back to polarized case, let us consider the case of  $pp \rightarrow \pi + X$ . The fragmentation function  $D_f^\pi(z, \mu^2)$  is defined as the probability density for a parton  $f$  to produce a pion in the final state with momentum fraction  $z$  of the parton  $f$  through hadronization. In the QCD parton model the cross section for this process is given by the Equation:

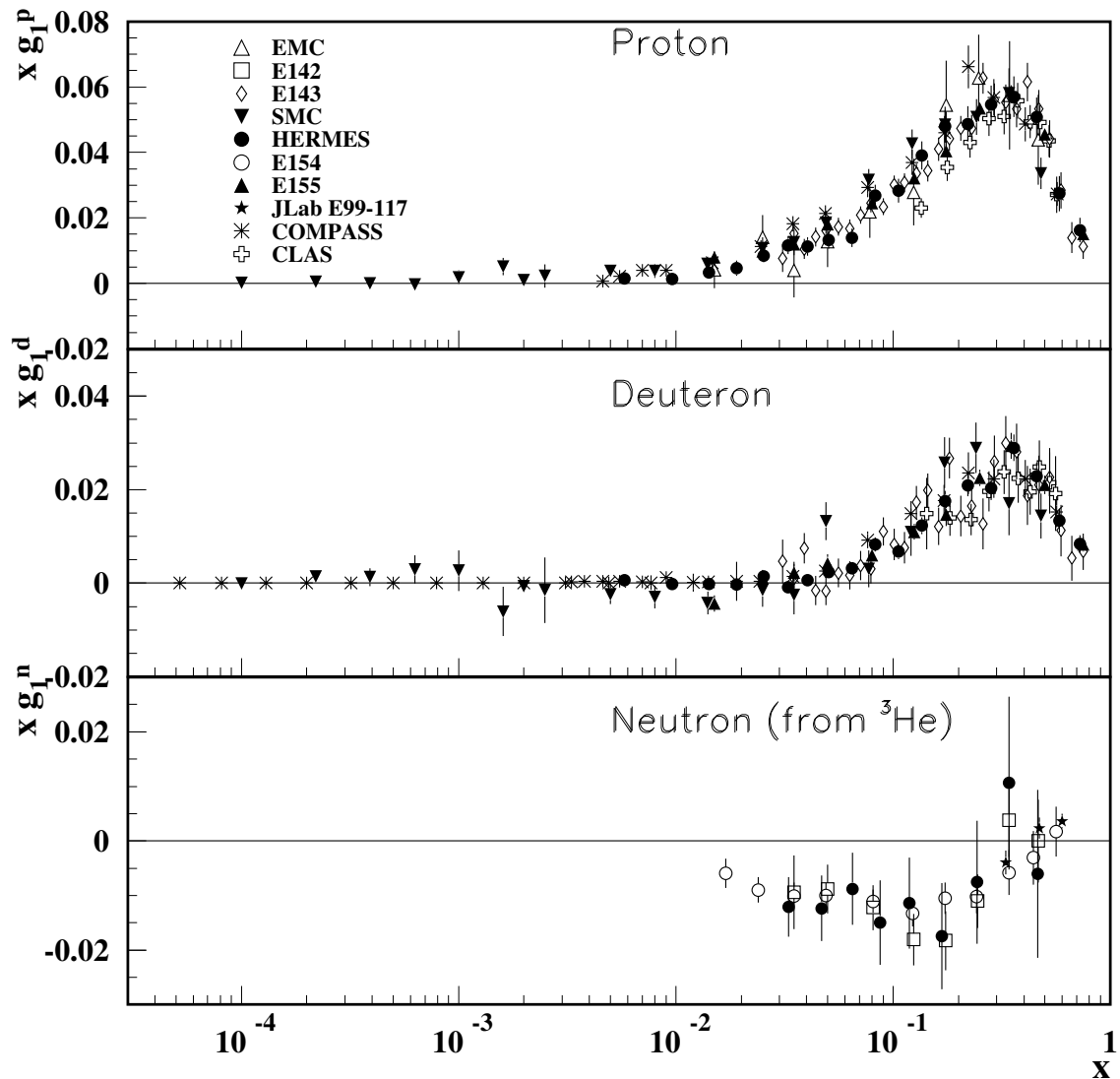


Figure (1.6) The world data on  $xg_1$  as a function of Bjorken  $x$ . The data are compiled by particle data group (PDG) [36]

$$\frac{d\sigma^{pp \rightarrow \pi X}}{d\beta} = \sum_{f_1, f_2, f} \int dx_1 dx_2 dz f_1^p(x_1, \mu^2) f_2^p(x_2, \mu^2) \frac{d\hat{\sigma}^{f_1 f_2 \rightarrow f X'}}{d\beta}(x_1 p_1, x_2 p_2, \beta_\pi/z, \mu) D_f^\pi(z, \mu^2) \quad (1.28)$$

Here  $p_1$  and  $p_2$  are the momenta of the incident protons and  $\beta$  is for the appropriate set of kinetic variables of the reaction. The  $f_i^p(x, \mu^2)$  terms are the quark and gluon parton distributions of the incident protons. The  $\hat{\sigma}^{f_1 f_2 \rightarrow f X'}$  are the underlying hard-scattering cross sections for initial partons  $f_1$  and  $f_2$  producing a final-state parton  $f$  plus unobserved  $X'$ . The parton model described above can be easily generalized to spin dependent processes. The fragmentation function for a parton to produce a pion should not depend on the spin of the parton because the pion has spin zero. Equation 1.28 can be generalized as

$$\frac{d\sigma^{pp \rightarrow \pi X}}{d\beta} \equiv \frac{1}{4} \left[ \frac{d\sigma_{++}^{pp \rightarrow \pi X}}{d\beta} + \frac{d\sigma_{--}^{pp \rightarrow \pi X}}{d\beta} - \frac{d\sigma_{+-}^{pp \rightarrow \pi X}}{d\beta} - \frac{d\sigma_{-+}^{pp \rightarrow \pi X}}{d\beta} \right] \quad (1.29a)$$

$$= \sum_{f_1, f_2, f} \int dx_1 dx_2 dz \Delta f_1^p(x_1, \mu^2) \Delta f_2^p(x_2, \mu^2) \times \frac{d\Delta\hat{\sigma}^{f_1 f_2 \rightarrow f X'}}{d\beta}(x_1 p_1, x_2 p_2, \beta_\pi/z, \mu) D_f^\pi(z, \mu^2) \quad (1.29b)$$

where

$$\frac{d\Delta\hat{\sigma}^{f_1 f_2 \rightarrow f X'}}{d\beta} \equiv \frac{1}{4} \left[ \frac{d\sigma_{++}^{pp \rightarrow \pi X}}{d\beta} + \frac{d\sigma_{--}^{pp \rightarrow \pi X}}{d\beta} - \frac{d\sigma_{+-}^{pp \rightarrow \pi X}}{d\beta} - \frac{d\sigma_{-+}^{pp \rightarrow \pi X}}{d\beta} \right] \quad (1.30)$$

### 1.3.4 Spin Structure of the Proton

Bjorken was the first to discuss spin structure in the context of deep inelastic scattering [24]. In 1966, he derived a fundamentally important sum rule

$$I_p - I_n = \int_0^1 (g_1^p - g_1^n) dx = \frac{1}{6} \left| \frac{g_A}{g_V} \right|, \quad (1.31)$$

where  $I_p$  and  $I_n$  are the structure function for proton and neutron and the factor  $\left| \frac{g_A}{g_V} \right|$  is the ratio of the nucleon axial vector and vector couplings, and measured to be  $1.2573 \pm 0.0028$  from beta decay of the neutron.  $g_1^p$  and  $g_1^n$  are the structure functions and are related to the asymmetries  $A_1^p$  and  $A_1^n$  for proton and neutron, respectively, and the unpolarized structure

functions  $F_1^p$  and  $F_1^n$  are given by  $g_1(x) \approx A_1(x) F_1(x)$ , and  $x$  is the Bjorken scaling variable. The Bjorken sum rule is valid assuming an infinite  $Q^2$ . Since experiments do not achieve  $Q^2 = \infty$ , there are QCD corrections to Equation 1.31. To incorporate the modification, Ellis-Jaffe sum rules were proposed in 1973 [22]. The Ellis-Jaffe sum rules are

$$I_p = \int_0^1 g_1^p(x) dx = \frac{1}{12} |g_A/g_V| \left[ 1 + \frac{5}{3}(3F - D)/(F + D) \right] \quad (1.32)$$

, and

$$I_n = \int_0^1 g_1^n(x) dx = \frac{1}{12} |g_A/g_V| \left[ -1 + \frac{5}{3}(3F - D)/(F + D) \right]. \quad (1.33)$$

where  $F$  and  $D$  are SU(3) parameters and are derived from experimental measurements of the beta decay of the neutron and hyperons in the baryon octet whose values are  $F = 0.459 \pm 0.008$  and  $D = 0.798 \pm 0.008$  [34]. Ellis-Jaffe sum rules assume that strange quarks in the nucleon are unpolarized.

The structure function  $g_1^p$  was determined by the EMC experiment [35] at a fixed  $Q^2 = 10.7 \text{ GeV}^2$ , as

$$\int_{0.01}^{0.7} g_1^p dx = 0.120 \pm 0.013 \pm 0.056. \quad (1.34)$$

Also the contributions outside the measured region were obtained from QCD evolution and are given by

$$\int_{0.7}^1 g_1^p dx = 0.001, \quad (1.35a)$$

$$\int_0^{0.01} g_1^p dx = 0.002. \quad (1.35b)$$

The systematic errors affect the values in all the bins in the same way. The contribution to the total uncertainty from each separate source is estimated by recalculating the integral after increasing or decreasing all the points simultaneously by the corresponding systematic

errors. Thus, from the asymmetry measurements the integral becomes

$$\int_0^1 g_1^p dx = 0.123 \pm 0.013 \pm 0.019, \quad (1.36)$$

where the  $\pm 0.013$  is the statistical error and  $\pm 0.019$  is the systematic error.

The combined values of the integral of structure function from SLAC and EMC is shown below. The SLAC data give

$$\int_{0.1}^{0.7} g_1^p dx = 0.094 \pm 0.008 \pm 0.014, \quad (1.37)$$

and in the same region, the EMC data give

$$\int_{0.1}^{0.7} g_1^p dx = 0.090 \pm 0.010 \pm 0.011. \quad (1.38)$$

Combining all the regions by extrapolating into the unmeasured regions gives

$$\int_0^1 g_1^p dx = 0.126 \pm 0.010 \pm 0.015. \quad (1.39)$$

The value expected for this integral from the Ellis-Jaffe sum rule is  $0.189 \pm 0.005$  using the current values of  $F/D = 0.631 \pm 0.018$ ,  $g_A = 1.254 \pm 0.006$  and  $\alpha_s = 0.27 \pm 0.02$  at  $Q^2 = 10.7 \text{ GeV}^2$ . The measured value is inconsistent with this prediction. The polarized parton distribution functions for different quarks are shown in Figure 1.7. Including the gluon distribution function, the polarized distribution function of quarks and gluons is shown in Figure 1.8. The naive quark model (NQM) predicts that due to relativistic effects the proton spin consists of only the total angular momentum of the quarks which can be expressed as:

$$\langle S_z^P \rangle = \frac{1}{2} = \frac{1}{2}\Delta\Sigma + L_q, \quad (1.40)$$

where  $\Delta\Sigma$  is the quark spin contribution and  $L_q$  the contribution from the quark orbital

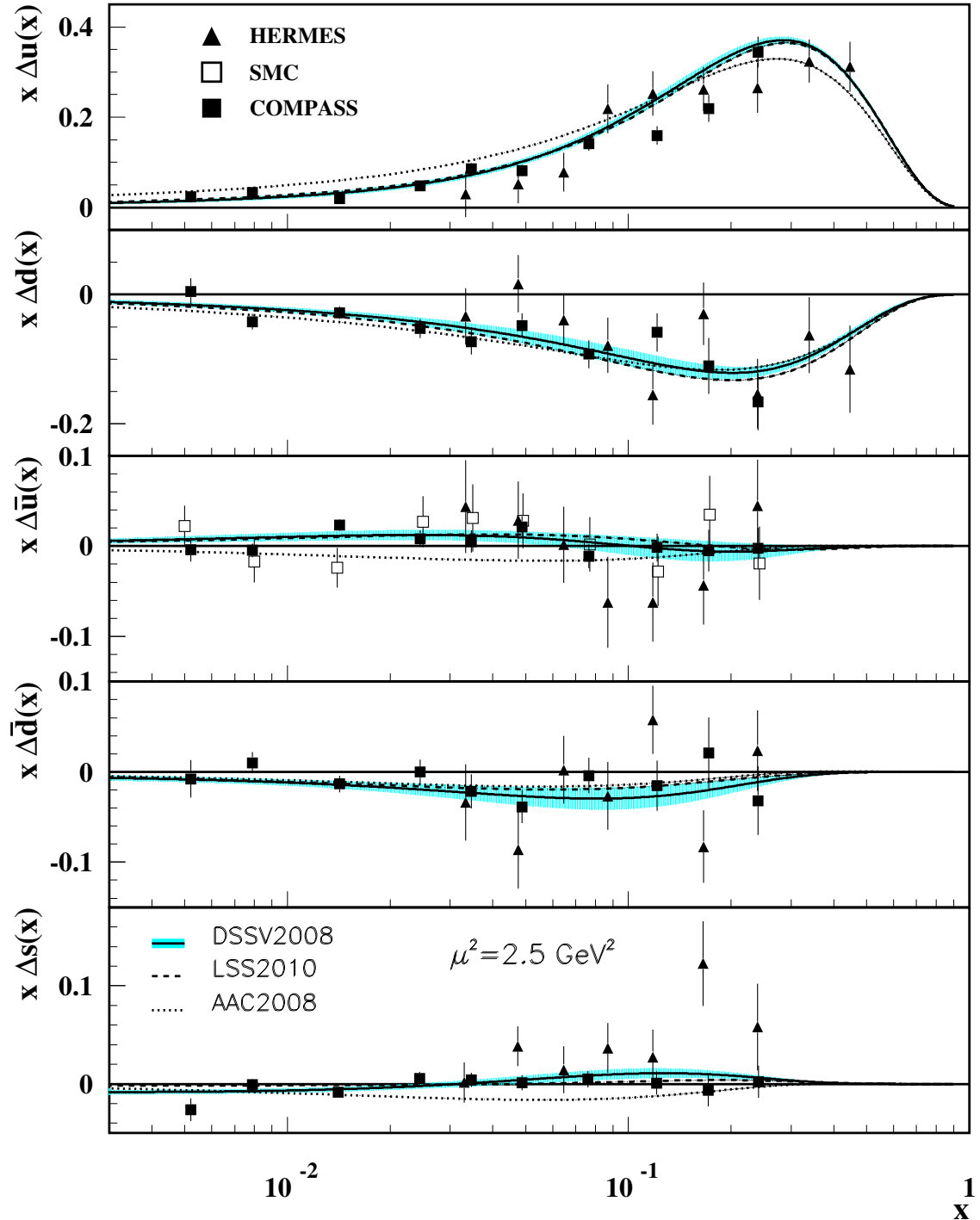


Figure (1.7) The parton distribution function for different quarks. The triangle data points are from HERMES experiment, the empty square box data points are from SMC experiment and the filled square box data points are from COMPASS experiment. Similarly, the solid lines are from DSSV2008 [63], the dash lines are from LSS2010 [64] and dot lines are from AAC2008 [65].

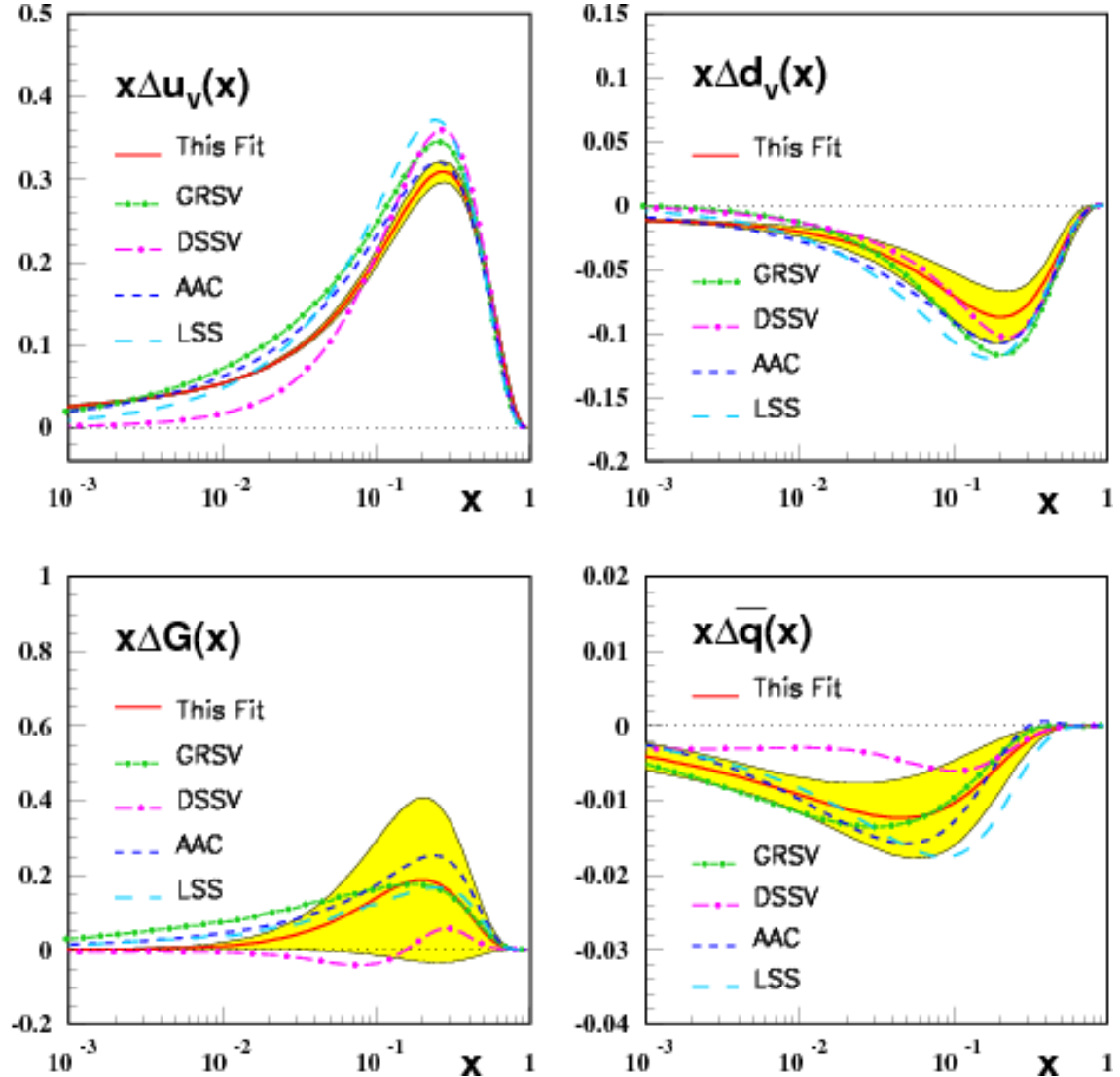


Figure (1.8) NLO polarized parton distributions at the input scale  $Q_0^2 = 4.0$  GeV $^2$  (solid line) compared to results obtained by GRSV (dashed-dotted line [47]), DSSV (long dashed-dotted line) [63], AAC (dashed line [49] , LSS (long dashed line) [71]. The shaded areas represent the  $1\sigma$  bands calculated by Gaussian error propagation. “This fit” represents the fit from [16].

angular momentum. The value of  $\Delta\Sigma$  was supposed to be 0.6. However, the experiments performed at EMC [20] showed that the quark spin fell short of 0.6 and opened a new chapter in this arena.

According to the modern concept, the total spin of the proton is the sum total of spin contribution from quarks ( $\Delta\Sigma$ ), gluons ( $\Delta G$ ) and angular momentum ( $L_q$  and  $L_g$  for quark and gluon) from Jaffe-Manohar spin sum rule [51] which is given by Equation 1.41.

$$\langle S_z^P \rangle = \frac{1}{2}\Delta\Sigma + \Delta G + L_q + L_g. \quad (1.41)$$

Recent results from DIS have confirmed that the quark spin contribution is about 25 - 30% which falls short of the original estimations.

### 1.3.5 Longitudinal Double Spin Asymmetry

In order to incorporate the polarization effects, the unpolarized cross-section Equation 1.15 is modified as

$$\Delta\sigma^{p+p \rightarrow h+X} = \sum_{f_a, b=q, \bar{q}, g} \Delta f_a(x_a, Q^2) \otimes \Delta f_b(x_b, Q^2) \otimes \Delta\hat{\sigma}^{a+b \rightarrow c+X}(x_a P_1, x_b P_2, q, z P_c) \otimes D_h^c(z, Q^2), \quad (1.42)$$

where  $\Delta f_a$  and  $\Delta f_b$  are the polarized parton distribution functions,  $\Delta\sigma$  is the difference between the same and opposite helicity particle

$$\Delta\sigma = \sigma_{++} + \sigma_{--} - (\sigma_{+-} + \sigma_{-+}) \quad (1.43)$$

Experimentally, however, there are often large systematic uncertainties due to detector acceptance and efficiencies, which make such a cross section measurement difficult. Instead the ratio of polarized and unpolarized cross sections are measured which largely reduces the systematic uncertainties. This ratio is called the longitudinal double spin asymmetry  $A_{LL}$ ,

which is given by:

$$A_{LL} = \frac{\Delta\sigma^{p+p \rightarrow \pi^0+X}}{\sigma^{p+p \rightarrow \pi^0+X}} \quad (1.44)$$

$$= \frac{\sum_{f_{a,b}=q,\bar{q},g} \Delta f_a \otimes \Delta f_b \otimes \Delta \hat{\sigma}^{a+b \rightarrow c+X} \otimes D_h^c}{\sum_{f_{a,b}=q,\bar{q},g} f_a \otimes f_b \otimes \hat{\sigma}^{a+b \rightarrow c+X} \otimes D_h^c} \quad (1.45)$$

$$= \frac{\sigma_{++} + \sigma_{--} - (\sigma_{+-} + \sigma_{-+})}{\sigma_{++} + \sigma_{--} + (\sigma_{+-} + \sigma_{-+})} \quad (1.46)$$

Experimentally,  $A_{LL}$  is calculated as:

$$A_{LL} = \frac{\sigma_{++} - \sigma_{+-}}{\sigma_{++} + \sigma_{+-}} \quad (1.47)$$

$$= \frac{\frac{N^{++}}{(\epsilon_{bias}^{++} \epsilon_{acc}^{++} \epsilon_{reco}^{++})}}{L^{++}} - \frac{\frac{N^{+-}}{(\epsilon_{bias}^{+-} \epsilon_{acc}^{+-} \epsilon_{reco}^{+-})}}{L^{+-}} \\ = \frac{\frac{N^{++}}{(\epsilon_{bias}^{++} \epsilon_{acc}^{++} \epsilon_{reco}^{++})}}{L^{++}} + \frac{\frac{N^{+-}}{(\epsilon_{bias}^{+-} \epsilon_{acc}^{+-} \epsilon_{reco}^{+-})}}{L^{+-}}, \quad (1.48)$$

where

$$\sigma = \frac{N_{Corrected}}{L}. \quad (1.49)$$

where  $L$  is the recorded luminosity.  $N_{Corrected}$  is the yield corrected with the efficiencies in reconstruction ( $\epsilon_{reco}$ ), trigger bias ( $\epsilon_{bias}$ ) and detector acceptance ( $\epsilon_{acc}$ ). A polarized proton accelerator offers a unique environment where  $\epsilon^{++} = \epsilon^{+-}$  so we use a simpler formula to get  $A_{LL}$

$$A_{LL} = \frac{1}{P_Y P_B} \frac{\frac{N^{++}}{L^{++}} - \frac{N^{+-}}{L^{+-}}}{\frac{N^{++}}{L^{++}} + \frac{N^{+-}}{L^{+-}}}. \quad (1.50)$$

where  $P_B$  and  $P_Y$  are the polarization of the two beams at RHIC. Since the beams at RHIC are not completely polarized, these values are used to normalize the measured asymmetry to get the physics asymmetry. Also,  $L^{++}$  ( $L^{+-}$ ) are the relative luminosity for same (opposite) helicity.

## 1.4 Neutral Pion $A_{LL}$

In this thesis, we focus on measuring the  $A_{LL}$  of  $\pi^0$ 's, as given in Equation 1.50. The  $\pi^0$  is dominantly produced in  $p + p$  collisions and the PHENIX central arms are designed to detect its decay photons. The fractions of  $\pi^0$  produced from the three possible partonic interactions in  $p + p$  collisions: gluon-gluon (gg), quark-gluon (qg) and quark-quark (qq) are shown in Figure 1.9. From this Figure, it is seen that the scattering processes that include gluons (qg) are dominated in the accessed kinematic region.

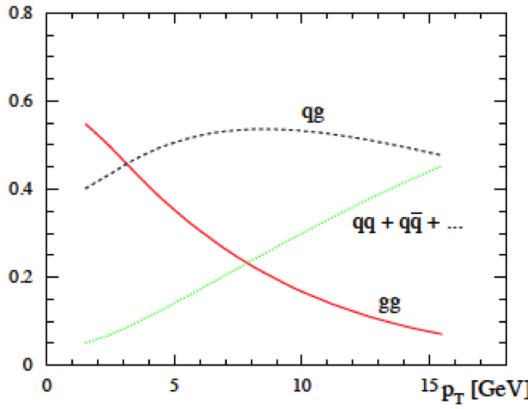


Figure (1.9) Relative fraction of  $\pi^0$  production as a function of  $p_T$  in  $p + p$  collisions at mid-rapidity. The solid red (online) represents the contribution from the gluon-gluon scattering, dashed black represents the contribution from the gluon-quark scattering and dotted green (online) represents the contribution from the quark-quark scattering. The figure is from [52].

## CHAPTER 2

### EXPERIMENT

The double helicity asymmetry,  $A_{LL}$ , measurement is performed at the Relativistic Heavy Ion Collider, RHIC, using the PHENIX detector. In this chapter, the RHIC compound and the PHENIX detectors used to measure  $A_{LL}$  will be presented. RHIC provides collisions of polarized protons at six interaction points among which only PHENIX and STAR are currently operational. BRAHMS and PHOBOS are two smaller special-purpose detectors which have completed their physics goals and are now dismantled.

#### 2.1 Relativistic Heavy Ion Collider (RHIC) Complex

The RHIC facility at Brookhaven National Laboratory (BNL) enables studies of nuclear phenomena and the proton spin structure. This is accomplished via collisions of light and heavy ions, and polarized protons. The main goal of the polarized proton collisions at RHIC is to understand the source of the spin of the proton.

RHIC is the first and only polarized proton-proton collider to study the polarized proton structure. RHIC consists of two intersecting storage ring synchrotrons called Blue and Yellow. There are as many as 120 polarized proton bunches which can be accelerated to an energy of 255 GeV per proton. The rings intersect in 6 locations among which PHENIX is located at the 8 o'clock position of the RHIC ring. In the 2013 run, RHIC was typically operated with 109 out of 120 bunches filled in each ring. RHIC collides specimens like Au - Au, Cu -Cu, Cu - Au, d - Au and U - U to create high density and temperature, and explore a regime of the possible deconfinement of quarks and gluons in the colliding nuclei [25]. The protons scatter as beams of polarized quarks and gluons after the intense beams of polarized protons

collide. The outline of RHIC is shown in the Figure 2.1. RHIC complex also consists of a Linear Accelerator (LINAC), Booster, Alternating Gradient Synchrotron (AGS) and Siberian snakes, some of which are relevant to our analysis are discussed in coming section. More detail information about RHIC can be found in [25].

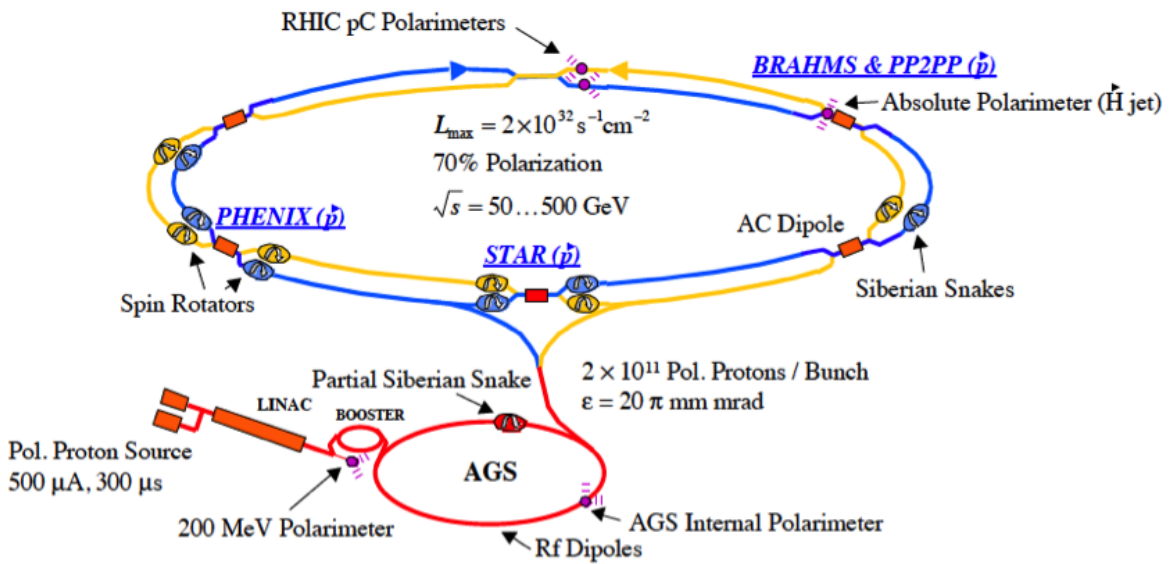


Figure (2.1) Sketch of the Relativistic Heavy Ion Collider complex including AGS Booster, the AGS, and the RHIC [25].

### 2.1.1 Polarized Proton Source and Booster

To study the spin structure of the proton, it is necessary to generate a beam of polarized protons. Polarized protons are generated by Optically Pumped Polarized  $H^{1-}$  Source (OPPIS). The OPPIS produces a 400  $\mu\text{s}$  pulse of  $10^{12}$  nuclearly polarized  $H^{1-}$  atoms with 35 KeV of kinetic energy. First, 3 KeV unpolarized protons ( $H^{1+}$ ) pass through an optically pumped rubidium gas in a 4T magnetic field producing a beam of electron-spin polarized  $H^0$  and un-reacted  $H^{1+}$  atoms. The  $H^{1+}$  ions are swept from the atomic beam by deflector plates and then the electron spin is transferred to the proton through a Sona transition [26]. The

Sona transition adiabatically brings the magnetic field from large positive to large negative values with a rapid jump between  $\pm 1$  gauss. Due to this rapid jump, the atoms also jump from electron-spin polarized atoms to nuclearly polarized atoms. After that, the beam is passed through a Na-jet vapor cell to facilitate acceleration of  $H^{1-}$  atoms. The atoms are then accelerated by a radio frequency quadrupole to 750 KeV. This polarized proton beam is now injected into LINAC and then to Booster.

### 2.1.2 LINAC

The LINAC includes ion sources, a radiofrequency quadropole, and nine accelerator radiofrequency cavities spanning the length of a 459 foot tunnel. The LINAC produce a  $H^{1-}$  beam of up to 200 MeV energy and 135  $\mu$ ampere current and injects the ions into the Booster.

### 2.1.3 From Polarized Proton Source to Accelerator

After the polarized protons beam is produced from an optically pumped polarized  $H$  source (OPPIS) with a polarization of  $\sim 80\%$  and accelerated via the LINAC, the beam is injected into a low energy booster. Proton bunches are injected into the Alternating Gradient Synchrotron (AGS) from the booster ring with proton energy of 2 GeV. The bunches are then accelerated to  $\sim 24.3$  GeV, and then injected into RHIC. There are many depolarizing resonances during the ramp in the AGS, and so controlling the polarization is very important for achieving high polarization in RHIC. In order to retain the polarization of the protons, sets of helical dipole magnets called Siberian snakes are used. The Siberian snakes are discussed in the next section. Due to the small size of the AGS, and the lack of straight sections in which a full Siberian snake can be inserted, there are no full Siberian snakes in the AGS. An 80% polarized proton source ( $H^-$ , to greatly improve the injection efficiency) feeds a series of accelerators. The AGS accelerates the protons to 24.3 GeV prior to injection into the two counter-rotating accelerator/storage rings of RHIC, indicated by blue and yellow rings.

## 2.2 Beam Instrumentation

### 2.2.1 Siberian Snakes and Spin Rotators

When the beam rotates through the storage ring, it loses the polarization. In order to preserve the polarization of the beam, Siberian snakes are used. There are two full snakes in each ring in RHIC, and their positions are shown in Figure 2.2. To understand this effect

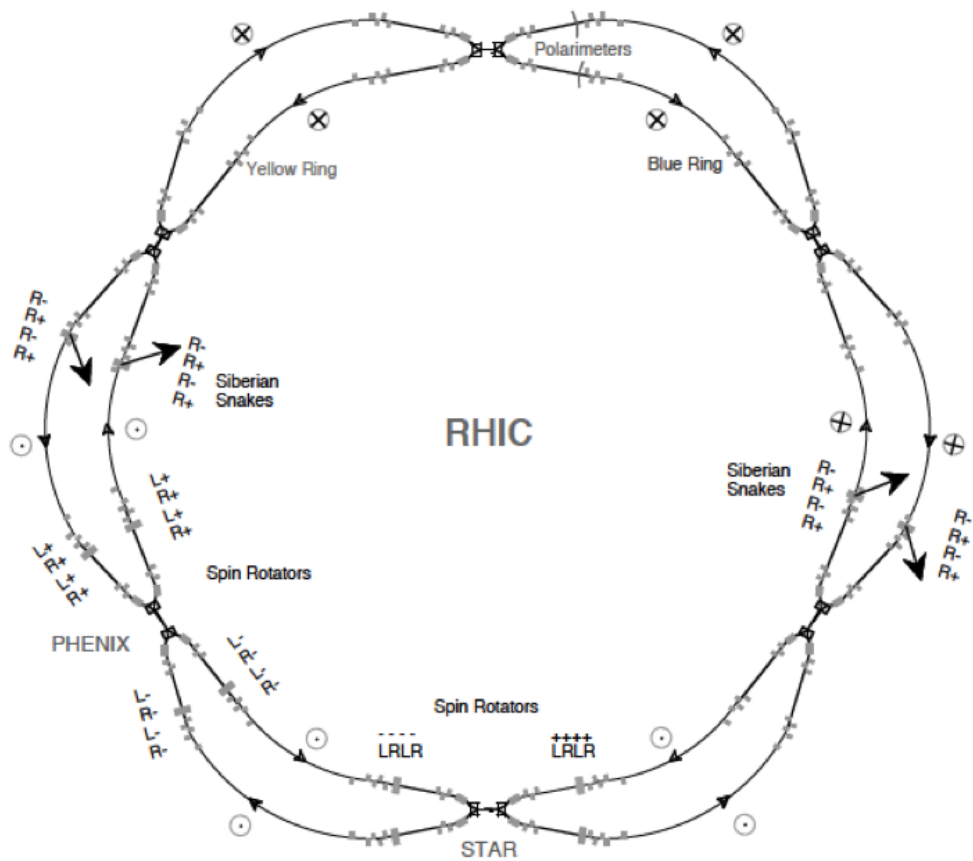


Figure (2.2) View of RHIC ring showing the location of the Siberian Snakes and the spin rotators placed around the collider experiments STAR and PHENIX. The polarization directions around the rings and around the detectors for collisions with longitudinal polarization are also shown [17].

the concept of the Lorentz force equation for the motion of particle in external magnetic

field is introduced which is given by:

$$\frac{d\vec{v}}{dt} = -\left(\frac{e}{\gamma m}\right) [\vec{B}_\perp] \times \vec{v}, \quad (2.1)$$

where  $e$  and  $m$  are the charge and mass of the particle respectively, and  $\gamma$  is the ratio of the electric field to the mass of the particle. If we consider the spin of the particle in an external magnetic field, the equation of motion is given by the Thomas-BMT equation [28]

$$\frac{d\vec{S}}{dt} = -\left(\frac{e}{\gamma m}\right) [G\gamma\vec{B}_\perp + (1+G)\vec{B}_\parallel] \times \vec{S}, \quad (2.2)$$

where  $G = 1.7928$  is the anomalous magnetic moment of the proton and  $B_{\parallel(\perp)}$  is the magnetic field parallel (perpendicular) to the particle's motion.  $G\gamma$  gives the number of full spin precessions for every revolution and is also called the spin tune,  $v_{sp}$ . At top RHIC energies,  $v_{sp}$  reaches about 400 [29]. The resonance effect from spin precession frequency and the frequency of the perturbation of the spin due to the magnetic field cause the depolarization of the protons. There are two main types of spin resonances corresponding to the possible sources of such fields: imperfection resonances, which are driven by magnet errors and misalignments, and intrinsic resonances, driven by the focusing fields. The strengths of both types of resonances increases with beam energy.

If there is some imperfection in the magnetic field at a given point in the ring it will perturb the precessions which eventually add constructively over multiple orbits and degrade the overall polarization of the beam. This is termed as "imperfection resonance". The imperfection depolarizing resonances arise when  $v_{sp} = G\gamma = n$ , where  $n$  is an integer.

During the circulation of the beam, it periodically deviates from its design orbit which is termed as betatron oscillations. Such deviations of the beam cause a depolarizing resonance when the spin tune matches the betatron oscillations or is an integer multiple of the magnetic lattice spacing (periodic placement of magnets around the ring, also called RHIC lattice).

This type of resonance is referred to as an "intrinsic resonance". The intrinsic resonances arise when  $v_{sp} = G\gamma = kP \pm v_y$ , where  $k$  is an integer,  $v_y$  is the vertical betatron tune and  $P$  is the superperiodicity.

**The use of Siberian Snakes:** To maintain polarization during the acceleration process, two full "Siberian snakes" are inserted on opposite sides of the RHIC lattice for each of the two counter-rotating rings. In addition, other magnetic components - spin rotators - are also located on each side of the two major interaction points which allow the spin orientation to be altered from the vertical direction to the horizontal direction. Superconducting magnets are used in order to contain the magnetic elements for a snake within a 10 m longitudinal space so as to fit within the available room in the RHIC lattice. Four right-handed helical dipole magnets, each 2.4 m long and operating near 4T or less can produce a Siberian snake. These dipoles create a field perpendicular to the spin vector, rotating the direction of the spin vector. If the vector is flipped 180°, then it is called the full snake. In the ideal case, a set of Siberian snakes precess the polarization vector by 180° per revolution as shown in Figure 2.3. The effect of this is to ensure that in any two revolutions, precessions of the spin

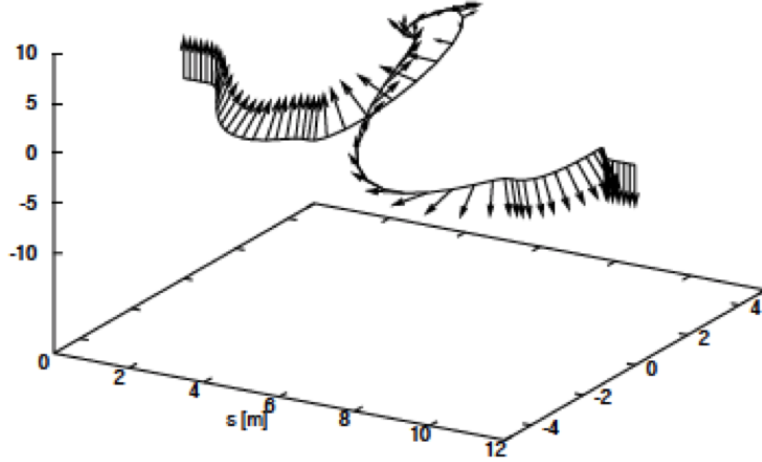


Figure (2.3) The polarization direction and path of a polarized proton bunch passing through a full Siberian snake [17].

vector due to resonances cancel. If the spin vector precession is not 180°, multiple orbits are needed to cancel out depolarization effects. These depolarization effects may not fully

cancel if the beam is accelerating during these multiple orbits. Detail of the Siberian snakes and their uses are explained in [27].

### 2.2.2 RHIC Polarimeters

In order to measure the polarization of the proton beams at RHIC an atomic beam source hydrogen gas jet (H-Jet) and proton-Carbon ( $pC$ ) polarimeters are used which are located at 12 o'clock area in the RHIC ring.

**$pC$ -Polarimeter:** Among the two polarimeters used in polarization measurements at RHIC, one is the  $pC$ -polarimeter which relies on proton-Carbon ( $pC$ ) elastic scattering. Two sets of identical  $pC$ -polarimeters are placed in the yellow and blue rings where the rings are separated. Figure 2.4 shows the schematic diagram of the  $pC$  polarimeter. Six silicon sensors are mounted in a vacuum chamber at  $45^\circ$ ,  $90^\circ$ ,  $135^\circ$  azimuthally in both left and right sides with respect to the beam as shown in Figure 2.4. Due to its high rates (2 million events in 1 s), it is used at RHIC for multiple measurements over the course of every fill to measure fill by fill polarization. However, the analyzing power is not directly measured, this measurement is only relative, and carries a large uncertainty (31% relative error per beam). In order to reduce this uncertainty another polarimeter called H-Jet is used to measure the absolute polarization.

**H-Jet Polarimeter:** The H-Jet polarimeter is used to measure the polarization of both beams and is located at the collision point. At first, hydrogen gas is polarized and ionized, and passed through the beam pipe, where it scatters from the beam. A polarimeter called a Breit-Rabi polarimeter (lower part in Figure 2.5) is used to measure the polarization after the beam exits the beam pipe. Molecular hydrogen can form after the H-Jet passes through the apparatus causing the dilution of the polarization. The outline of the H-Jet polarimeter used in RHIC is shown in Figure 2.5. Details of the H-Jet polarimeter are explained elsewhere [74].

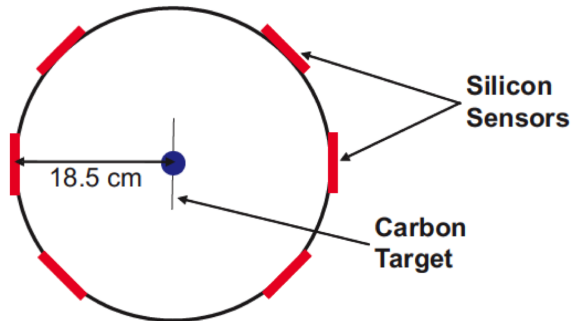


Figure (2.4) Beam view of  $pC$  polarimeter. The center is the carbon target and the beam is incident into it. Recoil Carbon atoms are measured with 6 silicon strip detectors (red) online [74].

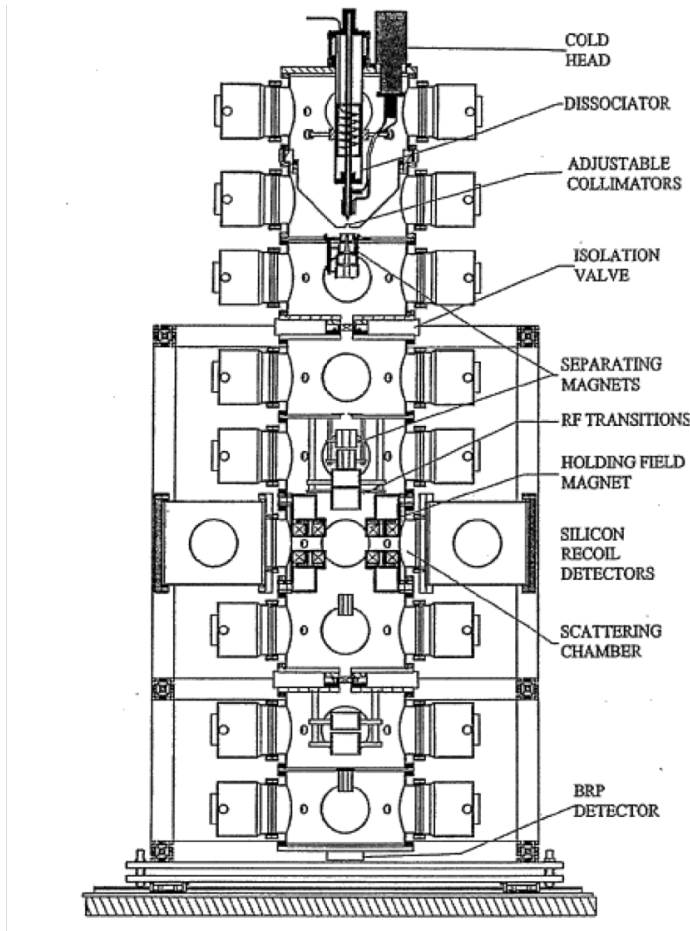


Figure (2.5) General layout of H-Jet polarimeter. This figure is taken from [74].

From the H-Jet, the polarized protons are scattered at nearly perpendicular angles to the beam direction. To measure the left right asymmetry of the beam, a set of three silicon detectors sit on each side of the beam perpendicular to both the beam and H-Jet axis. Since H-Jet is polarized, both target and beam asymmetries are measurable. This allows to measure the polarization absolutely. However, due to the low rate of this detector, many fills are required to achieve the lower uncertainties in the measurements. Both H-jet and  $pC$  are used for polarization measurements but H-jet target gives polarization information once per fill while  $pC$  gives several values, hence, H-jet is used to normalize the  $pC$  polarimeter.

### 2.2.3 Spin Rotators

In order to measure  $A_{LL}$ , longitudinal polarization of the proton beams is required. However, the stable direction for polarization at RHIC is vertical. Therefore, a set of four helical dipole magnets are used to rotate the polarization vector from the vertical axis to the horizontal axis. These dipole magnets are placed on each side of the PHENIX interaction point. The spin rotators have the same design as that of the Siberian snakes but the magnetic field strength of each component of helical dipole as well as degree of rotation of the polarization is different. Instead of causing a  $180^\circ$  rotation about the polarization axis, the spin rotators change the polarization direction from vertical to horizontal before collision. After collision, the beam polarization is reverted back to its original direction of polarization.

### 2.2.4 Different Spin Patterns used in Run 13

The polarization pattern for the beam bunches in RHIC is controlled and formed of different possible combinations ( $++$ ,  $+ -$ ,  $- +$  and  $--$ ). These patterns can collide at PHENIX within four filled crossings. During run 13, initially there were 8 different spin patterns P1, P2, P3, P4, P5, P6, P7 and P8, but at the later part of the run they are recombine to get different spin patterns. In order to distinguish them from the original patterns, they were named as P21, P22, P23, P24, P25, P26, P27 and P28. The list of patterns with the associated helicity is given in the Table 2.1.

Table (2.1) The different spin patterns used in run 13.

Spin Pattern	Beam	Patterns Helicity
P21	BLUE	+ + - - + + - - + +
	YELLOW	- - + + + + - - - -
P22	BLUE	+ + - - + + - - + +
	YELLOW	+ + - - - + + + +
P23	BLUE	- - + + - - + + - -
	YELLOW	- - + + + + - - - -
P24	BLUE	- - + + - - + + - -
	YELLOW	+ + - - - + + + +
P25	BLUE	- - + + + + - - - -
	YELLOW	+ + - - + + - - + +
P26	BLUE	- - + + + + - - - -
	YELLOW	- - + + - - + + - -
P27	BLUE	+ + - - - + + + +
	YELLOW	+ + - - + + - - + +
P28	BLUE	+ + - - - + + + +
	YELLOW	- - + + - - + + - -

### 2.3 PHENIX Detector

The PHENIX detector is a large general purpose detector which is located at the 8 o'clock position of the RHIC ring. It consists of two central arms at midrapidity, shown in the upper frame of Figure 2.6, and two muon spectrometers at forward rapidity, shown in the lower frame of Figure 2.6. The PHENIX detector also includes the beam beam counters (BBC) and zero degree calorimeters (ZDC) which can be seen in the lower frame of Figure 2.6.

For this analysis, the two central arms, the beam-beam counters, and the zero degree calorimeters are used and are discussed in the subsequent sections.

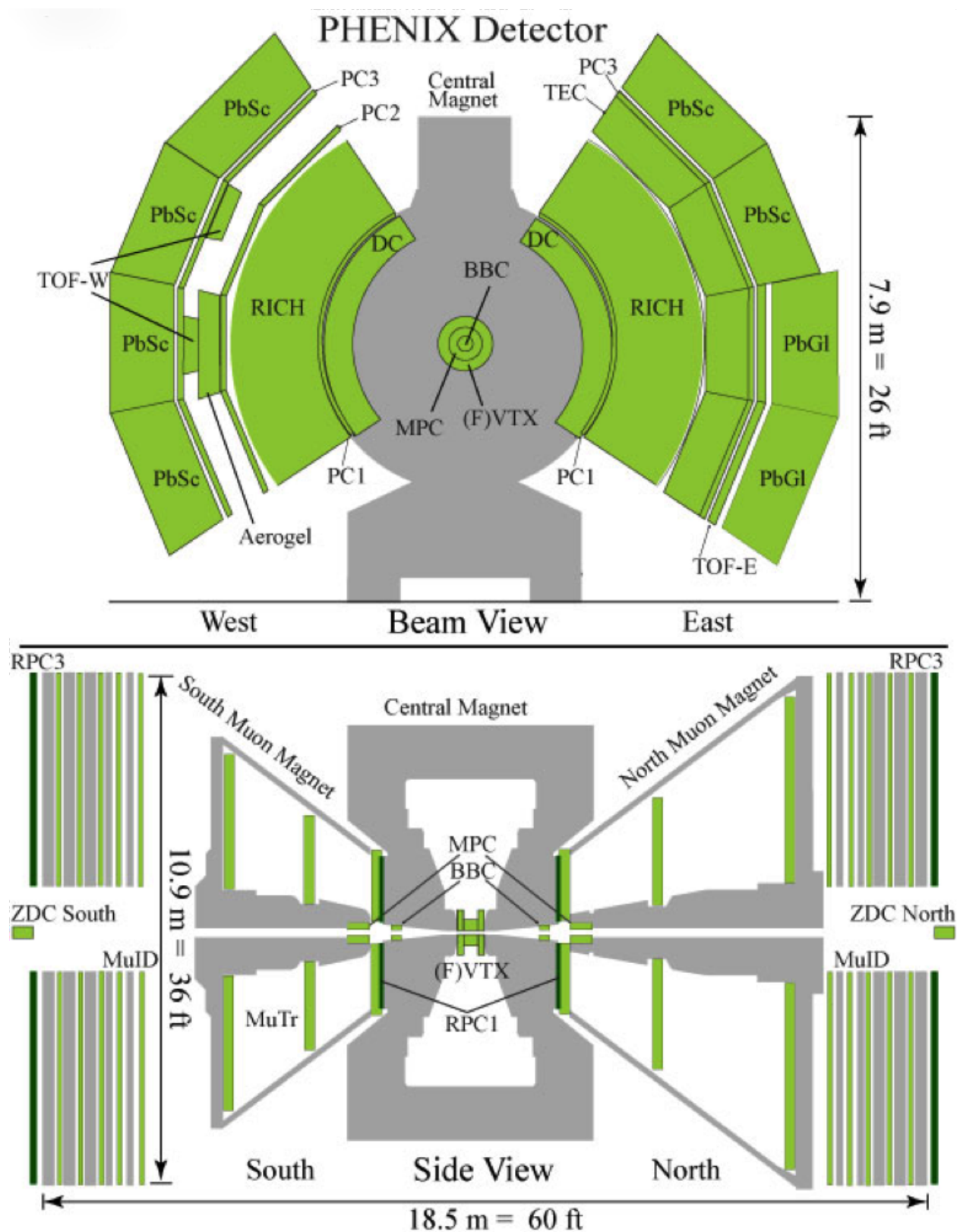


Figure (2.6) Layout of Phenix Detector. Top is the central arm and the bottom is the muon arm.

### 2.3.1 Central Arm Detectors

The central (east and west) arms consist of several subsystems for tracking, particle identification, and energy measurements. Each cover a pseudorapidity<sup>1</sup> range of  $|\eta| < 0.35$  and have azimuthal coverage of  $\Delta\phi = \frac{\pi}{2}$ . From a radius between 2 and 5 m outside the magnetic field region, there are several tracking and PID detectors that are not used in this work and will not be described here. There is a thin multiwire proportional chamber called the pad chamber (PC3) which is approximately at 5 m from center. PC3 is immediately followed by an electromagnetic calorimeter (EMCal). EMCal are used for energy reconstruction and event triggering.

**Electromagnetic Calorimeter (EMCal)** The PHENIX Electromagnetic Calorimeter (EMCal) is used to measure the spatial position and energy of electrons and photons produced in heavy ion and  $p + p$  collisions. It covers the full central arm acceptance of  $|\eta| < 0.35$  [31]. It is also used in triggering. The EMCal system can trigger on rare events with high transverse momentum photons and electrons [31].

The EMCal consists of 6 sectors among which four are in the west arm and two in the east arm. The EMCal is comprised of two types of calorimeters: Lead Scintillator (PbSc) and Lead Glass (PbGl) calorimeters as shown in Figure 2.6.

**PbSc Calorimeter** All the west arm sectors and two of the east arm are made of PbSc calorimeters. The PbSc electromagnetic calorimeter is a shashlik type sampling calorimeter made of alternating tiles of Pb and scintillator called cells which consists of 15552 individual towers and covering an area of approximately  $48 \text{ m}^2$ . These cells are optically connected by 36 longitudinally penetrating wavelength shifting fibres for light collection. Light is read out by 30 mm FEU115M phototubes at the back of the towers. Four towers are mechanically

---

<sup>1</sup>A commonly used spatial coordinate describing the angle of a particle relative to the beam axis. Its value will be maximum along beam direction and minimum perpendicular to beam direction

grouped together into a single structural entity called a module. 36 modules are attached together by welded stainless steel skins on the outside to form a rigid structure called a supermodule. Eighteen supermodules make a sector with a dimension of  $2 \times 4 \text{ m}^2$  plane. Details of the design can be found in [31]. The energy resolution is given by

$$\frac{\sigma_E}{E} = 2.1\% \oplus \frac{8.1\%}{\sqrt{E}}. \quad (2.3)$$

**PbGl Calorimeter** The PbGl calorimeter modules in the east arm consist of 9216 individual towers as shown in Figure 2.6. The PHENIX Time-of-Flight (TOF) system is located on the PbGl sectors. Each PbGl module is  $40 \text{ mm} \times 40 \text{ mm} \times 400 \text{ mm}$  in size. Each sector comprises 192 supermodules (SM) in an array of 16 SM wide by 12 SM high. The PbGl modules within a SM are individually wrapped with aluminized mylar and shrink tube [31], and 24 modules are glued together with carbon fiber and epoxy resin to form a self-supporting SM with a shared calibration system. The energy resolution for the PbGl calorimeter is given by

$$\frac{\sigma_E}{E} = 0.8\% \oplus \frac{5.9\%}{\sqrt{E}}. \quad (2.4)$$

The use of two different technologies (detectors) within the same experiment by PHENIX was done deliberately as they increase the confidence level of the physics results because of different systematics of the two detectors. This also helps in producing independent cross checks of results within the same experiment.

### 2.3.2 Beam-Beam Counters

The Beam-Beam Counter (BBC) consists of two identical sets of counters installed on North and South sides of the interaction region along the beam direction and named as BBCN and BBCS, respectively [30]. The BBC's are at  $\pm 144 \text{ cm}$  from the center of the interaction region and surround the beam pipe covering a pseudorapidity coverage of  $3.0 < |\eta| < 3.9$  over the full azimuth. Each counter is composed of 64 one-inch diameter

mesh-dynode photomultiplier tubes (Hamamatsu R6178) equipped with 3 cm quartz on the head of the PMT as a Čerenkov radiator. The outer diameter of the BBC is 30 cm and the inner diameter is 10 cm. For this configuration the expected number of charged particles for a central Au - Au collision at 200 GeV is expected to be 15 particles per BBC element. In order to monitor and calibrate the drift of the timing for the ToF measurement, a laser signal which is used by the ToF and Electromagnetic Calorimeter (EMCal) calibration systems, is also delivered to individual BBC elements. The BBC system has 8 high voltage channels for each side. In order to maintain the system of low temperature, an air flow of  $200 \frac{l}{min}$  is used to cool the BBC. The BBC readout electronics chain consists of discriminators, shaping amplifiers, time-to-voltage converters (TVC) and flash ADC's (FADC). The BBC provides the Local Level 1 (LL1) trigger with an input signal thus the timing and pulse height of BBC elements are digitized during each beam crossing by the TVC and FADC and stored at the same time in the buffer memory. The timing achieved for a single element was  $52 \pm 4$  ps. During the first year of operation, a ToF resolution of 96 ps was obtained. Detail explanation of the BBCs is given in the Ref. [30]. The Beam-Beam counter is primarily used for the following purposes:

- Provides the time of beam-beam collisions for the ToF measurement.
- Provides a signal for the PHENIX LVL1 trigger.
- Measures the collision vertex point (ZVTX) along the beam axis.

### 2.3.3 Zero Degree Calorimeter and Shower Max Detectors

The RHIC Zero Degree Calorimeters (ZDC) [32] are hadron calorimeters used to detect neutrons emitted within a cone of 2 milliradians from the beam axis along both beam directions and measure their total energy. These evaporated neutrons are usually produced from both beam and target nuclei during high energy collisions of nuclei. The ZDC's are used for luminosity determination at all four interaction points around RHIC. The ZDC's are also used for event triggering and to calculate multiplicity. The neutron multiplicity is correlated

with the event geometry and thus the ZDC's are used to measure collision centrality in beam interactions. The mechanical design of the tungsten modules of ZDC's is shown in Figure 2.7. The PHENIX Shower Max Detectors (SMD) are layers of position sensitive hodoscopes

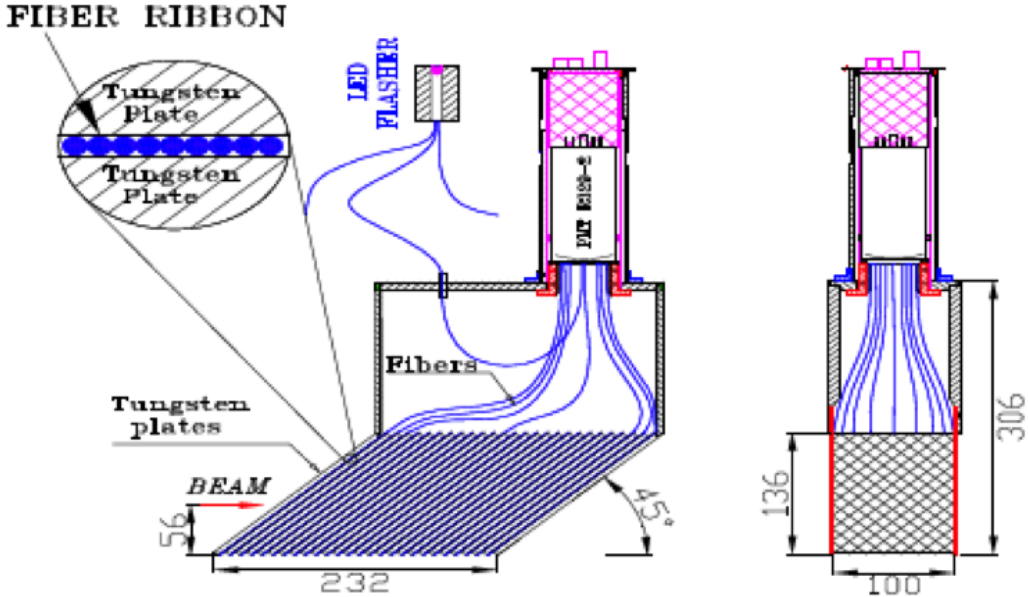


Figure (2.7) Mechanical design of the Tungsten Modules of Zero Degree Calorimeter [32].

sandwiched between the first and second module of the ZDC's. Since photon showers are concentrated in the first module of ZDC, the showers shown in the SMD's are primarily due to neutrons. The purpose of the SMD is to measure the centroid of showers in the ZDC in 2 coordinates-x and y. The first SMD layer has 21 strips of  $0.5 \text{ cm} \times 0.5 \text{ cm}$  scintillators each with wavelength shifting fiber readout. Groups of 3 fibers are read out by a single channel of a multi-anode PMT. The total width of the SMD, 10.5 cm, is subdivided into 7 samples. Similarly, the vertical coordinate has 8 elements of 4 scintillator strips. The ZDC as well as SMD are used in systematic error studies in the calculation of relative luminosity along with the measurement of polarization direction on a fill by fill basis which will be discussed in next chapter.

### 2.3.4 EMCAL RICH Trigger

To record events containing a  $\pi^0$  with high transverse momentum ( $p_T$ ), a photon trigger with high energy threshold is used. A basic trigger tile is a group of  $2 \times 2$  EMCAL towers and if some energy deposited is above a threshold in one tile, then the event will be triggered. If a high energy particle lies at the edge of a tile, the threshold will not be met for any one individual tile. Thus to reduce loss at the edge of a tile,  $2 \times 2$  tiles are overlapped to form a  $4 \times 4$  tower trigger. For Run 13  $\pi^0$  analysis at center of mass energy of 510 GeV, we used three triggers with three different thresholds. The three triggers:  $4 \times 4a$ ,  $4 \times 4b$  and  $4 \times 4c$  having the threshold energies of 4.7 GeV (3.7 GeV), 5.6 GeV (4.7 GeV) and 3.7 GeV (3.7 GeV), respectively, for PbSc (PbGl) were used. The different energy threshold values for PbSc and PbGl are due to difference in their energy resolutions.

## 2.4 Tracking

PHENIX has pad chambers (PC) detectors in each arm at varying radii for the tracking of charged particles. The construction and performance of the PHENIX PC are given in Ref. [73]. The PC, as shown in Figure 2.6, consists of three stations (PC1, PC2 and PC3) and covers a total area of  $88 \text{ m}^2$ . The PC have the following specifications:

- Provide reliable track information with an accurate coordinate in the  $z$  direction (parallel to the beams) and good position resolution in the  $\varphi$  direction.
- Define entry and exit coordinates of the particle identification subsystems, mainly the RICH and the EMCAL.
- Help separate neutral EMCAL showers from charged tracks.
- Help in vetoing the charged tracks that produce energy in the EMCAL.

PC2 and PC3 also play important roles in particle identification. In this analysis, PC3, which is located in front of the EMCAL, is used. It helps in identifying the charged particles

entering the EMCal. The cells in the PC3 are  $1.7 \times 1.7 \text{ cm}^2$ , which is significantly smaller than the position resolution of any EMCal tower. The two dimensional position resolution depends on whether a hit is contained within a single cell or split between two cells. If the hit is contained within a single cell, the resolution is simulated at 4.9 mm along the direction of the wires, and 6.1 mm across the wires. If the hit is split between two cells, the resolution improves and is 3.2 mm along the wires and 4.8 mm across [73].

## 2.5 Data Acquisition System

The PHENIX DAQ can write data at maximum rate of 700 MB/s. Data flows from each subsystem's front-end electronics in the interaction region over fiber optic cables to data collection modules (DCM) located outside the interaction region. After this, the data are passed to the Sub Event Buffers (SEB) and subsequently to the Assembly and Trigger Processor (ATP). The ATP's assemble the event's data from the individual subsystems and pass the data to one of a series of buffer boxes for archiving. The buffer boxes are composed of seven machines each with 15 terabytes of hard-drive space. All machines are written to in parallel, but each one's capacity is split into four filesystems: a, b, c and d. During normal operations data is written in sequence to a, b, c, d and then starts again at a. Swaps between filesystems are done once a filesystem reaches maximum capacity. After a swap, data are immediately copied to a tape robot with multi-petabyte storage capacity. The computing facility which houses this tape robot is called the RHIC Computing Facility (RCF). The RCF facility maintains a computing farm of several thousand machines used for reconstructing and analyzing data and a smaller set of machines for interactive use. Data are written to the buffer box in a binary format called Phenix Raw Data File (PRDF). The PRDF internal structure is based around a packet ID unique to each data collection module. After the data have been copied, it is safe to delete them from the buffer box but it is not done until the last possible moment. The data are kept locally on the buffer boxes for about twelve hours. This allows quick analysis of the data. Two types of analyses are done. The first is called online monitoring. It produces a simple but fast display of each detector's performance.

These plots are monitored by the shift crew all the time during RHIC run. The online monitoring of the detector performance plots are designed in such a way that any problems can automatically alert the shift crew. The second type of analysis is online calibration. Online calibration gives the subsystem experts a first iteration on calibrating their detector, and helps in speeding up their analysis. The performance of the particular subsystem can be easily tracked by the subsystem experts with the online calibration.

## CHAPTER 3

### DATA ANALYSIS

This chapter provides a detailed description of the data analysis. It includes the various analysis tools and techniques, the calibration procedures, the rates and the particle identification cuts. The last part of the chapter is dedicated to  $\pi^0$  reconstruction and asymmetry calculations.

#### 3.1 Quality Assurance (QA) of Data

In order to analyze qualitative data, any problem in the data sets should be identified and must be removed for further analysis. At first we checked the Data Acquisition (DAQ) time to see if there are any runs<sup>1</sup> which are terminated earlier than normal. After that we check the spin database to see if there are any problems with the polarization information.

##### 3.1.1 Data Acquisition (DAQ) Condition

Two DAQ tests are used to select good runs. First is the DAQ time. Runs that are shorter than 10 minutes are rejected because there might be some problem with the DAQ which caused early termination of the run. Second is the live-time of the BBCLL1, ERT\_4X4A, ERT\_4X4B and ERT\_4X4C triggers. The live-time of these triggers must be larger than 50%. There can be one or more problems in the run if the live-time of the triggers is below 50%.

##### 3.1.2 Spin Database

The spin database at PHENIX contains the runs that pass the spin-related QA tests. These tests include no clear crossing shift, strange spin patterns and problems with the

---

<sup>1</sup>Segment of data recorded within sixty to ninety minutes.

scaler<sup>2</sup> values like high scalers, empty scalers or noisy scalers. Runs with run numbers: 386825, 387557, 387558 and 390038 do not have clear crossing shift and also there is huge fluctuations. Runs 387247, 391170, 391818, 392096-392100, 392218-392223, 393798, 394525, 394528, 3945318 do not have the scaler values. Similarly, runs 395775, 396785, 391966-391970, 394389-394391, 391288-3912968 have either noise scalers or high values with large fluctuations. These runs are excluded from this analysis.

### 3.1.3 Polarization

A minimum of 10% polarization on both beams is required to pass run QA. Any run that has polarization value below 10% is an outlier since this value is much lower than the average value, which is  $\sim 55\%$  for each beam. Therefore, these runs are removed in this analysis.

## 3.2 EMCAL Calibration

After the basic QA is done, the next step is the energy calibration of EMCAL. The energy calibration is done using the  $\pi^0$  peak position in the di-photon invariant mass spectrum for each of the EMCAL towers. At lower transverse momentum ( $p_T$  below 5 GeV), the mass of each  $\pi^0$  candidate is below the mean mass of  $\pi^0$  which is  $\sim 135$  MeV [36]. Similarly, at higher transverse momentum ( $p_T$  above 8 GeV) the mass of each  $\pi^0$  candidate is above the mean mass. In order to correct this, the following procedure is followed: First, the cluster energy for a given tower is multiplied by 137 MeV<sup>3</sup> and then divided by the  $\pi^0$  peak position. This corrects the  $\pi^0$  peak position to around 137 MeV/ $c^2$ . Additionally, if the  $\pi^0$  invariant mass spectrum for any tower in any run is abnormal, the corresponding tower is marked as bad and removed for further analysis.

---

<sup>2</sup>RHIC has scaler board designed to record counts at a 10 MHz rate to correlate the fast detector data with the bunch number information to uncover the spin dependence of different signal combinations.

<sup>3</sup>Due to detector smearing effect, the mass of  $\pi^0$  is 137 MeV/ $c^2$  instead of 135 MeV/ $c^2$

### 3.3 Event Selection

The primary task of the data analysis is to identify the photon pairs that are coming from  $\pi^0$  decays. However, there are several other sources from which photon pairs can be produced. These photons contaminate the  $\pi^0$  signal. We estimate these sources of background by applying the following selection conditions and cuts on the event level.

- Trigger requirement: At least one of the triggers (ERT\\_4x4A, ERT\\_4X4B and ERT\\_4X4C) must be present in the event. Similarly, the cluster with higher energy should have the ERT\\_4X4C trigger. The leading photon of the di-photon pair is required to be in the triggered supermodule.
- BBC z-vertex requirement: The reconstructed vertex along the beam axis for the event should have values between  $\pm 30$  cm of the center of the interaction region.

### 3.4 Cluster Rejection Due to Electronic Noise

There are two methods used to reduce the effects due to electronic noise. One is the use of a minimum energy cut and the other is the warnmap. Both of them are discussed in following sub-sections.

#### 3.4.1 Minimum Energy Cut

The first method to reduce the effects caused by electronic noise is to exclude very low energy clusters by applying a higher threshold on the energy of the cluster. Since the center of mass energy for collision is high, we applied a minimum energy cut of 300 MeV for both PbSc and PbGl. This cut has a very small effect on the signal but have dramatically reduces the background under the  $\pi^0$  peak especially at low  $p_T$ . At high  $p_T$ , only decays with very asymmetric energies are cut. This energy asymmetry should be independent from the partonic distributions in the proton in the initial state. Thus, this cut will not bias the spin asymmetry measurement. Due to insignificant effect in the asymmetry measurement, the energy asymmetry cut is not applied.

### 3.4.2 Warn/Deadmap

Since hot or noisy towers can make the combinatorial background large, those towers are excluded in the analysis. To find such hot towers, hits per tower distribution is used such that if the number of hits per tower is greater than the average of all towers plus one standard deviation, the tower is masked and labeled as a hot tower. Similarly, if the tower doesn't have any hits, it is masked and labeled as dead tower. The uncalibrated and edge towers are also excluded. Towers which are neighboring a hot, dead or uncalibrated tower are also excluded. In addition, in order to prevent the analysis of a cluster centered on a good tower that extends into a bad tower, the adjacent towers to a masked tower are also excluded from the analysis because a typical photon shower is no more than three towers in diameter. Table 3.1 shows the number of hot, dead, and uncalibrated and edge towers that are masked.

Table (3.1) Number of non-edge (hot, dead and uncalibrated) and edge masked towers from “Or” triggered data. The number in the parenthesis is the percentage of the total. W0 to W3 are the sectors in west arm and E0 to E3 are the sectors in east arm.

sector	masked non-edge towers	masked edge towers	total towers
W0	2 (0%)	416 (16%)	2592
W1	39 (2%)	416 (16%)	2592
W2	46 (2%)	416 (16%)	2592
W3	60 (2%)	416 (16%)	2592
E0	88 (2%)	560 (12%)	4608
E1	74 (2%)	560 (12%)	4608
E2	65 (3%)	416 (16%)	2592
E3	60 (2%)	416 (16%)	2592
PbSc	272 (2%)	2496 (16%)	15552
PbGl	162 (2%)	1120 (12%)	9216
Total	434 (2%)	3616 (15%)	24768

### 3.5 $\pi^0$ Reconstruction

After the selection of events, the  $\pi^0$  invariant mass distribution is obtained by combining photon pairs according to the following equation,

$$m_{\gamma\gamma}^2 = E_1 \cdot E_2 - (p_1 \cdot p_2), \quad (3.1)$$

where  $p_1$  and  $p_2$  are the momenta of each photon and  $E_1$  and  $E_2$  are their energies. In terms of the angle between the decay photons, the invariant mass can also be written as:

$$m_{\gamma\gamma}^2 \equiv 2E_1E_2(1 - \cos\theta), \quad (3.2)$$

where  $E_1$  and  $E_2$  are the energies of the two clusters and  $\theta$  is the angle between the two vectors from the decay vertex to the EMCAL clusters.

### 3.6 Di-photon Cuts

After the spin related QA is done, several cuts are applied to reduce the combinatorial background under the  $\pi^0$  peak in the di-photon invariant mass spectrum. These cuts include:

**Global Energy Calibration:** The EMCAL reconstruction algorithm neglects contributions from towers with an energy below a set cutoff. Therefore, the reconstructed clusters will be missing small amounts of energy from those towers where the energy deposition was below this cutoff. The correction for these effects is parameterized as,

$$E_{final}^{PbSc} = \frac{E_{Calib}^{PbSc}}{0.003 + (1 - \frac{0.01}{E_{calib}^{PbSc}})}, \quad (3.3)$$

for PbSc and,

$$E_{final}^{PbGl} = \frac{E_{Calib}^{PbGl}}{0.021 + (1 - \frac{0.02}{E_{calib}^{PbGl}})}, \quad (3.4)$$

for PbGl.

**Minimum  $p_T$ :** Only  $\pi^0$  candidates which have  $p_T > 2$  GeV/c are considered for this analysis because there is large background which dilutes the  $\pi^0$  signal below 2 GeV/c.

**Shower Shape Cut:** In the EMCAL photons, electrons as well as hadrons produce a shower. Photons and electrons interact with material electromagnetically while hadrons interact with material via strong interaction. Hence, the two interactions produce different shower shapes which allows isolating photons and electrons from hadrons. The shower shape of the cluster is determined in terms of photon probability which is characterized by the variable “prob\_photon”. In this analysis, all clusters that have probability of being electromagnetic greater than 2% are included. i.e.,

$$\text{prob\_photon} > 0.02. \quad (3.5)$$

**Time of Flight Cut:** The time of flight (ToF) of a particle associated with an energy cluster in the EMCAL is defined as

$$\text{ToF} = \text{time}_{\text{EMCAl}} - \text{time}_{\text{BBC}} \quad (3.6)$$

where  $\text{time}_{\text{EMCAl}}$  is the time difference between RHIC clock and the time the particle hits the EMCAL, and  $\text{time}_{\text{BBC}}$  is the time difference between RHIC clock and the time the collision occurs, as determined by the BBCs. The ToF of an EMCAL tower is calibrated in such a way that the ToF peak of photons is centered at zero. We choose the time of flight range between -15 to +15 nano seconds for PbSc and -10 to +10 nano seconds for PbGl. Figure 3.1 shows the average time of flight (TOF) distributions from which it is seen that the average TOF is below 15 nano seconds for all runs. ToF cut is applied to all cluster to reject “ghost” cluster which is cluster of photons from previous events. Because clusters from previous events will be unassociated with the current event thus they will have a wide ToF distribution centered at different values of ToF as shown in left panel of Figure 3.1. The small bump at the right side of the left panel in Figure 3.1 is due to this “ghost” clusters. After the ToF cut is

applied, the corrected distribution is shown in the right panel of Figure 3.1.

**Charge Veto Cut:** Another method of reducing charged hadron contamination is to apply

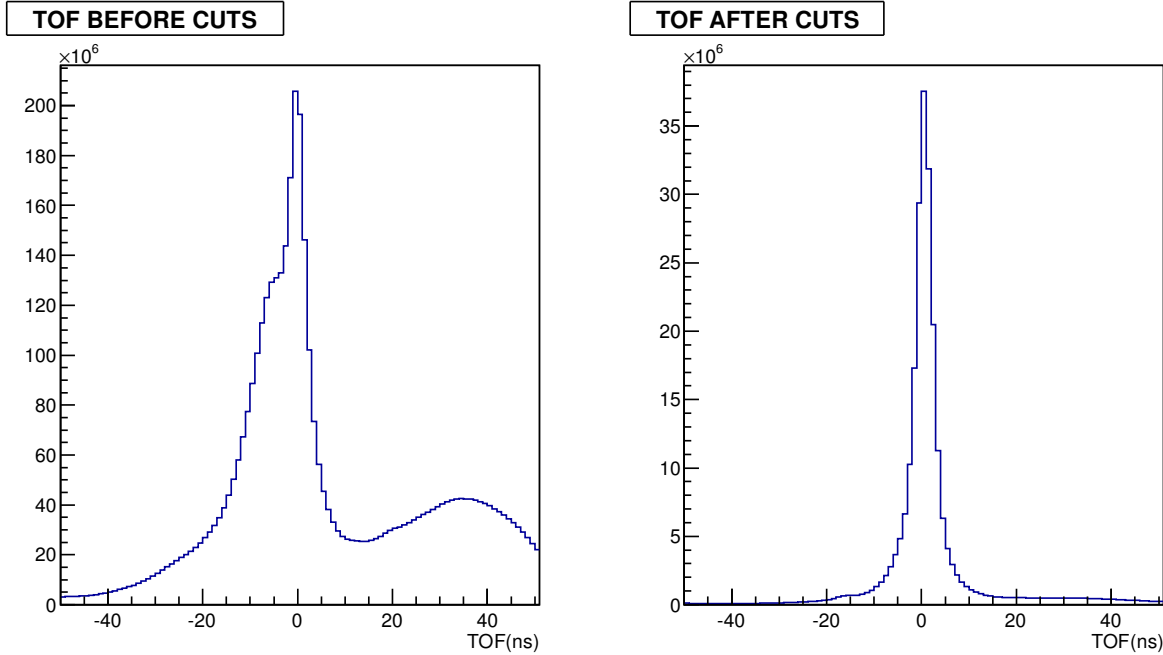


Figure (3.1) Time of flight distribution before and after applying the cuts.

a veto on clusters associated with charged tracks. For this, we look for hits in the PC3, which is about 20 cm closer radially to the z-axis than the EMCAL. We define two vectors: the first from the vertex  $(0, 0, z_{BBC})$  to the cluster position in the EMCAL, and the second from the vertex to the nearest hit in the PC3. The angle between these two vectors is defined as  $\theta_{cv}$ . The values of charge veto angle  $\theta_{cv}$  are divided into three regions (“small”, “medium”, and “large”), which can be identified in following manner:

1. Small  $\theta_{cv}$ : Electron positron pairs from photon conversions outside of the magnetic field region can still form a single cluster if their opening angle is small relative to the conversion’s distance from the EMCAL. In this case we may find an associated PC3 hit directly in front of the cluster, but we can still accurately reconstruct the original photon from the energy deposited. Thus we would like to retain these events.

2. Medium  $\theta_{cv}$ : For hadrons that travel through the inner magnetic field region, it is not possible to draw a straight line connecting the EMCal cluster, PC3 hit and collision vertex. Thus there will be some finite  $\theta_{cv}$  associated with these particles. We would like to exclude any such hadrons that are not already excluded by the shower shape and ToF cuts.
3. Large  $\theta_{cv}$ : The phase space for combinatorial association of an EMCal cluster with an unrelated PC3 hit increases linearly with  $\tan(\theta_{cv})$ . Thus random association dominates this region and we should not throw out these events.

The following formula is used for PbSc:

$$4.22 \times 10^{-5} + 1.16 \times 10^{-2} E_\gamma - 4.53 \times 10^{-3} E_\gamma^2 < \theta_{cv} < 1.01 \times 10^{-1} - 2.02 \times 10^{-1} E_\gamma + 1.50 \times 10^{-1} E_\gamma^2 - 3.66 \times 10^{-1} E_\gamma^3 \quad (3.7)$$

Similarly, the following formula is used for PbGl:

$$1.27 \times 10^{-2} - 2.14 \times 10^{-3} E_\gamma + 2.26 \times 10^{-3} E_\gamma^2 < \theta_{cv} < 1.64 \times 10^{-2} - 7.38 \times 10^{-3} E_\gamma + 1.27 \times 10^2 e^{-4.00 E_\gamma} \quad (3.8)$$

Figure 3.2 shows the  $\theta_{cv}$  as a function of energy of the cluster. In the Figure 3.2 the clusters between the red and blue curves are excluded.

### 3.7 Relative Luminosity

The relative luminosity is calculated using the ratio of number of BBC triggered events in the same helicity crossings to that in the opposite helicity crossings. The  $\pi^0$  yield for the same and opposite helicities are normalized by the luminosity recorded by BBC. Since the double helicity asymmetry depends on the cross-section measurement, the cross-section of  $\pi^0$  indeed depends on the measured yield of  $\pi^0$  normalized by the luminosity. Thus, measuring relative luminosity is an important ingredient for the calculation of double helicity

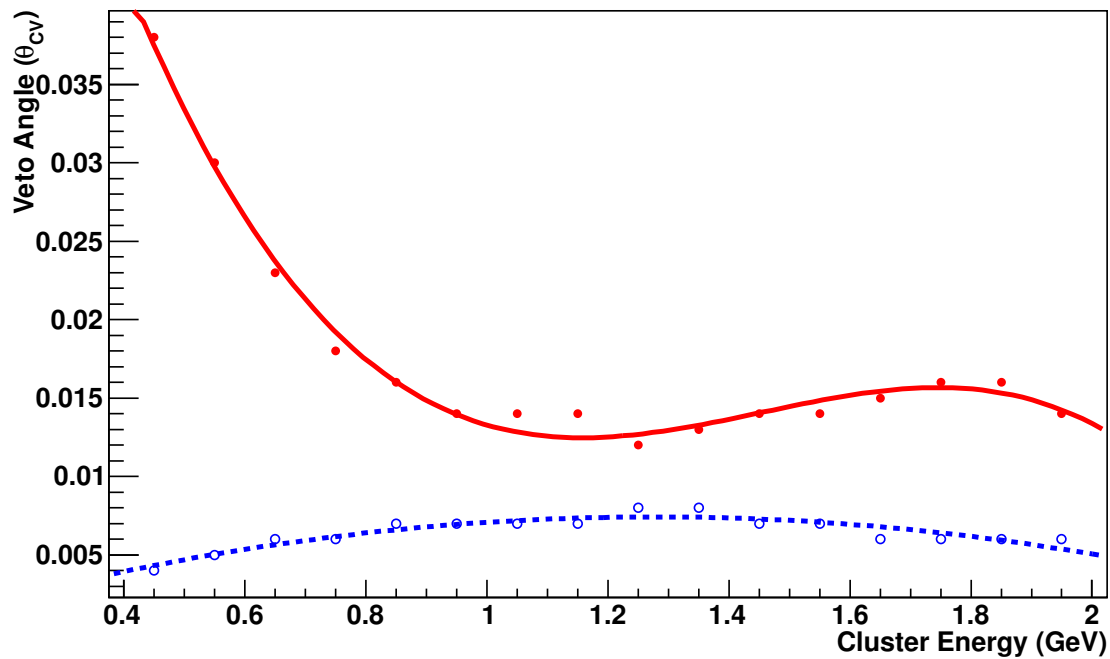


Figure (3.2) Charge veto angle as a function of energy of cluster. Red full circles are for large veto angle and blue empty circles are for small veto angle. The solid red and dashed blue curves are from fit. The clusters within the two curves are excluded in this analysis.

asymmetry. Also, the dominant source of systematic uncertainty in the calculation of double helicity asymmetry comes from the uncertainty in relative luminosity. It is calculated for even and odd crossing separately taking into account the difference in the even and odd crossings. Details of relative luminosity and corresponding systematic uncertainty are explained in Chapter 4.

### 3.8 Asymmetry Calculations

After applying all the cuts, the invariant mass spectrum of  $\pi^0$  is obtained as a function of transverse momentum ( $p_T$ ). The number of  $\pi^0$ s with the same and opposite helicities<sup>4</sup> of collisions ( $N^{++}$  and  $N^{+-}$ ) are obtained from the  $\pi^0$  mass spectrum. The detail of this process is given in Chapter 5.

The double helicity asymmetry,  $A_{LL}$  is calculated using Equation 3.9

$$A_{LL} = \frac{1}{P_B P_Y} \frac{N^{++} - RN^{+-}}{N^{++} + RN^{+-}}, \quad R \equiv \frac{L^{++}}{L^{+-}} \quad (3.9)$$

where  $P_{B(Y)}$  is the polarization of the blue (yellow) beam,  $R$  is the relative luminosity and  $N^{++}(N^{+-})$  are the number of  $\pi^0$ 's obtained from the same (opposite) sign helicity collisions. The statistical uncertainty of  $A_{LL}$  is calculated using Equation 3.10.

$$\sigma_{A_{LL}} = \frac{1}{P_B P_Y} \frac{2RN^{++}N^{+-}}{(N^{++} + RN^{+-})^2} \sqrt{\left(\frac{\sigma_{N^{++}}}{N^{++}}\right)^2 + \left(\frac{\sigma_{N^{+-}}}{N^{+-}}\right)^2 + \left(\frac{\sigma_R}{R}\right)^2}. \quad (3.10)$$

The expression for  $A_{LL}$  written above is valid assuming that all acceptance and efficiency corrections for the detector do not depend on helicity and crossing. This is applicable for detector acceptance and reconstruction efficiencies as they do not change on the scale of hundreds of nanoseconds. However, the trigger efficiency varies with even and odd crossings as they use separate circuits. Therefore, this analysis is done using even and odd crossings

---

<sup>4</sup>Projection of spin along the momentum direction

separately. Also, the combined triggers ( $4\times 4A \parallel 4\times 4B \parallel 4\times 4C$ ) are used for data selection. Figure 3.3 shows the invariant mass spectrum of  $\pi^0$ . The solid red region in Figure 3.3

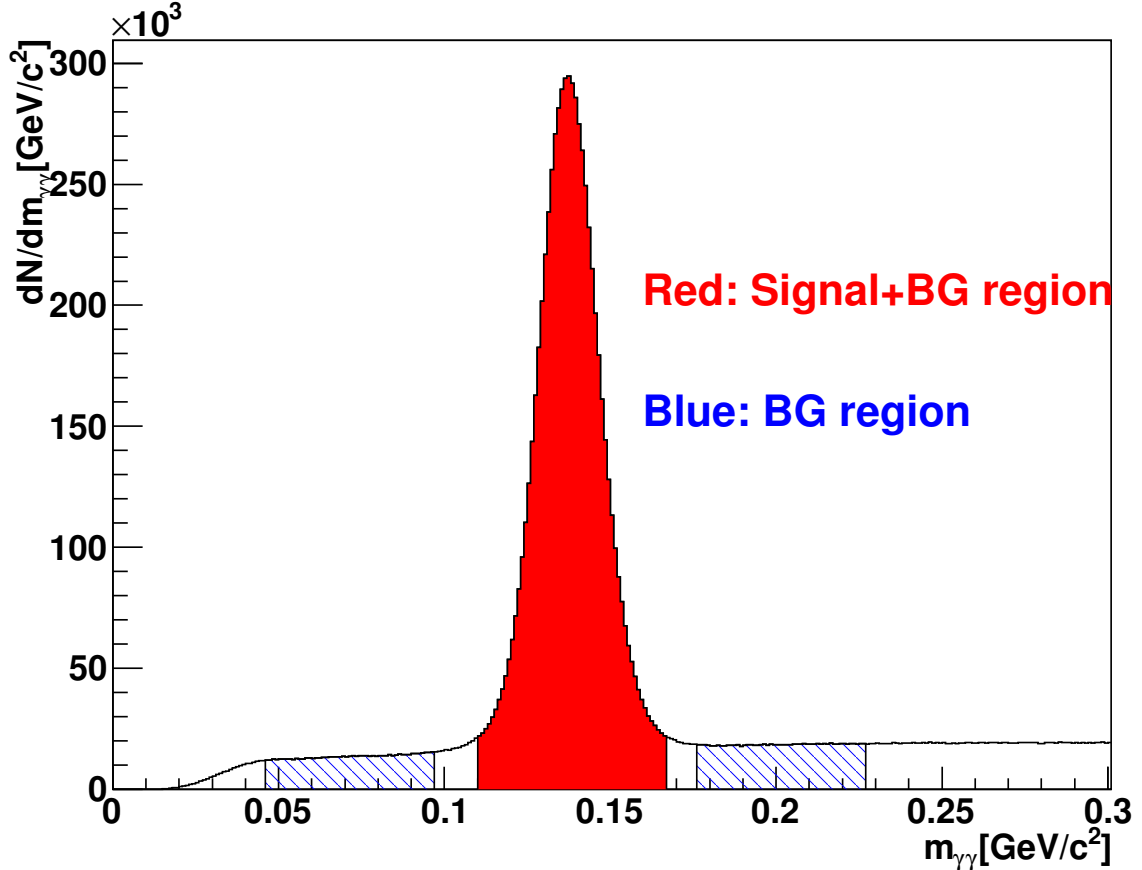


Figure (3.3) Invariant mass spectrum of  $\pi^0$ . The signal region is represented by solid red region ( $0.112 \leq M_{\gamma\gamma} \leq 0.162 \text{ GeV}/c^2$ ). The background region is represented by shaded blue pattern region ( $0.047 \leq M_{\gamma\gamma} \leq 0.097 \text{ GeV}/c^2$  and  $0.177 \leq M_{\gamma\gamma} \leq 0.227 \text{ GeV}/c^2$ )

is the signal region and the shaded blue pattern is the background. The solid red region consists of  $\pi^0$  signal as well as background. Since this region also contains background, the double helicity asymmetry for signal region is diluted by background. In order to remove the background asymmetry, we use the following equation

$$A_{LL}^{\pi^0} = \frac{A_{LL}^{\pi^0+BG} - r A_{LL}^{BG}}{1 - r} \quad (3.11)$$

Here,  $A_{LL}^{\pi^0+BG}$  is the double helicity asymmetry for signal region and  $A_{LL}^{BG}$  is for background region. The ratio  $r$  is the fraction of the background within the signal region. In the following section, we discuss the various components in  $A_{LL}$  calculation.

### 3.8.1 Background Fraction

The background fraction is given by

$$r = \frac{N_{BG}}{N_{\pi^0+BG}} \quad (3.12)$$

Here,  $N_{BG}$  is the yield in background region (blue shaded pattern area in Figure 3.3) and  $N_{\pi^0+BG}$  is the yield in signal region (red solid area in Figure 3.3.) The background fraction is estimated using the Gaussian process regression method which is explained in following section.

**Gaussian Process Regression** The background fraction is calculated using the Gaussian Process Regression (GPR) method. A Gaussian process is a specific type of stochastic process where the variance of each of the random variables comprising the process is Gaussian. In this method, the background yield within the GPR fit is divided by the signal yield within the signal region (solid red area in Figure 3.3). This method predicts several extrapolated/interpolated data points within the provided data at the same time. Examples of fits using the GPR approach are shown in Figures 3.6 and 3.7 for even and odd bunch crossings and a representative  $p_T$  bin, respectively. The plot for all the  $p_T$  bins are shown in Figures ?? and ???. The background fraction obtained with the GPR method is quite consistent with Breit Weigner (BW) fit<sup>5</sup> method except at higher  $p_T$  region where BW method overestimate the background fraction. The fit of the invariant mass spectrum using BW function is shown in Figure 3.4 and Figure 3.5 for even and odd crossings, respectively.

---

<sup>5</sup>It is the distribution of a random variable that is the ratio of two independent standard normal variables and has the probability density function  $f(x;0,1) = \frac{1}{\pi(1+x^2)}$

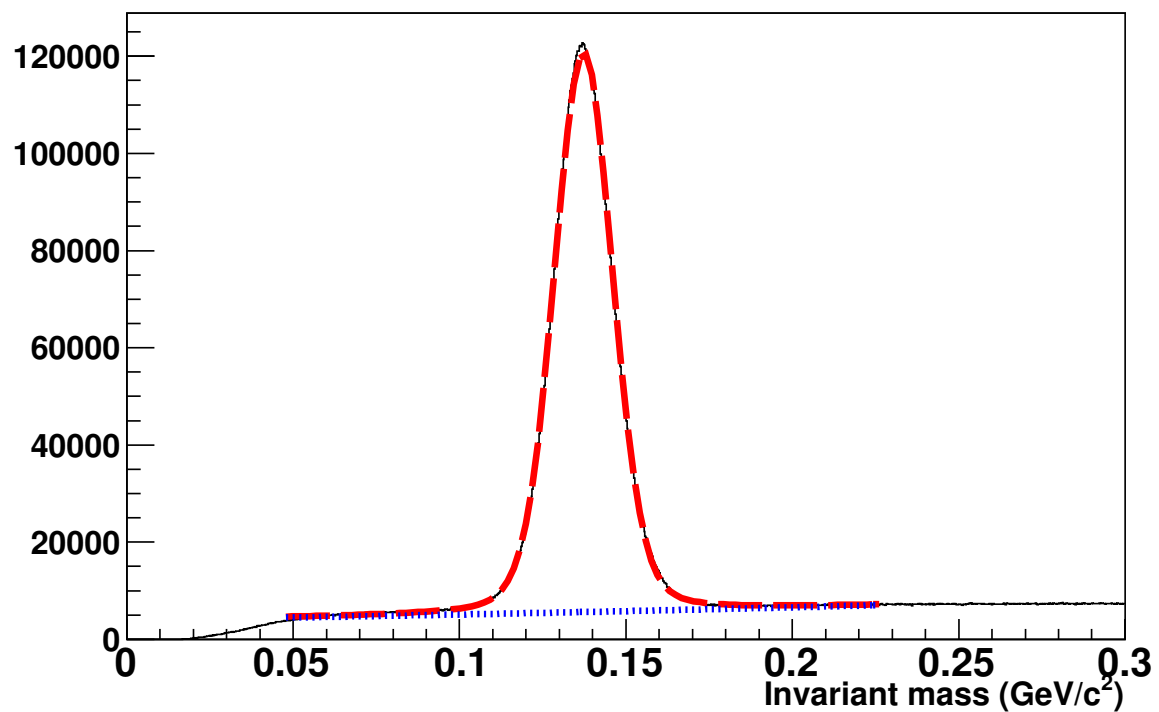


Figure (3.4) BW method to calculate the background fraction for even crossing. Here red dashed curve is the Gaussian + BW function and blue dotted line is the third order polynomial function.

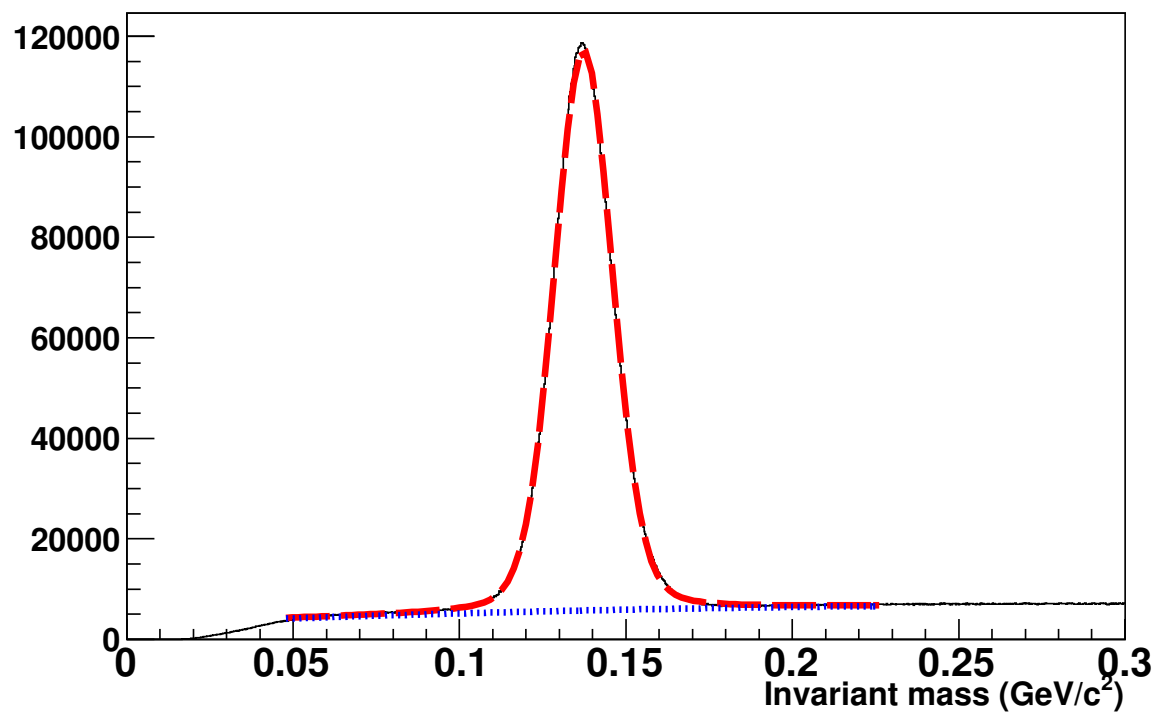


Figure (3.5) BW method to calculate the background fraction for odd crossing. Here red dashed curve is the Gaussian + BW function and blue dotted line is the third order polynomial function.

The comparison plots for the two different methods used to compare the background fraction are shown in Figure 3.8 (even) and Figure 3.9 (odd).

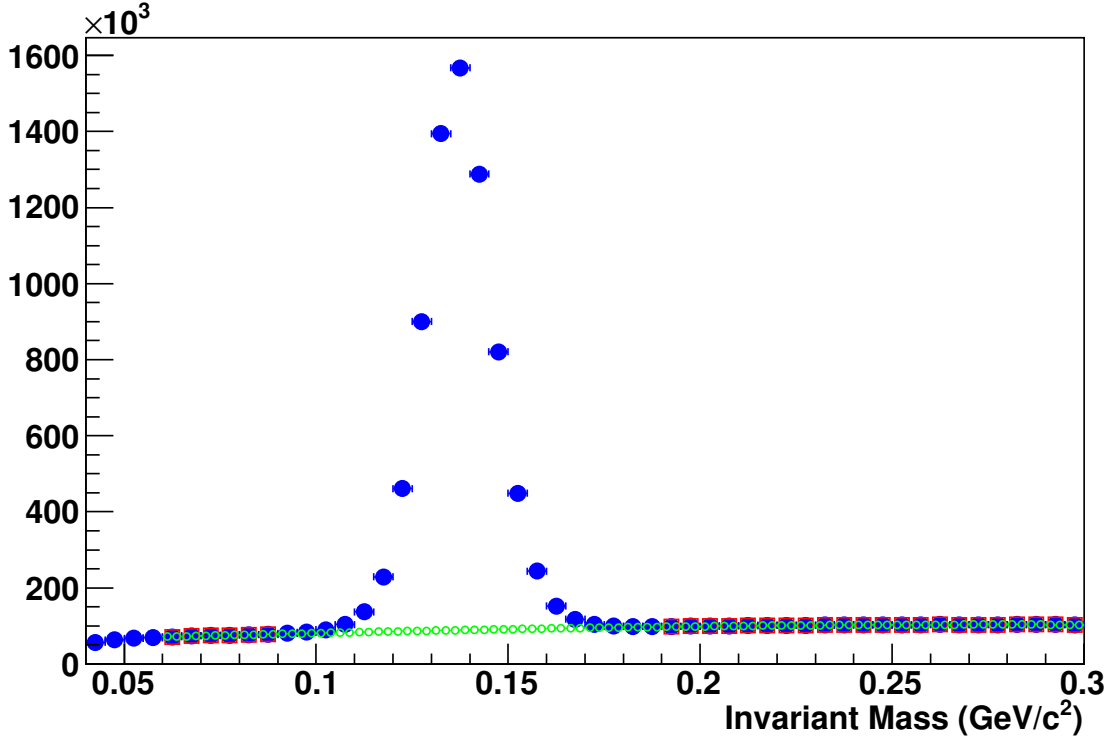


Figure (3.6) GPR approach to calculate the background fraction for even crossing. Here the solid blue circles represent the invariant mass histogram, the empty green circles represent the extrapolate/interpolate values using GPR and the red square boxes represent the input data points.

### 3.8.2 Luminosity Calculations

After QA and cuts, the integrated luminosity of the remaining runs is calculated in following manner: At first, the total live trigger count for BBCLL1(>0tubes)<sub>(novertex)</sub> for all the runs used in our analysis is obtained from the PHENIX online database. After that the total number of events for all the runs from offline data with minimum bias trigger ON are obtained. For this, the BBCLL1 (novertexcut) trigger should be present. The ratio ( $R$ ) of BBCLL1 with  $\pm 30$  cm cut and BBCLL1 for all events without  $\pm 30$  cm cut were calculated

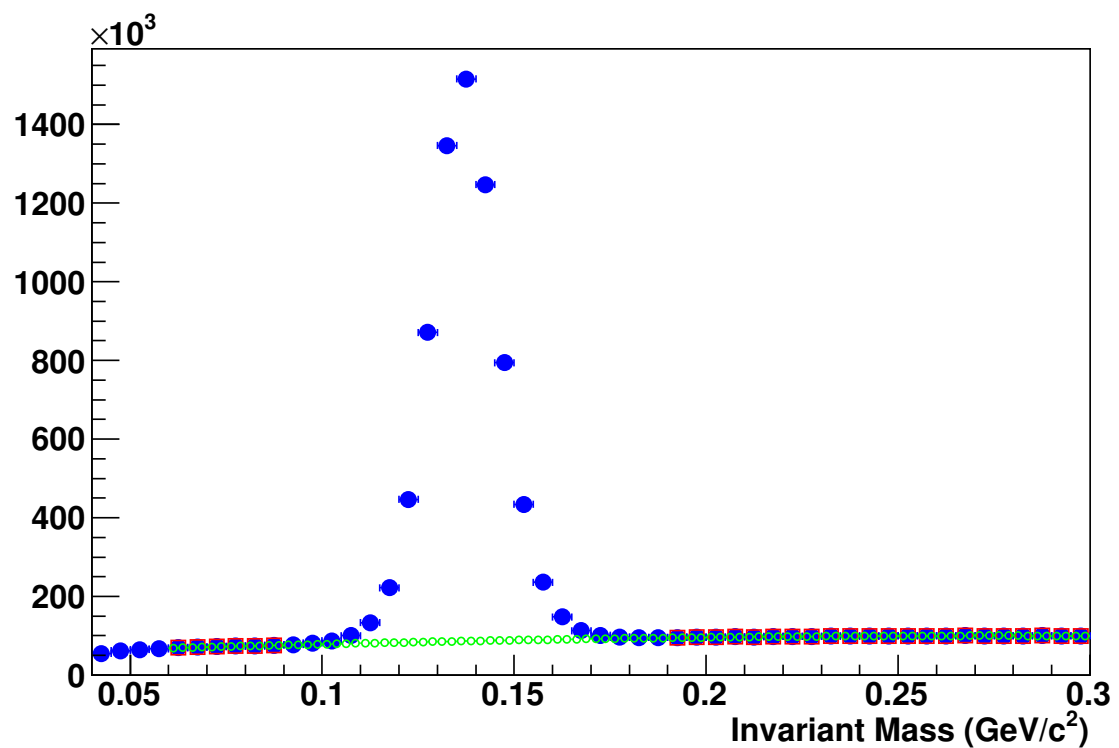


Figure (3.7) GPR approach to calculate the background fraction for odd crossing. Here the solid blue circles represent the invariant mass histogram, the empty green circles represent the extrapolate/interpolate values using GPR and the red square boxes represent the input data points.

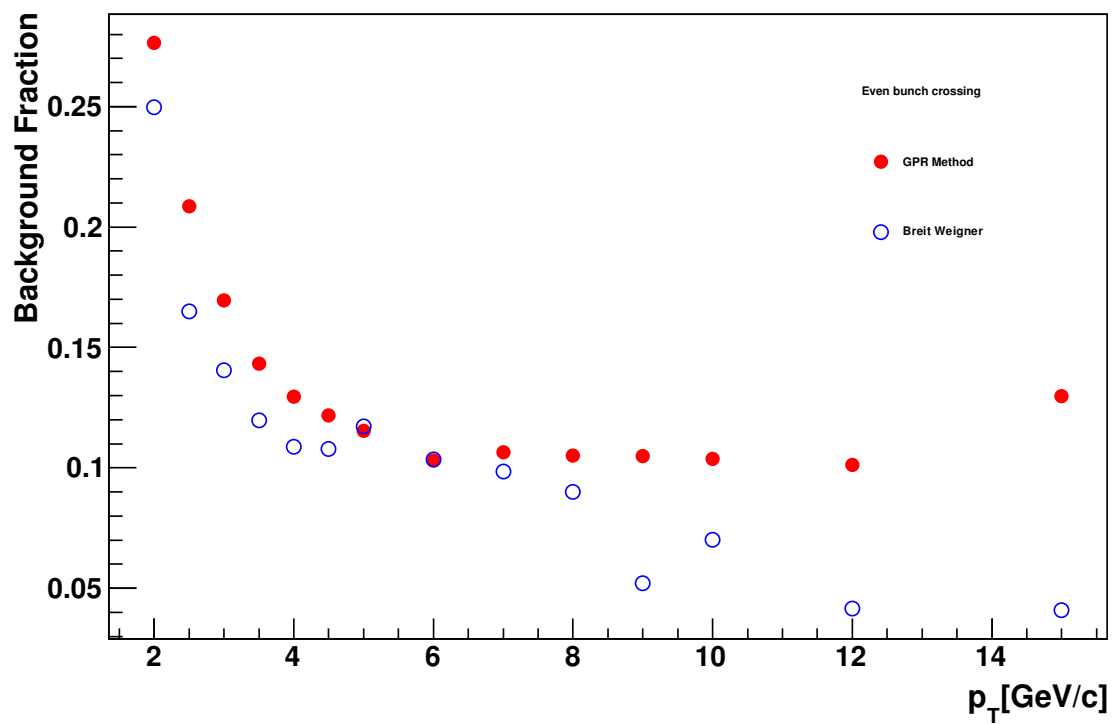


Figure (3.8) Comparison of the background fraction calculated by using GPR and Breit Weigner method for even crossing as a function of  $p_T$ . Here the red solid circles are from GPR method and the empty blue circles are from the Breit Weigner method.

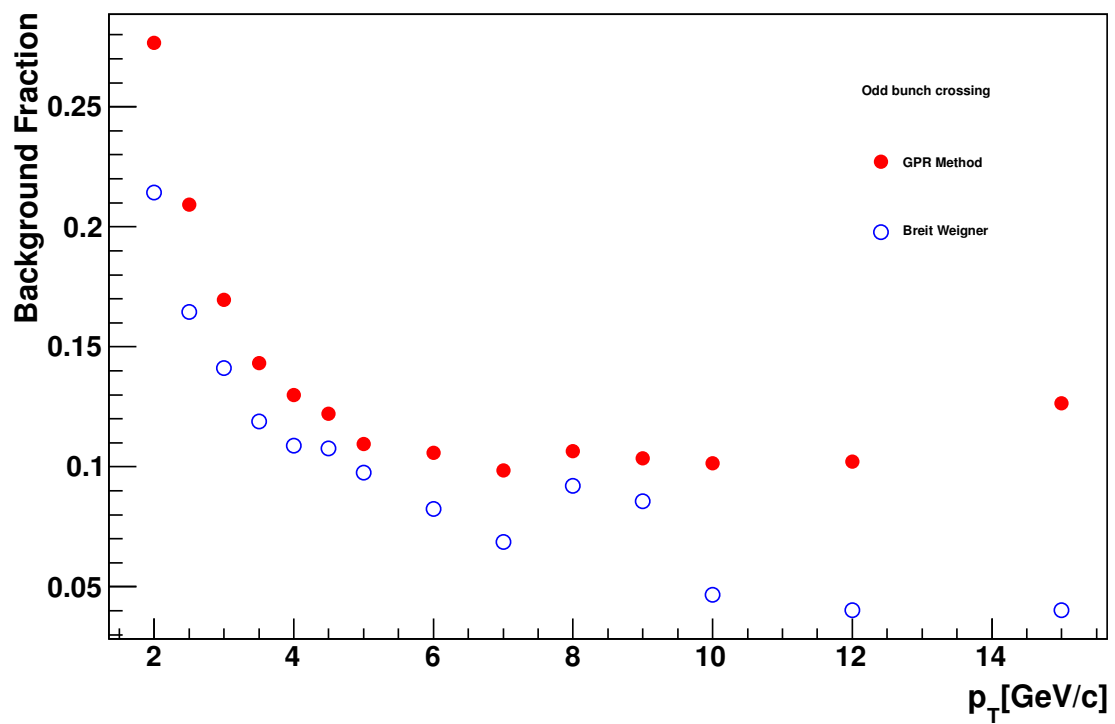


Figure (3.9) Comparison of the background fraction calculated by using GPR and Breit Weigner method for odd crossing as a function of  $p_T$ . Here the red solid circles are from GPR method and the empty blue circles are from the Breit Weigner method.

as follows:

$$R = \frac{BBCLL1_{30cm}}{BBCLL1_{novertex}} \quad (3.13)$$

The total number of events used in the analysis is calculated as:

$$T = N_{novertex} \times R \quad (3.14)$$

where  $N_{novertex}$  is the total number of events with no\_vertex cut. Finally, the integrated luminosity of the data used in our analysis is:

$$I = \frac{T}{\sigma_{BBC}} \text{ pb}^{-1} \quad (3.15)$$

Here, the BBC cross-section,  $\sigma_{BBC}$  is  $(32.5 \pm 3.2) \times 10^{-3}$  mb which is obtained using the van der Meer scan technique [38]. This calculation shows that a  $108.13 \text{ pb}^{-1}$  of data are used in this analysis.

### 3.8.3 Polarization

Beam polarization is an important ingredient in calculating  $A_{LL}$ . There are two methods in measuring the beam polarization at RHIC: proton-carbon ( $pC$ ) and H-jet. Both are explained in Chapter 2. The polarization is calculated on run-by-run basis according to the following procedure:

1. The polarization ( $P_0$ ) values at the beginning of each fill ( $t_{fill}$ ) is provided by the local polarimetry group at RHIC ([https://wiki.bnl.gov/rhicspin/Run\\_13\\_polarization](https://wiki.bnl.gov/rhicspin/Run_13_polarization)).
2. The rate of change of polarization as a function of time, i.e., slope ( $dP/dT$ ) for the fill is also provided by the polarimetry group.
3. The beginning time ( $t_0$ ) and the end time ( $t_1$ ) of each run are extracted from the PHENIX database and the average time ( $t_{avg}$ ) is

$$t_{avg} = \frac{t_0 + t_1}{2} \quad (3.16)$$

4. The polarization value at any time ( $t$ ) is calculated as:

$$P = P_0 + (t_{avg} - t_{fill}) \frac{dP}{dT} \quad (3.17)$$

where  $t_{fill}$  is the starting time of a fill.

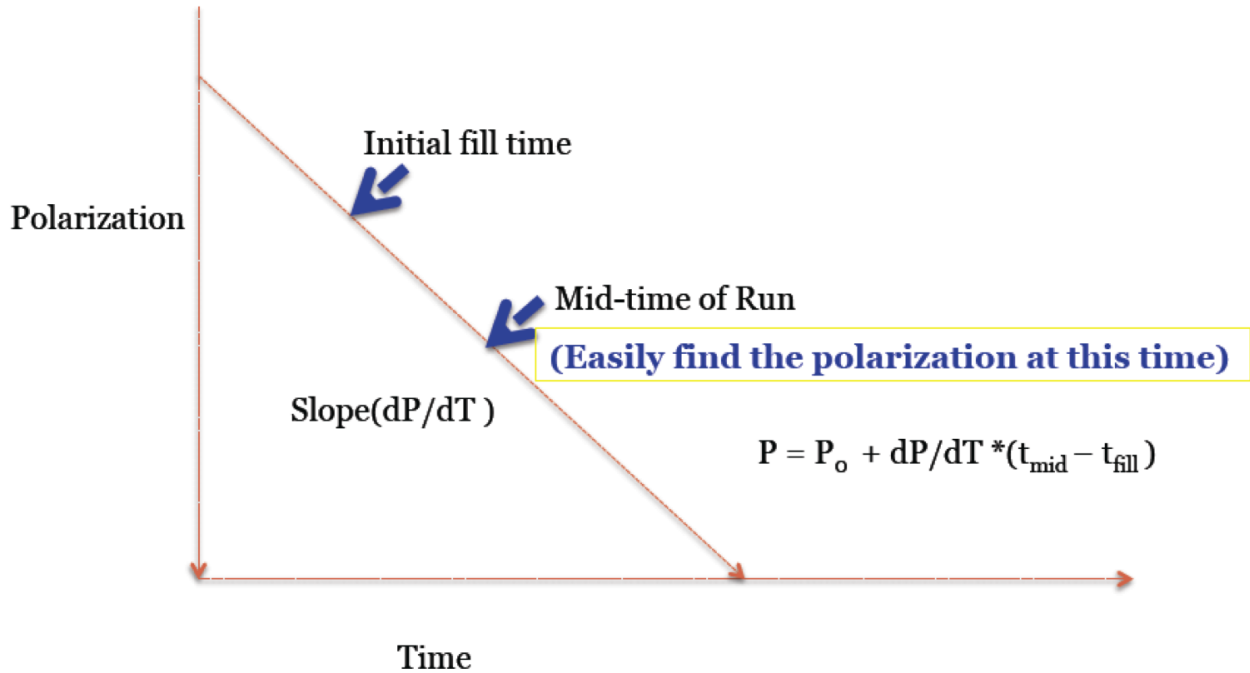


Figure (3.10) Polarization calculation procedure at mid-time of the run.

The process is illustrated in Figure 3.10. Figures 3.11 and 3.12 show the polarization values per run for the blue and yellow beams, respectively. The average polarization values normalized by BBC counts with  $z_{vertex} = \pm 30$  cm cut of the center of the interaction region (IR) along the beam axis are  $55\% \pm 0.001$  and  $56 \% \pm 0.001$  for the blue and the yellow beam polarization, respectively.

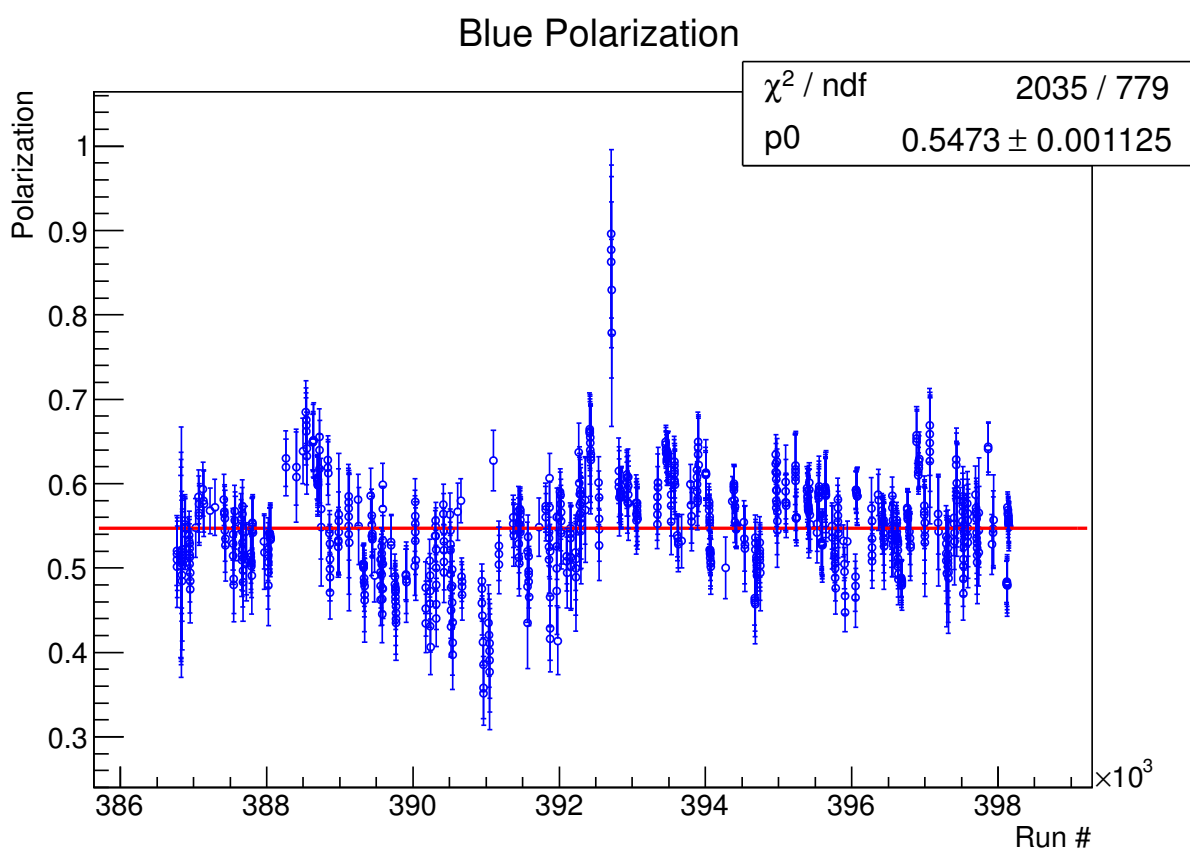


Figure (3.11) Blue beam polarization as a function of run number.

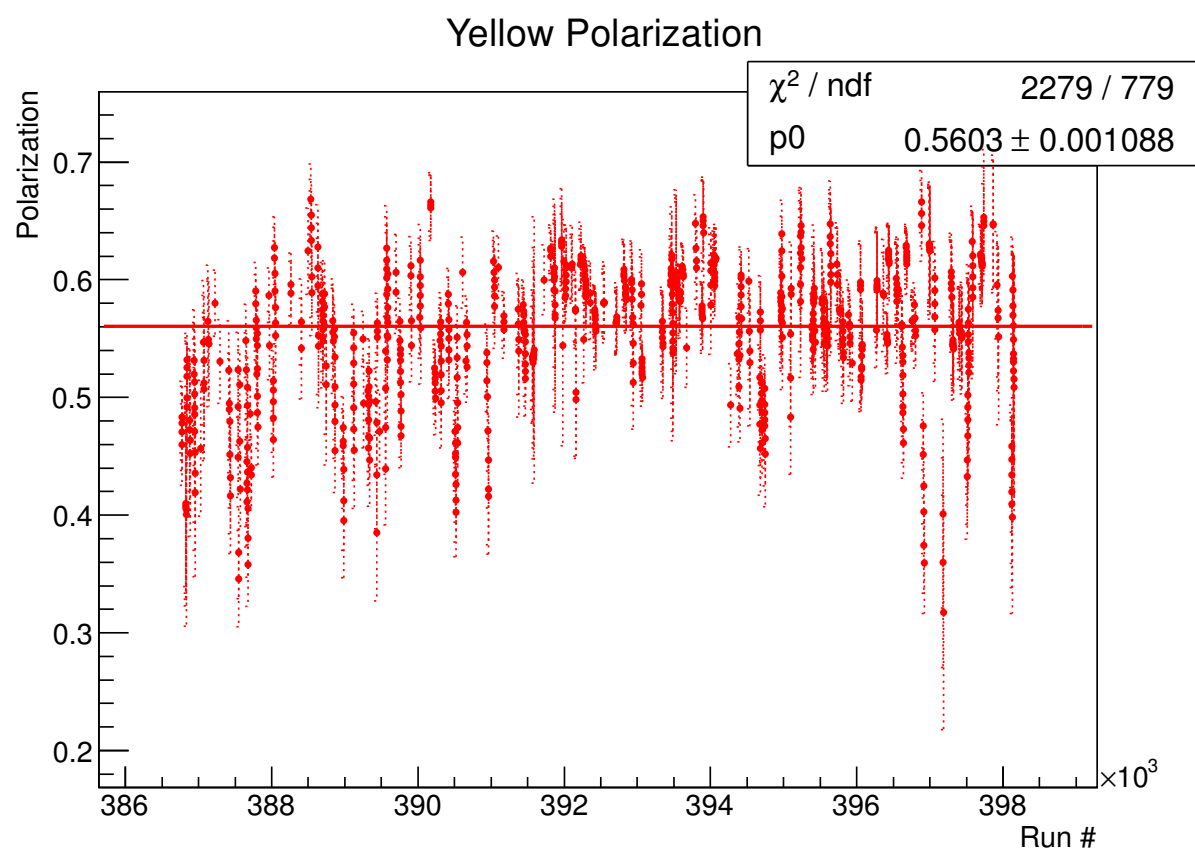


Figure (3.12) Yellow beam polarization as a function of run number.

### 3.8.4 Local Polarimetry at PHENIX

As explained in Chapter 2, for the measurement of the  $A_{LL}$  using longitudinally polarized beams, spin rotators are used to rotate the direction of the beam polarization from vertical to longitudinal. In reality, there is always some remaining transverse component of the polarization. This remaining component reduces the sensitivity of  $A_{LL}$ , while increasing the sensitivity of the transverse spin asymmetry  $A_{TT}$ . Therefore, it is very important to estimate this transverse components. The remaining transverse components are calculated according to the following method: PHENIX records events with the spin rotator magnet off for some time to establish a baseline measurement of the single transverse spin asymmetry ( $A_N$ )<sup>6</sup> of forward neutron production with the ZDCs. When the spin rotators are turned on for longitudinal running, the remaining component ratio,  $f_T$  of each beam is

$$f_T \equiv \frac{P_T}{P} = \frac{A_{N,rotators\_on}}{A_{N,rotators\_off}}, \quad (3.18)$$

and the corresponding longitudinal component ratio,  $f_L$  is given by

$$f_L \equiv \frac{P_L}{P} = \sqrt{1 - \left(\frac{P_T}{P}\right)^2} \quad (3.19)$$

The values of  $f_L$  are found to be

$$f_L^B = 0.9999^{+0.0001}_{-0.0001}(stat)^{+0.0000}_{-0.0001}(syst.), \quad (3.20)$$

for the blue beam and

$$f_L^Y = 0.9989^{+0.0004}_{-0.0005}(stat)^{+0.0003}_{-0.0001}(syst.), \quad (3.21)$$

for the yellow beam. With these numbers, the scale factor on our final Run 13  $A_{LL}^{\pi^0}$  is 1.001

---

<sup>6</sup>Particle spin  $\vec{S}$  is perpendicular to its momentum  $\vec{p}$

with the additional global scaling uncertainty,

$$\sqrt{\left(\frac{\delta f_L^B}{f_L^B}\right)^2 + \left(\frac{\delta f_L^B}{f_L^B}\right)^2} = \sqrt{\left(\frac{\pm 0.0001}{0.9999}\right)^2 + \left(\frac{\pm 0.0004}{0.9989}\right)^2} = \frac{\pm 0.004\%}{\mp 0.5\%}, \quad (3.22)$$

where combining of the asymmetric uncertainty has been done by treating the + and - errors separately and assuming the systematic error is uncorrelated between the blue and yellow beams.

### 3.9 Prescales and Run-by-Run Analysis

We used three sets of triggers to select events for this analysis: ERT4x4A&&BBCLL1, ERT4x4B and ERT4x4C&&BBCLL1 trigger. Among them the ERT4x4A&&BBCLL1 trigger and the ERT4x4C&&BBCLL1 trigger were prescaled<sup>7</sup> due to the high rate of events at high center of mass energy collisions ( $\sqrt{s} = 510$  GeV). This analysis is done on run-by-run basis due to different triggers prescales in different runs.

---

<sup>7</sup>Due to collision at high energy, there are number of events generated. It is not possible to record all the events so they are recorded selectively.

## CHAPTER 4

### SYSTEMATIC UNCERTAINTIES AND CROSS CHECKS

In this chapter, we discussed different possible sources of systematic uncertainties. These sources of systematic effects include the parity violating single spin asymmetry, relative luminosity and any systematic effects from bunch to bunch or fill to fill correlations are also discussed.

#### 4.1 Single Spin Asymmetry

The longitudinal single spin asymmetries are parity violating and strong interactions preserve parity and those associated with  $\pi^0$  production in  $p + p$  collisions are expected to be negligible. The longitudinal single spin asymmetry,  $A_L$ , is calculated according to the following Equation:

$$A_L^{beam} = \frac{1}{P_{beam}} \frac{N^+ - R_{beam}N^-}{N^+ + R_{beam}N^-}, \quad R_{beam} \equiv \frac{L^+}{L^-} \quad (4.1)$$

where  $R_{beam}$  is the relative luminosity of each beam,  $N^+$  ( $N^-$ ) are the particle yields in collisions with the positive (negative) helicity crossings in the set beam, and  $P_{beam}$  is the polarization for that beam. The single spin asymmetries for blue and yellow beams as a function of  $p_T$  are shown in Figure 4.1 and listed in Table 4.1. The first column of Table 4.1 is the transverse momentum, the second and third columns are the single spin asymmetry values and associated errors for the blue beam. Similarly, the fourth and fifth columns are the single spin asymmetry values and associated errors for the yellow beam. The data show that the  $A_L$  values are negligible, and thus no associated systematic effect is assigned.

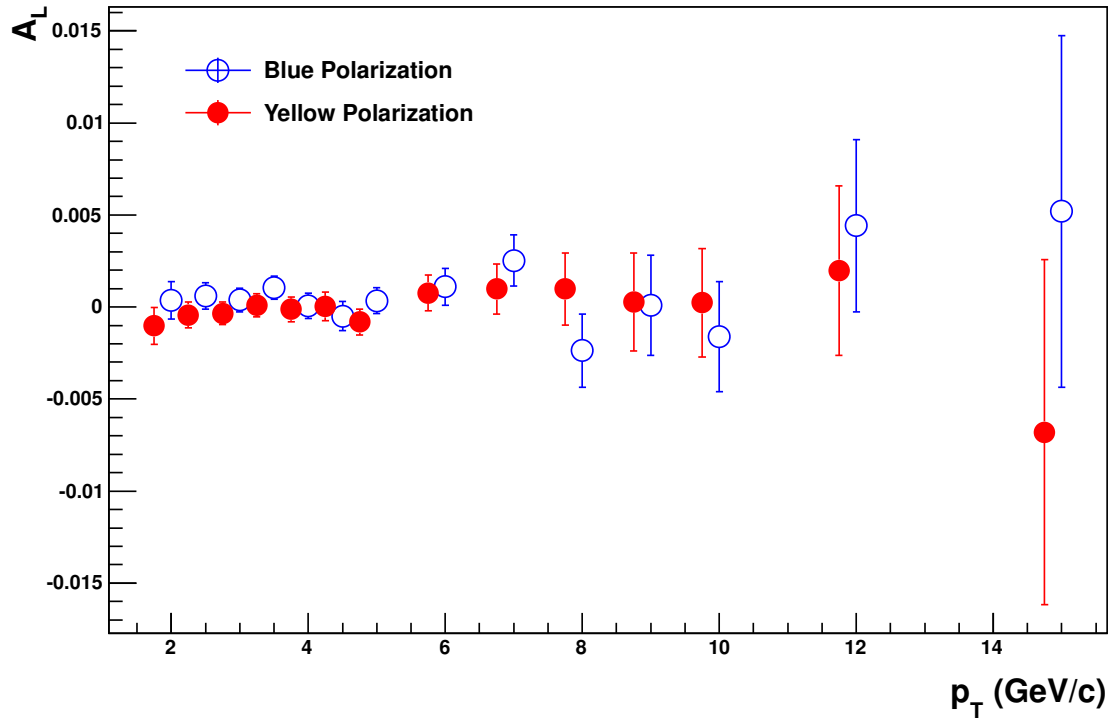


Figure (4.1) Single spin asymmetry as function of  $p_T$  for blue and yellow beams.

Table (4.1) Single spin asymmetry values for blue and yellow beams.

$p_T$	$A_L^{\pi^0}(B)$	$\Delta A_L^{\pi^0}(B)$	$A_L^{\pi^0}(Y)$	$\Delta A_L^{\pi^0}(Y)$
2.0-2.5	3.62e-4	1.01e-3	-1.02e-3	9.93e-4
2.5-3.0	6.07e-4	7.21e-4	-4.36e-4	7.07e-4
3.0-3.5	3.82e-4	6.36e-4	-3.44e-4	6.24e-4
3.5-4.0	1.05e-3	6.38e-4	9.07e-5	6.26e-4
4.0-4.5	6.39e-5	6.93e-4	-1.28e-4	6.80e-4
4.5-5.0	-4.99e-4	7.88e-4	2.31e-5	7.73e-4
5.0-6.0	3.43e-4	7.08e-4	-8.12e-4	6.95e-4
6.0-7.0	1.10e-3	9.92e-4	7.53e-4	9.73e-4
7.0-8.0	2.52e-3	1.39e-3	9.76e-4	1.36e-3
8.0-9.0	-2.37e-3	1.98e-3	2.81e-4	1.95e-3
9.0-10.	1.00e-4	2.71e-3	2.29e-4	2.66e-3
10.-12.	-1.61e-3	2.99e-3	1.98e-3	2.93e-3
12.-15.	4.41e-3	4.68e-3	-6.80e-3	4.59e-3
15.-20.	5.19e-3	9.56e-3	-6.27e-3	9.37e-3

## 4.2 Relative Luminosity

The relative luminosity is calculated as the ratio between BBCLL1 trigger counts in the same helicity crossing to those in the opposite helicity crossing. The relative luminosity is a dominant source of systematic uncertainty of  $A_{LL}$  measurement. To identify the fake asymmetry (systematic uncertainty) due to luminosity from the BBC, different corrections like pileup, width and residual rate are studied. These corrections are used to categorically identify the systematic uncertainty on relative luminosity calculations.

In order to test if the double helicity asymmetry is spin independent, we measure  $A_{LL}^{BBC}$ . The definition of  $A_{LL}^{BBC}$  is

$$A_{LL}^{BBC} = \frac{1}{P_B P_Y} \frac{\frac{N_{BBC}^{++}}{L^{++}} - \frac{N_{BBC}^{+-}}{L^{+-}}}{\frac{N_{BBC}^{++}}{L^{++}} + \frac{N_{BBC}^{+-}}{L^{+-}}}, \quad (4.2)$$

where  $N_{BBC}^{++}$  ( $N_{BBC}^{+-}$ ) are the number of collisions in '+ +' and '+ -' crossings,  $L^{++}$  ( $L^{+-}$ ) are the luminosities for same (opposite) helicity. We test the asymmetry results obtained from BBC by comparing it with another detector called ZDC. ZDC is used as next luminosity detector because it has low background and good statistics. Thus, what we measure is:

$$A_{LL}^{ZDC/BBC} = \frac{1}{P_B P_Y} \frac{\frac{N_{ZDC}^{++}}{N_{BBC}^{++}} - \frac{N_{ZDC}^{+-}}{N_{BBC}^{+-}}}{\frac{N_{ZDC}^{++}}{N_{BBC}^{++}} + \frac{N_{ZDC}^{+-}}{N_{BBC}^{+-}}} \quad (4.3)$$

The uncertainty of  $A_{LL}^{ZDC/BBC}$  includes  $\Delta\epsilon_{LL}$  from bunch fitting, which is the fitting of the ratio of ZDC and BBC, and statistical uncertainties of each RHIC beam polarization and is given by Equation 4.4

$$\Delta A_{LL}^{ZDC/BBC} = \frac{1}{P_B P_Y} \sqrt{(\Delta\epsilon_{LL} \times \sqrt{\chi_{re}^2})^2 + \epsilon_{LL}^2 \left( \frac{(\Delta P_B)^2}{P_B^2} + \frac{(\Delta P_Y)^2}{P_Y^2} \right)}. \quad (4.4)$$

where  $\chi_{re}^2$  is the chi-square of bunch fitting. The scaling of uncertainty of  $\epsilon_{LL}$  is omitted until correction parameters are fixed because it dilute the behaviour of each corrections. Without

any correction, the ratio,  $A_{LL}^{ZDC/BBC}$ , is found to be  $(-2.433 \times 10^{-4} \pm 1.002) \times 10^{-5}$  which is shown in Figure 4.2.

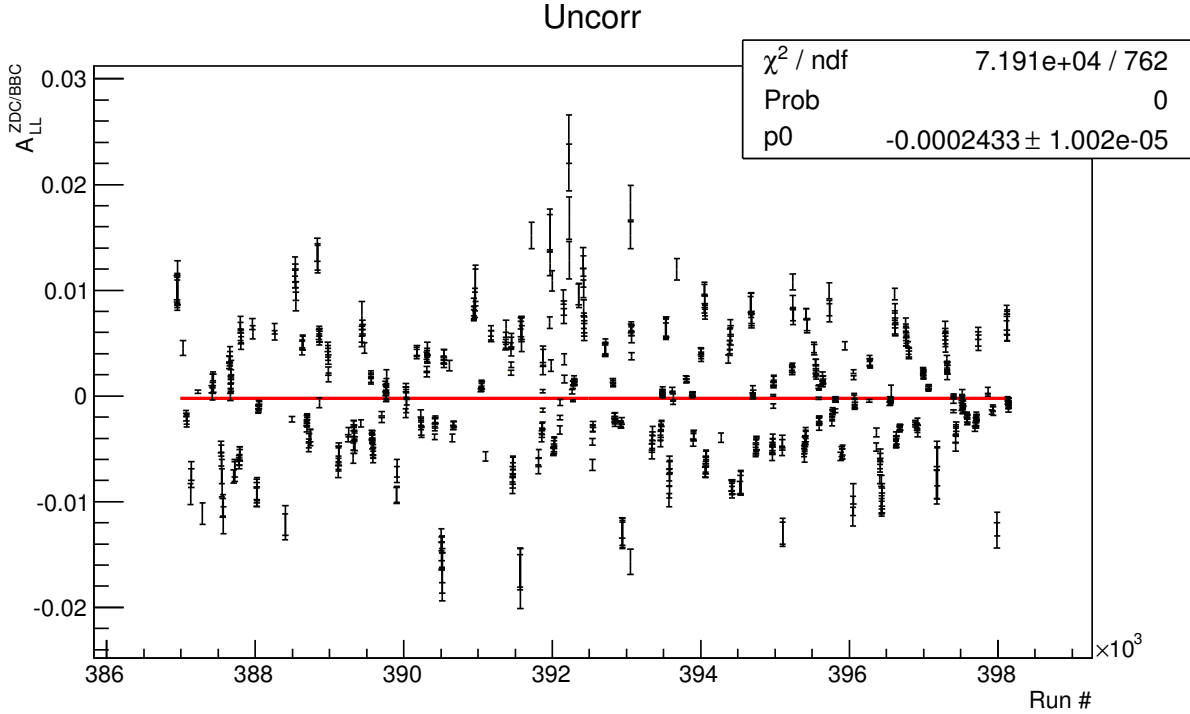


Figure (4.2)  $A_{LL}^{ZDC/BBC}$  as a function of run number. The central red line is a fit with a zeroth-order polynomial. No corrections have been applied in this plot.

#### 4.2.1 Pileup Correction

Due to multiple collisions and random coincidences of single diffractive events, scaler over-counting or under-counting can occur. The scaler miss-counting is fixed by calculating true rate for each scaler values using Equation 4.5,

$$Rate_{obs} = 1 - e^{-Rate_{true}(1+k_N)} - e^{-Rate_{true}(1+k_S)} + e^{-Rate_{true}(1+k_N+k_S)} \quad (4.5)$$

where  $k_{N(S)}$  is the north (south) hit probability. The observed scaler rate is calculated by dividing each scaler count by the Clock scaler<sup>1</sup> counts. Then, true scaler rate are obtained

---

<sup>1</sup>Measure counts within specific time

by numerically solving Equation 4.5.  $K_N$  and  $K_S$  can be determined with Star Scaler<sup>2</sup>. Each  $K_N$  and  $K_S$  are calculated for bunch ID and run number. To remove the rate dependence of  $K_N$  and  $K_S$ , the true coincident rate and exclusive rate are calculated according to the following Equation:

$$R_{NS}^{True} = \ln(1 - R_N^{Inc., Observed} - R_S^{Inc., Observed} + R_{NS}^{Observed}) - \ln(1 - R_N^{Inc., Observed}) - \ln(1 - R_S^{Inc., Observed}) \quad (4.6)$$

and

$$R_{N(S)}^{True, Exc.} = -\ln(1 - R_{N(S)}^{Inc., Observed} - R_{NS}^{True}) \quad (4.7)$$

where  $R_{N(S)}$  is the north (south) rate.  $K_N$  and  $K_S$  are obtained by fitting with a constant function. With the determination of  $K_N$  and  $K_S$  and observed scaler rates, true scaler rates are obtained by substituting them into the the pileup correction Equation 4.5. Figures 4.3 and 4.4 show the BBC and ZDC rates. Figures 4.3 shows scaler under-counting is dominant for BBC similarly 4.4 shows scaler over-counting is dominant for ZDC. With this correction, the ratio,  $A_{LL}^{ZDC/BBC}$ , is found to be  $-5.828 \times 10^{-5} \pm 9.293 \times 10^{-6}$ . Figure 4.5 shows result of

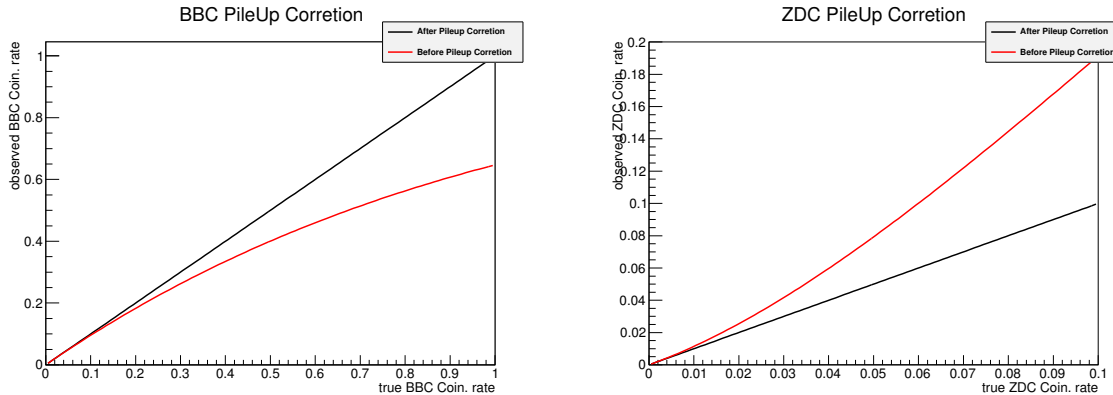


Figure (4.3) BBC rate with and without Pileup correction. For BBC, scaler under-counting is dominant at high rate.

Figure (4.4) ZDC rate with and without Pileup correction. For ZDC, scaler over-counting is dominant at high rate.

<sup>2</sup>There are three STAR scaler boards at the PHENIX experiment. These are used to measure raw, live and scaled trigger. Raw triggers count the number of times a trigger fires, the live triggers count the number of times a trigger fires when the DAQ is not busy and the scaled triggers count the number of triggers when the DAQ is not busy and after the prescale is applied.

run fitting with pileup correction. We observe a reduce in both  $A_{LL}^{ZDC/BBC}$  and  $\chi^2_{re}$  of run fitting.

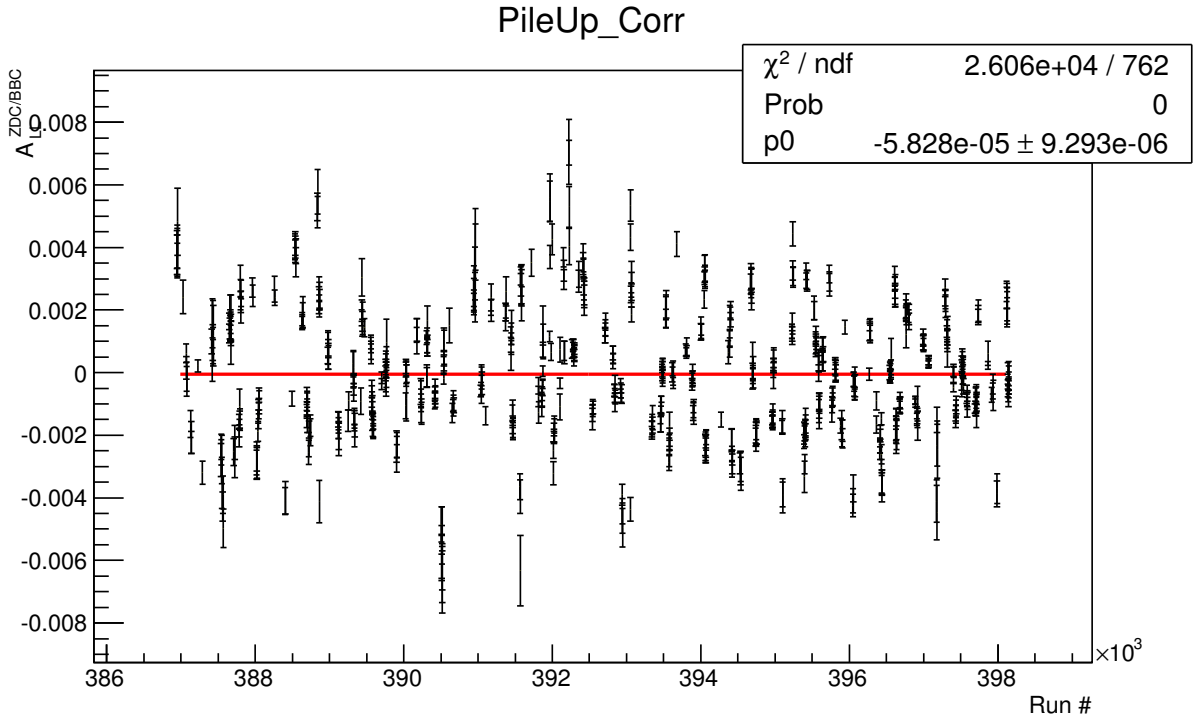


Figure (4.5)  $A_{LL}^{ZDC/BBC}$  as a function of run number with pileup correction. Both  $A_{LL}^{ZDC/BBC}$  and  $\chi^2_{re}$  are reduced compared with no corrections as shown in the Figure 4.2.

#### 4.2.2 Width Correction

The width correction is an additional correction to scaler miscount. It is a classical way to handle scaler miscount due to vertex cut, especially for ZDC. Due to the poor resolution of the ZDC, undercounting by ZDC occurs which depends on the  $z_{vertex}$  width. The narrower the  $z_{vertex}$ , the more undercounting occurs. Thus, we need to correct ZDC/BBC ratio by the  $z_{vertex}$  width. To parameterize the  $z_{vertex}$  width, we define  $\sigma_{proxy}$  which is

$$\sigma_{proxy} = \frac{ZDC_{out}}{ZDC_{narrow}}, \quad (4.8)$$

where  $ZDC_{narrow} = ZDC_{30cm}$  and  $ZDC_{out} = ZDC_{NoVtx} - ZDC_{narrow}$ . Thus, the ratio can be simplified as:

$$\left(\frac{ZDC}{BBC}\right)' = \left(\frac{ZDC}{BBC}\right) \frac{\langle \frac{ZDC}{BBC} \rangle}{P_0 + P_1 \sigma_{proxy}} \quad (4.9)$$

This correction is called the width correction. With the width and pileup corrections, the ratio,  $A_{LL}^{ZDC/BBC}$ , is found to be  $-1.704 \times 10^{-5} \pm 8.794 \times 10^{-6}$  as shown in Figure 4.6.

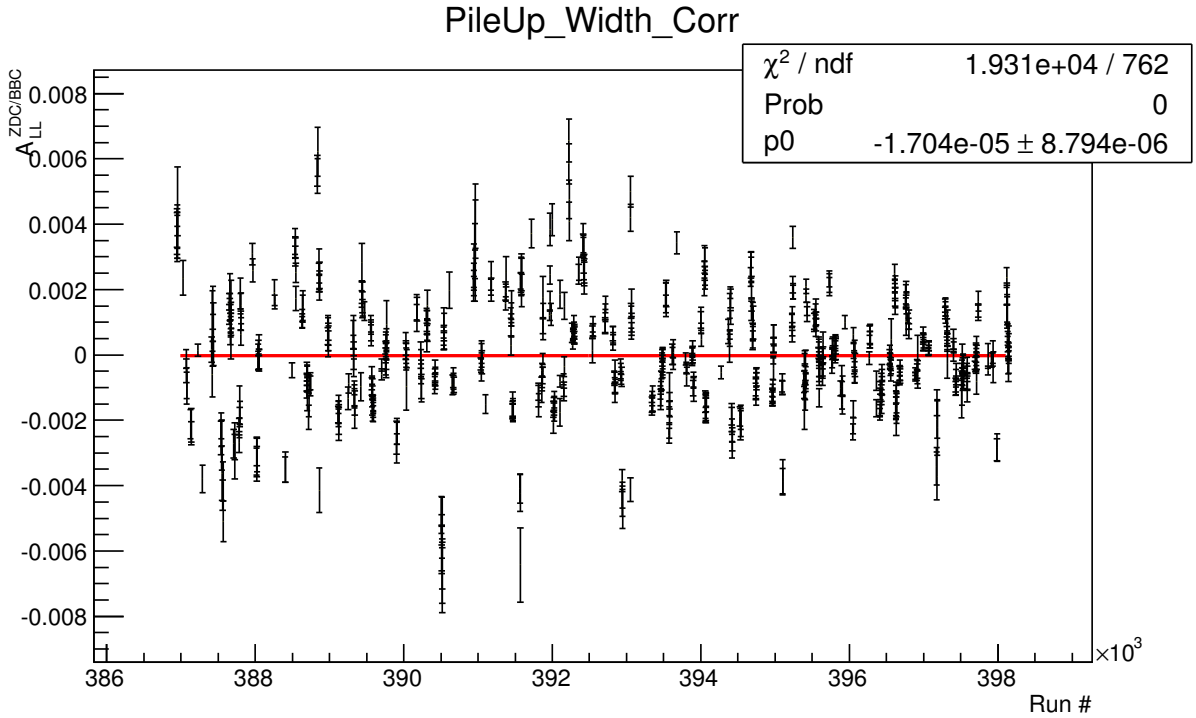


Figure (4.6)  $A_{LL}^{ZDC/BBC}$  as a function of run number with pileup and width correction. Both  $A_{LL}^{ZDC/BBC}$  and  $\chi^2_{re}$  are reduced compared with no corrections as shown in Figure 4.2.

#### 4.2.3 Residual Rate Correction

The pileup correction formalism is analytic. If the BBC and ZDC coincidence triggers have no vertex cut, the formalism works well on the data. But this formalism does not work when a vertex cut is present. Thus, we use the residual rate correction. First, let's define the factor  $f$  as the fraction of crossings where a coincidence is found, real or accidental, such

that the vertex is reconstructed within the 30 cm vertex cut.

$$f = \frac{Observed_{30cm\_vertex\_scaler\_count}}{Observed_{no\_vertex\_scaler\_count}} \quad (4.10)$$

The bunch-by-bunch factor  $f$  is obtained from STAR Scaler data. The vertex cut true rate is approximately:

$$Rate_{obs} \rightarrow f Rate_{obs}, \quad (4.11a)$$

$$Rate_{obs} = F(Rate_{obs}), \quad (4.11b)$$

Which gives:

$f Rate_{obs} \sim F(Rate_{true,vtx})$  where,  $F$  is the right hand side of Equation 4.5. If we solve the above equations,  $Rate_{true}$  and  $Rate_{true,vtx}$  are obtained.

$$Rate_{true} = F^{-1}(Rate_{obs}) \quad (4.12a)$$

$$Rate_{true,vtx} \approx F^{-1}(f Rate_{obs}) \quad (4.12b)$$

From Equation 4.12, an additional factor appears in the relation between  $Rate_{true}$  and  $Rate_{true,vtx}$ .

$$Rate_{true,vtx} \approx f Rate_{true}/C_{res} \quad (4.13)$$

where,

$$C_{res} \equiv \frac{f F^{-1}(Rate_{obs})}{F^{-1}(Rate_{obs,vtx})} \quad (4.14)$$

Figures 4.7 and 4.8 show calculated  $C_{res}$  of BBC and ZDC.

The true rate is now corrected by multiplying it by  $C_{res}$  to get the observed vertex cut rate.

$$Rate_{obs,vtx,residual} = Rate_{obs,vtx} \times C_{res} \quad (4.15)$$

This is called the residual rate correction. With the residual rate correction, the ratio,

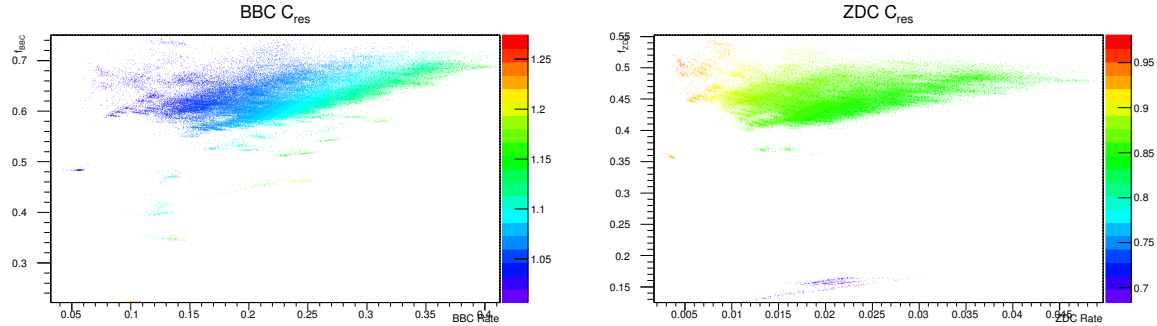


Figure (4.7)  $C_{res}$  of BBC as a function of observed vertex cut rate of BBC.

Figure (4.8)  $C_{res}$  of ZDC as a function of observed vertex cut rate of ZDC.

$A_{LL}^{ZDC/BBC}$ , is found to be  $(5.610 \pm 1.002) \times 10^{-5}$  as shown in Figure 4.9.

#### 4.2.4 $\Delta A_{LL}$ due to Relative Luminosity

From the discussion above, measured  $A_{LL}^{ZDC/BBC}$

$$A_{LL}^{ZDC/BBC} = -1.026 \times 10^{-4} \pm 3.762 \times 10^{-5} (\text{stat.}) \pm 8.727 \times 10^{-8} (\text{syst. correction}) \pm 3.694 \times 10^{-4} (\text{syst. pattern}) \quad (4.16)$$

is obtained. The overall systematic uncertainty in  $A_{LL}^{\pi^0}$  due to relative luminosity is obtained by quadratic sum of all the three corrections and is found to be

$$\Delta A_{LL}(\text{Rel. Lumi}) = 3.853 \times 10^{-4}. \quad (4.17)$$

#### 4.2.5 Summary of Corrections

The Table 4.2 shows the summary of all the corrections while measuring the  $A_{LL}^{ZDC/BBC}$ .

### 4.3 Bunch Shuffling

Bunch shuffling is a systematic technique to ensure that any systematic uncertainty from bunch to bunch or fill to fill correlations are less than the statistical uncertainty. The bunch shuffling technique includes randomly shuffling the helicities of the bunches used in

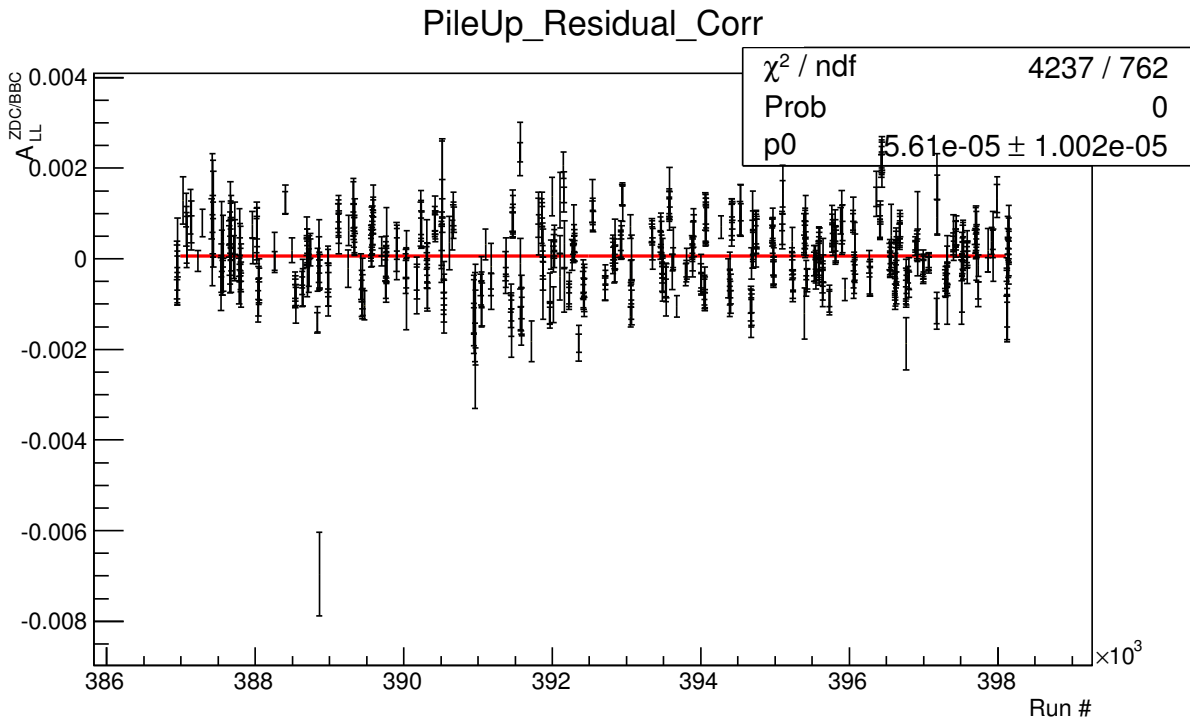


Figure (4.9)  $A_{LL}^{ZDC/BBC}$  as a function of run number with pileup, width and residual rate corrections.  $A_{LL}^{ZDC/BBC}$  is a bit increased. However  $\chi^2_{re}$  are dramatically reduced compared with no corrections as shown in Figure 4.2.

Table (4.2) Summary table of all the corrections in the calculation of the uncertainty in relative luminosity.

Variables	Uncorr	Pileup	Width	Residual
$A_{LL}^{ZDC/BBC}$	$-2.43 \times 10^{-4}$	$-5.83 \times 10^{-5}$	$-1.70 \times 10^{-5}$	$5.61 \times 10^{-5}$
$\chi^2_{re}(\text{run})$	$9.44 \times 10^1$	$3.42 \times 10^1$	$2.53 \times 10^1$	$5.56 \times 10^0$
$\chi^2_{re}(\text{bunch})$	$3.08 \times 10^3$	$2.05 \times 10^2$	$1.28 \times 10^2$	$2.36 \times 10^1$
Syst. Patt	$3.00 \times 10^{-3}$	$1.08 \times 10^{-3}$	$7.34 \times 10^{-4}$	$3.69 \times 10^{-4}$

the analysis per fill and then calculating  $A_{LL}$ .

Bunch shuffling allows the creation of multiple samples needed to differentiate indications of systematic uncertainties from normal fluctuations in  $\chi^2$  of samples. To create a new sample, the helicity for all bunches in the data sample are randomly assigned. The  $A_{LL}$  is then calculated and a new  $\chi^2$  is obtained. Doing this numerous times (60,000 in this case), gives a  $\chi^2$  distribution. If the distribution differs from the expected distribution for a set number of degrees of freedom, it is an indication of a systematic effect.

The  $\chi^2$  distributions of  $A_{LL}$  in the signal and background regions with even and odd bunch crossings from bunch shuffling are shown in Figures 4.10, 4.11, 4.12 and 4.13. The histogram on each panel is the  $\chi^2$  distributions from the data and the red curve is the expected one given by Equation 4.18. Similarly, the distributions of  $A_{LL}/\sigma$ , where  $\sigma$  is the width of the distribution, for the peak and background regions are shown in the Figures 4.14, 4.15, 4.16 and 4.17. These distributions are expected to follow the Gaussian distribution with a mean at 0 and a variance of 1 if the uncertainty is appropriately approximated. The probability distribution of  $\chi^2$  is given by:

$$F(x; k) = \begin{cases} \frac{x^{\frac{k}{2}-1} e^{-\frac{x}{2}}}{2^{\frac{k}{2}} \Gamma(\frac{k}{2})}, & x \geq 0; \\ 0, & \text{otherwise} \end{cases} \quad (4.18)$$

where  $k$  is a positive integer that specifies the number of degrees of freedom.

#### 4.4 Systematic Uncertainty due to Background Fraction

As mentioned earlier, the background fraction is calculated using the GPR method. In order to study the systematic effects in background fraction calculations, fitting methods like Breit Wigner and Gaus + pol2 with different fitting ranges are used. The results are

Table (4.3) Systematic uncertainty due to background fraction calculation:  $A_{LL}^{\pi^0}$  at  $\sqrt{s} = 510$  GeV. Lower and upper values of systematic uncertainty from background fraction are listed.

$p_T$ Bin	Mean $p_T$	$A_{LL}^{\pi^0}$	$A_{LL}^{\pi^0}$ (stat.)	$A_{LL}^{\pi^0}$ (syst. low)	$A_{LL}^{\pi^0}$ (syst. high)
2.0-2.5	2.28e+0	-5.97e-5	1.20e-3	-3.14e-5	6.48e-5
2.5-3.0	2.76e+0	-8.98e-4	8.64e-4	-5.54e-7	4.82e-6
3.0-3.5	3.25e+0	3.47e-4	7.62e-4	-2.50e-5	4.26e-5
3.5-4.0	3.74e+0	-4.71e-4	7.61e-4	-6.10e-5	8.29e-5
4.0-4.5	4.24e+0	1.10e-3	8.22e-4	-7.96e-5	6.48e-5
4.5-5.0	4.74e+0	7.99e-4	9.34e-4	-1.46e-6	5.09e-6
5.0-6.0	5.45e+0	3.93e-4	8.33e-4	-5.42e-20	1.43e-5
6.0-7.0	6.45e+0	1.58e-3	1.17e-3	-5.74e-5	2.72e-5
7.0-8.0	7.45e+0	1.30e-3	1.65e-3	-9.20e-5	5.45e-5
8.0-9.0	8.45e+0	3.03e-3	2.31e-3	-4.87e-5	2.05e-5
9.0-10.	9.45e+0	6.42e-3	3.22e-3	-6.23e-4	2.14e-4
10.0-12.0	1.08e+1	7.80e-3	3.50e-3	-3.31e-4	1.21e-4
12.0-15.0	1.31e+1	9.51e-5	5.50e-3	-3.67e-4	5.03e-5
15.0-20.0	1.66e+1	8.62e-3	1.10e-2	-1.21e-3	7.32e-4

given in Table 4.3. The first column is the transverse momentum ( $p_T$ ), the second is the average value of transverse momentum, the third column is the double helicity asymmetry, the fourth is the statistical uncertainty, the fifth and the sixth columns are the lower and upper ranges of systematic uncertainty from the background fraction calculations. From this table, it is seen that the systematic uncertainties from the background fraction calculations are negligible compared to statistical uncertainties for all  $p_T$  ranges.

## 4.5 Summary

The systematic effects due to single spin asymmetry, relative luminosity and bunch-to-bunch spin effects are studied. Table 4.4 shows a summary of the dominant systematic uncertainties. These are dominated by the relative luminosity systematic uncertainty over the whole  $p_T$  range while the uncertainty due to single spin asymmetry is negligible. The global uncertainty due to polarization is  $\sim 6.5\%$  which also affect our results.

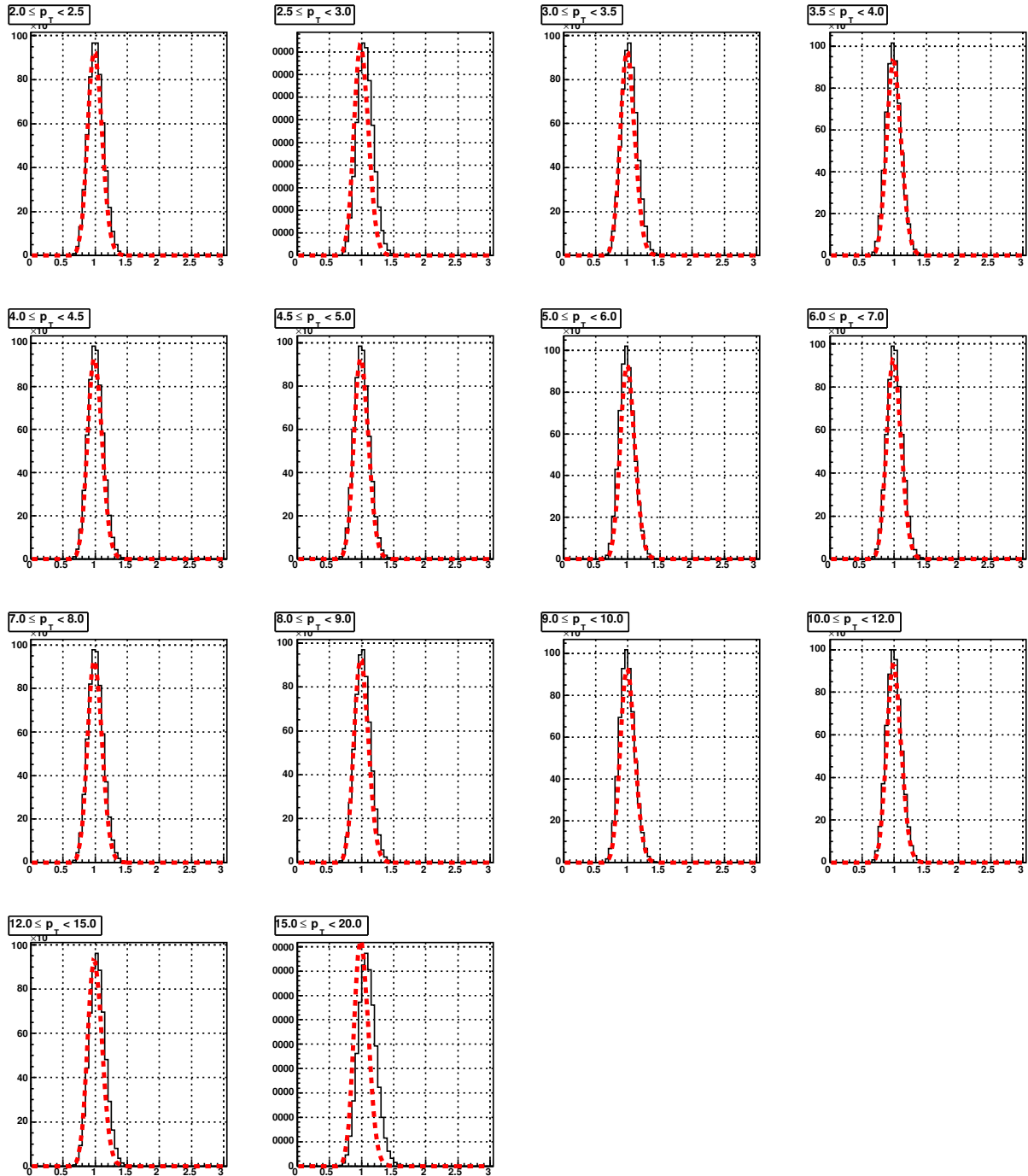


Figure (4.10)  $\chi^2/\text{NDF}$  from 600000 bunch shuffled samples from even bunches for  $A_{LL}^{\pi^0+BG}$ . The red dash curves are from the theoretical  $\chi^2$  fit.

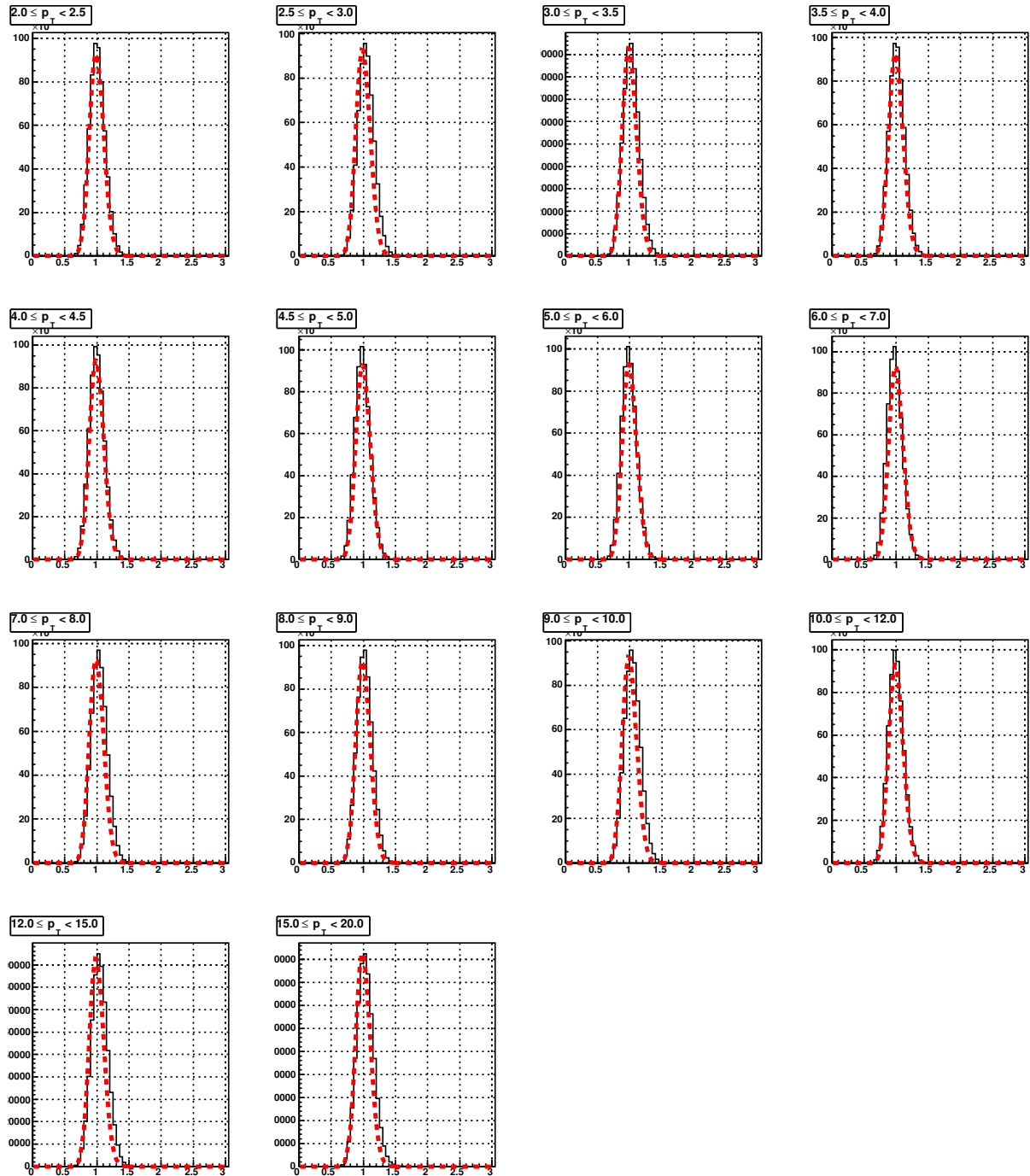


Figure (4.11)  $\chi^2/\text{NDF}$  results from 600000 bunch shuffled samples from odd bunches for  $A_{LL}^{\pi^0+BG}$ . The red dash curves are from the theoretical  $\chi^2$  fit.

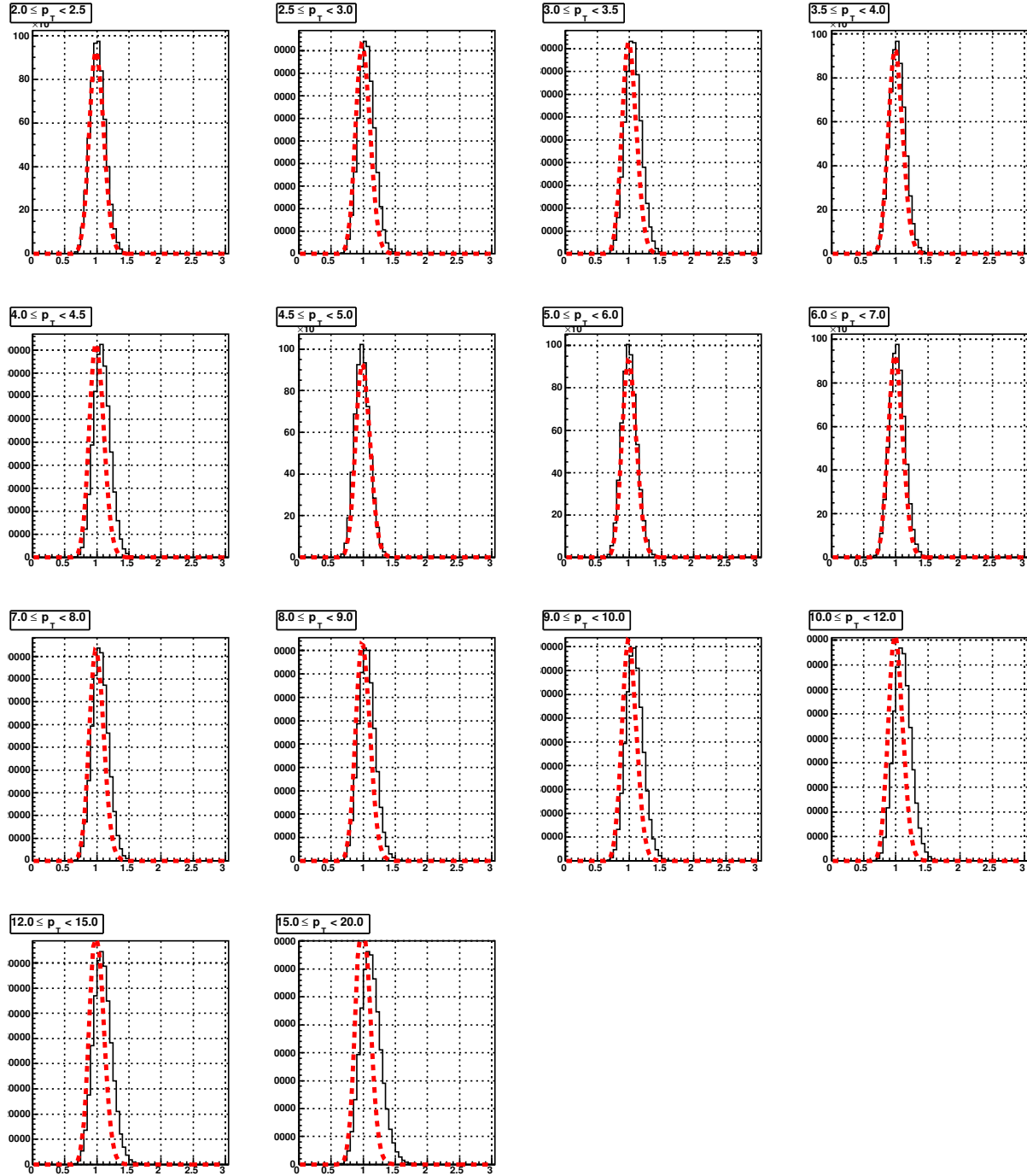


Figure (4.12)  $\chi^2/\text{NDF}$  results from 600000 bunch shuffled samples from even bunches for  $A_{LL}^{BG}$ . The red dash curves are the from the theoretical  $\chi^2$  fit.

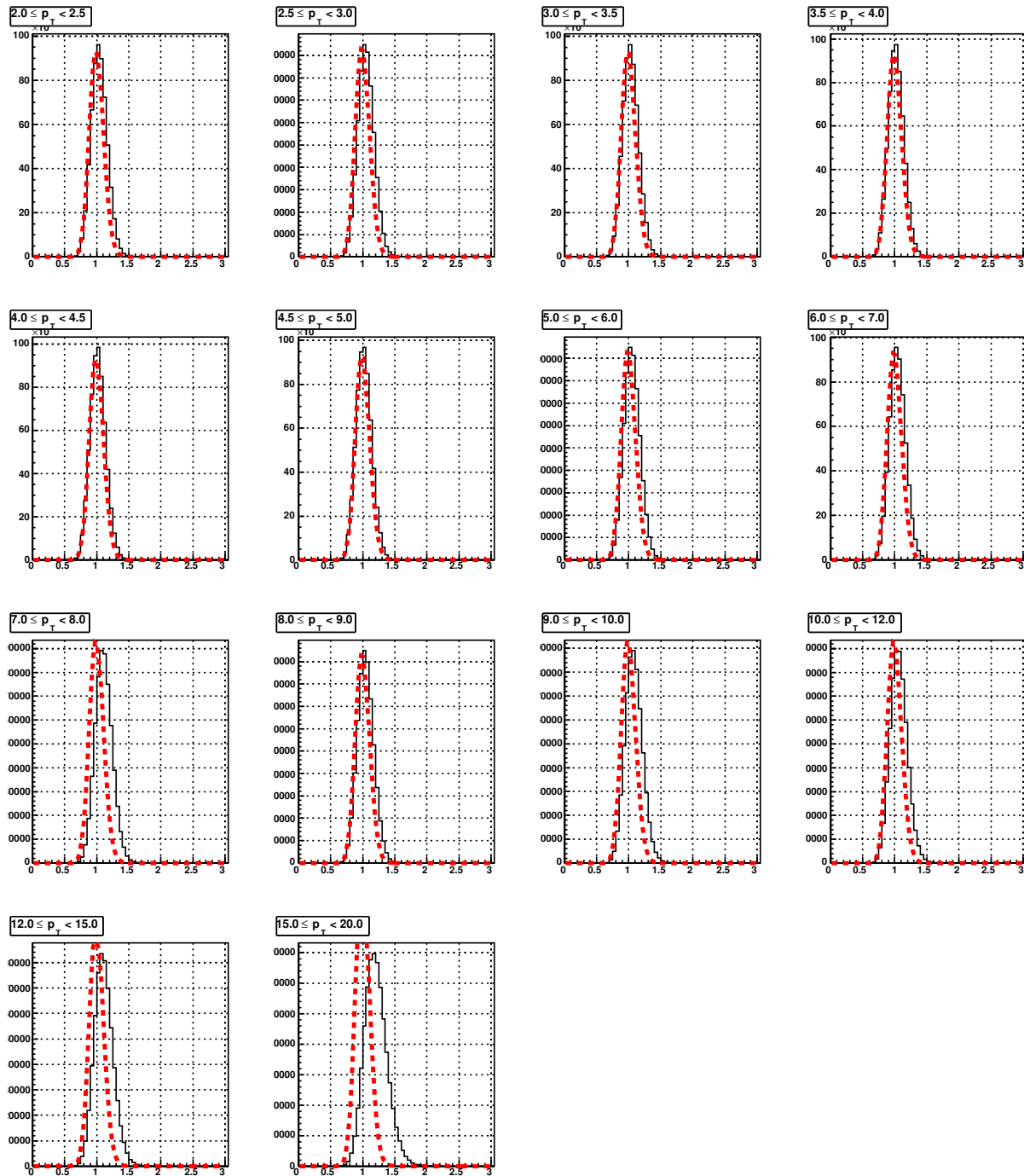


Figure (4.13)  $\chi^2/\text{NDF}$  results from 600000 bunch shuffled samples from odd bunches for  $A_{LL}^{BG}$ . The red dash curves are from the theoretical  $\chi^2$  fit.

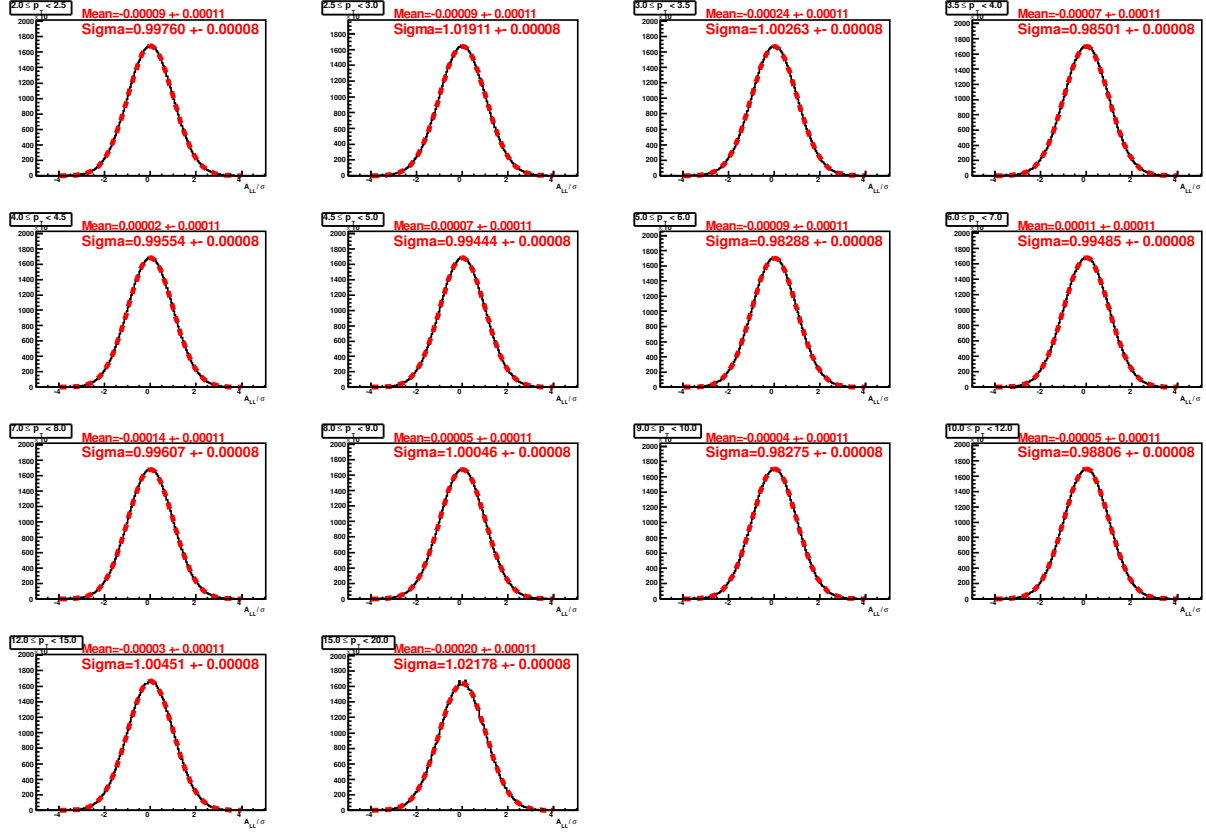


Figure (4.14) The distribution of  $A_{LL}^{\pi^0+BG}/\sigma$  for even bunches from the bunch shuffling. The red dash curves show Gaussian fit.

Table (4.4) Summary of non-negligible systematic uncertainties in the  $A_{LL}$  measurements is presented. The systematic uncertainty due to bunch shuffling with  $p_T$  below 12 GeV is negligible.

source	Effects
single spin asymmetry	$4.5 \pm 2.5 \times 10^{-4}$ (Blue), $-1.74 \pm 2.5 \times 10^{-4}$ (Yellow)
bunch shuffling ( $p_T > 12$ GeV)	< 1%
relative luminosity	$3.853 \times 10^{-4}$
polarization	6.5%

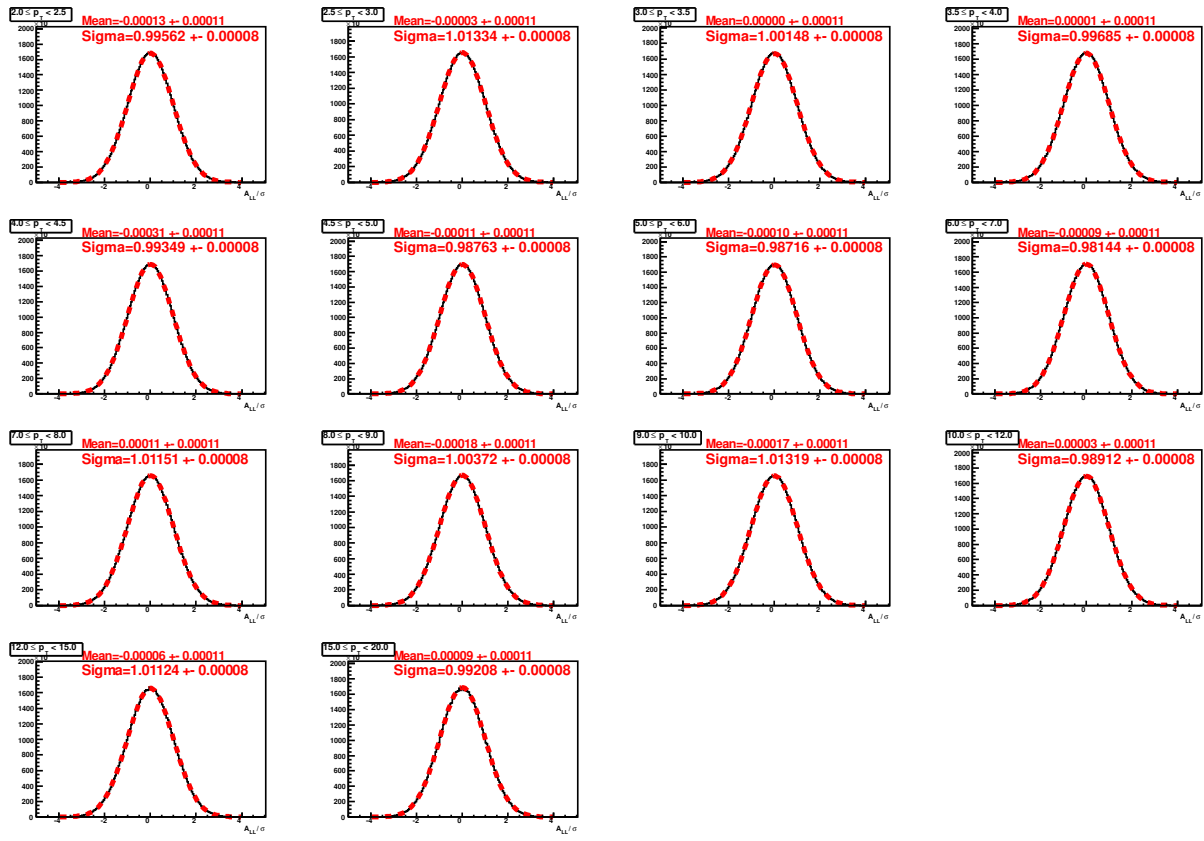


Figure (4.15) The distribution of  $A_{LL}^{\pi^0+BG}/\sigma$  for odd bunches from the bunch shuffling. The red dash curves show Gaussian fit.

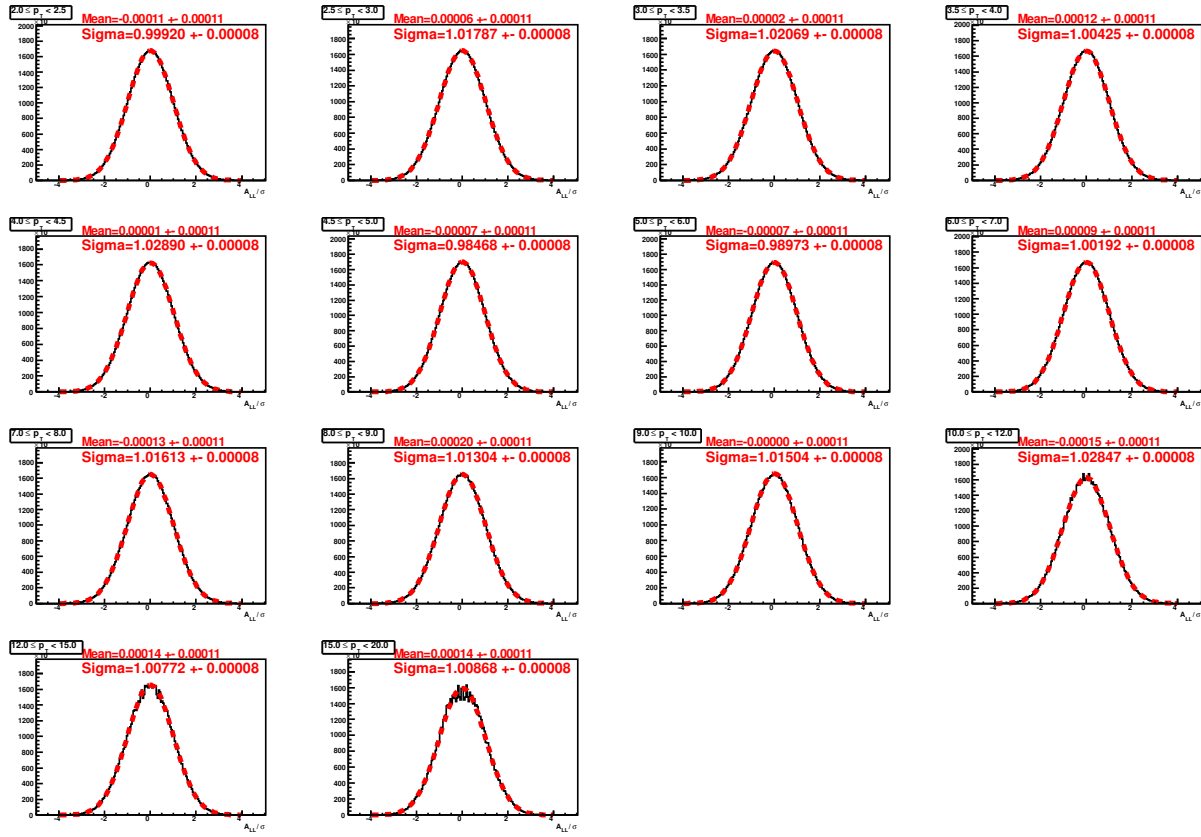


Figure (4.16) The distribution of  $A_{LL}^{BG}/\sigma$  for even bunches from the bunch shuffling. The red dash curves show Gaussian fit.

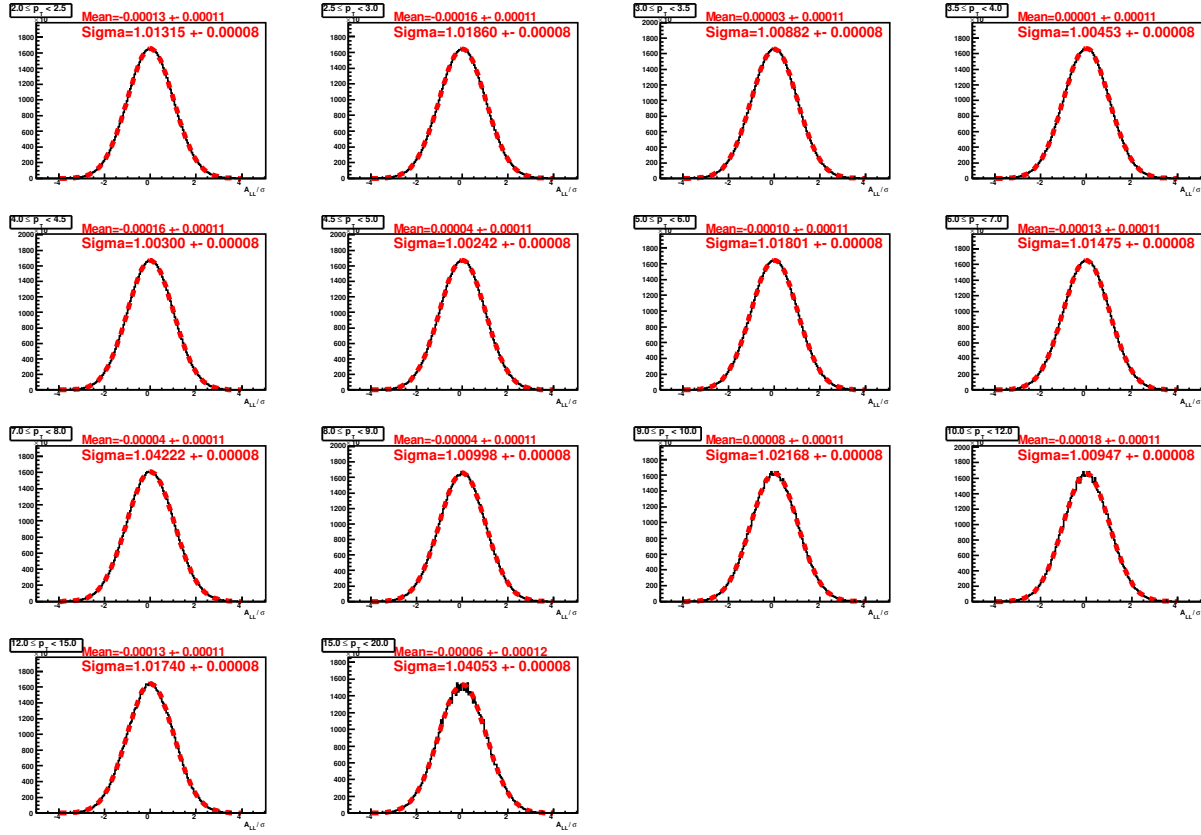


Figure (4.17) The distribution of  $A_{LL}^{BG}/\sigma$  for odd bunches from the bunch shuffling. The red dash curves show Gaussian fit.

## CHAPTER 5

### RESULTS AND DISCUSSION

The double helicity asymmetry in terms of particle yield, polarization and relative luminosity is calculated to the following Equation:

$$A_{LL} = \frac{\Delta\sigma}{\sigma} = \frac{1}{P_B P_Y} \frac{N^{++} - RN^{+-}}{N^{++} + RN^{+-}}, \quad R \equiv \frac{L^{++}}{L^{+-}} \quad (5.1)$$

where  $P_{B(Y)}$  is the polarization of the blue (yellow) beam,  $R$  is the relative luminosity and  $N^{++}(N^{+-})$  are the number of  $\pi^0$ 's obtained from the same sign (opposite sign) helicity collisions. There are three ingredients necessary to calculate  $A_{LL}$  as explained above. The first one is the beam polarization, second is the relative luminosity and the third is the  $\pi^0$  yield with same and opposite helicities, among which the first and the second are discussed in previous chapters. In this chapter, we focus on calculating  $A_{LL}$  and its statistical uncertainty ( $\sigma_{A_{LL}}$ ). RHIC carried out collisions with different spin patterns in order to reduce any systematic uncertainties from changing beam conditions. The asymmetries for the different spin patterns as a function of  $p_T$  are calculated. Finally, the double helicity asymmetry results obtained from the data collected in 2013 are discussed.  $A_{LL}$  results from 2013 is compared with those at 510 GeV from the data collected in 2012 and data collected in 2006 and 2009 [68]. The data are also compared with DSSV<sup>1</sup> calculation [70].

The  $\pi^0$  peak region in the invariant diphoton mass spectrum includes both  $\pi^0$  and background that can not be distinguished. Since the  $\pi^0$  mass window includes both  $\pi^0$  and background the calculated asymmetry will be diluted by the background. To extract the  $\pi^0$  asymmetry, the background asymmetry must be subtracted. The background asymmetry is independently calculated from shaded side bands as shown in Figure 3.3. This is based on

---

<sup>1</sup>RHIC data are combined with data from inclusive and semi inclusive DIS in a next-to-leading order (NLO) global QCD analysis, which is referred to as DSSV analysis.

the assumption that the background under the  $\pi^0$  peak is an extension to that on both sides of the  $\pi^0$  peak. To accurately subtract the background asymmetry, the background fraction under the  $\pi^0$  peak must be determined. The background fraction is calculated using the GPR method as detailed in Chapter 3.

## 5.1 Signal and Background Yield

In this section, the signal and background yields for different spin patterns are presented. As is stated in Chapter 2, there are eight spin patterns used for the data used in this analysis. They are grouped into four categories namely, SOOSSOO<sup>2</sup>, OSSOOSS, SSOO and OOSS. The invariant yield of  $\pi^0$  for these spin patterns for signal and background regions are shown in Tables 5.1 and 5.2. Finally, the cross-section as well as double helicity asymmetry results from run 13 are presented.

### 5.1.1 Spin Pattern Separated Yields and Background Fraction

$\pi^0$  yields for different spin patterns for even crossings are shown below:

Table (5.1) Di-photon yields and background fractions for even crossings for different spin patterns.

$p_T(GeV/c)$	Spin Pat.	Peak Yield	Back. Yield	Back. Frac. (%)
2.0-2.5	SOOSSOO	296431	133454	
	OSSOOSS	357018	159785	27.6
	SSOO	3561801	1795840	
	OOSS	3707908	1888111	
2.5-3.0	SOOSSOO	414846	147320	
	OSSOOSS	502605	176948	20.5

---

<sup>2</sup>S represents same helicity and O represents opposite helicity for blue and yellow beam. Similar scheme for other patterns also.

	SSOO	5546694	2115502	
	OOSS	5809845	2229894	
3.0-3.5	SOOSOO	447018	132899	
	OSOOS	539953	160380	16.5
	SSOO	6215045	1968842	
	OOSS	6544653	2086957	
3.5-4.0	SOOSOO	388404	102092	
	OSOOS	462936	121591	13.9
	SSOO	5659189	1579614	
	OOSS	5982479	1679693	
4.0-4.5	SOOSOO	301362	72856	
	OSOOS	356470	85530	12.5
	SSOO	4560569	1167810	
	OOSS	4842545	1241876	
4.5-5.0	SOOSOO	220049	50829	
	OSOOS	258047	58877	11.7
	SSOO	3429552	818916	
	OOSS	3637003	873264	
5.0-6.0	SOOSOO	268595	57276	
	OSOOS	312192	66378	11.2
	SSOO	4214987	927075	
	OOSS	4468989	981733	
6.0-7.0	SOOSOO	133421	25700	
	OSOOS	153476	29196	10.5
	SSOO	2097162	407445	
	OOSS	2208305	429549	
7.0-8.0	SOOSOO	66517	11586	
	OSOOS	76196	13272	9.7

	SSOO	1041814	182992		
	OOSS	1093378	190831		
8.0-9.0	SOOSOO	33694	5529	10.3	
	OSOOS	37978	6084		
	SSOO	522942	85532		
	OOSS	545742	89294		
9.0-10.0	SOOSOO	17936	2708	9.6	
	OSOOS	20167	3049		
	SSOO	273048	42258		
	OOSS	284529	44208		
10.0-12.0	SOOSOO	15383	2238	10.3	
	OSOOS	17282	2509		
	SSOO	234195	34620		
	OOSS	243792	35884		
12.0-15.0	SOOSOO	6291	866	10.4	
	OSOOS	7013	1000		
	SSOO	95870	13796		
	OOSS	100091	14480		
15.0-20.0	SOOSOO	1645	271	12.7	
	OSOOS	1865	322		
	SSOO	25539	4373		
	OOSS	26451	4638		

$\pi^0$  yields for different spin patterns for odd crossings are shown below:

Table (5.2) Di-photon yields and background fractions for odd crossings for different spin patterns.

$p_T(GeV/c)$	Spin Pat.	Peak Yield	Back. Yield	Back. Frac.(%)
2.0-2.5	SOOSOO	301911	133408	
	OSSOOSS	370996	163971	27.4
	SSOO	3442239	1738964	
	OOSS	3616037	1836657	
2.5-3.0	SOOSOO	411715	144410	
	OSSOOSS	505786	177585	20.6
	SSOO	5351868	2043877	
	OOSS	5637522	2164618	
3.0-3.5	SOOSOO	434889	128776	
	OSSOOSS	529470	157140	16.6
	SSOO	6003952	1902906	
	OOSS	6348560	2025332	
3.5-4.0	SOOSOO	373161	97903	
	OSSOOSS	448432	118101	14.0
	SSOO	5464919	1527769	
	OOSS	5799947	162045	
4.0-4.5	SOOSOO	288837	70142	
	OSSOOSS	344501	82581	12.5
	SSOO	4405739	1128086	
	OOSS	4690574	1201452	
4.5-5.0	SOOSOO	212388	48757	
	OSSOOSS	249511	56109	11.8
	SSOO	3312566	792768	
	OOSS	3525032	844286	

5.0-6.0	SOOSOO	258098	55250	
	OSOOSSS	300589	63308	10.6
	SSOO	4078000	895940	
	OOSS	4324431	951008	
6.0-7.0	SOOSOO	128446	24911	
	OSOOSSS	146662	28141	10.0
	SSOO	2024522	394326	
	OOSS	2137035	416102	
7.0-8.0	SOOSOO	64316	10937	
	OSOOSSS	73090	12578	10.3
	SSOO	1009074	176731	
	OOSS	1054626	184662	
8.0-9.0	SOOSOO	32384	5353	
	OSOOSSS	36725	5845	8.9
	SSOO	506375	83229	
	OOSS	526337	86903	
9.0-10.0	SOOSOO	17058	2622	
	OSOOSSS	19158	3028	10.4
	SSOO	264092	41119	
	OOSS	275975	43096	
10.0-12.0	SOOSOO	14739	2035	
	OSOOSSS	16808	2416	9.4
	SSOO	226323	33696	
	OOSS	235332	35158	
12.0-15.0	SOOSOO	6035	839	
	OSOOSSS	6778	1035	10.3
	SSOO	91991	13512	

	OOSS	96361	13838	
15.0-20.0	SOOSOO	1577	262	
	OSOOSS	1849	335	11.3
	SSOO	24749	4276	
	OOSS	25666	4330	

The background corrected asymmetry and corresponding statistical uncertainty of  $\pi^0$  are calculated using Equations 5.2 and 5.3.

$$A_{LL}^{\pi^0} = \frac{A_{LL}^{\pi^0+BG} - r A_{LL}^{BG}}{1 - r} \quad (5.2)$$

$$\sigma_{A_{LL}^{\pi^0}} = \frac{\sqrt{\sigma_{A_{LL}^{\pi^0+BG}}^2 + r^2 \sigma_{A_{LL}^{BG}}^2}}{1 - r}, \quad (5.3)$$

where  $r = \frac{N_{BG}}{N_{\pi^0+BG}}$  is the background fraction. The number of particles within background region is calculated by fitting the background region using the GPR method and counting the particle within the fit.

$A_{LL}^{\pi^0}$  is calculated over the  $p_T$  range,  $2 \leq p_T \leq 20$  GeV/c. Below 2 GeV/c, the mass spectrum is dominated by background and above 20 GeV/c<sup>2</sup> the  $\pi^0$  yield is limited statistically. Due to different ERT electronics chains, the data are analyzed separately for even and odd bunch crossings. The final  $A_{LL}$  is the weighted average of those of even and odd bunch crossing.

$$A_{LL} = \frac{\frac{A_{LL}^{even}}{(\delta A_{LL}^{even})^2} + \frac{A_{LL}^{odd}}{(\delta A_{LL}^{odd})^2}}{\frac{1}{(\delta A_{LL}^{even})^2} + \frac{1}{(\delta A_{LL}^{odd})^2}}. \quad (5.4)$$

while the uncertainty is:

$$\delta A_{LL} = \sqrt{\frac{1}{\frac{1}{(\delta A_{LL}^{even})^2} + \frac{1}{(\delta A_{LL}^{odd})^2}}}. \quad (5.5)$$

The statistical uncertainties in the Equation 5.3,  $\sigma_{N_{\gamma\gamma}}$  are not simply  $\sqrt{N_{\gamma\gamma}}$ . There may be more than one photon pair per event in the selected mass region, which causes a slight

increase in the uncertainty,

$$\sigma_{N_{\gamma\gamma}} = \sqrt{\frac{\bar{\kappa}^2}{\kappa} N_{\gamma\gamma}} \quad (5.6)$$

where  $\kappa$  is the multiplicity of the collisions and  $\bar{\kappa}$  is the average of the multiplicity of the collisions. The values of  $\frac{\bar{\kappa}^2}{\kappa} N_{\gamma\gamma}$  for different  $p_T$  bins used in this analysis are shown in Table 5.3.

The  $p_T$  distribution may differ between signal and background region so the  $\pi^0$   $p_T$  is

Table (5.3)  $\kappa$ -factors for the  $\pi^0 + BG$  and BG region.

$p_T(GeV/c)$	$\kappa^{\pi^0+BG}$ (Even)	$\kappa^{BG}$ (Even)	$\kappa^{\pi^0+BG}$ (Odd)	$\kappa^{BG}$ (Odd)
2-2.5	1.0591	1.1266	1.0592	1.1222
2.5-3	1.0438	1.1077	1.0440	1.1066
3-3.5	1.0358	1.0975	1.0353	1.0979
3.5-4	1.0303	1.0908	1.0303	1.0892
4-4.5	1.0265	1.0830	1.0259	1.0845
4.5-5	1.0222	1.0775	1.0221	1.0771
5-6	1.0325	1.1148	1.0325	1.1130
6-7	1.0247	1.1007	1.0249	1.1013
7-8	1.0217	1.0925	1.0205	1.0879
8-9	1.0176	1.0790	1.0172	1.0798
9-10	1.0157	1.0757	1.0162	1.0754
10-12	1.0227	1.0965	1.0265	1.1065
12-15	1.0297	1.1243	1.0263	1.1014
15-20	1.0318	1.1108	1.0301	1.0947

determined according to Equation 5.7

$$\langle p_T^{\pi^0} \rangle = \frac{\langle p_T^{\pi^0+BG} \rangle - r \langle p_T^{BG} \rangle}{1 - r} \quad (5.7)$$

where  $r$  is the background fraction from Table 5.5. The average value of  $p_T$  is given in Table 5.4.

Table (5.4) Mean  $p_T$  for each  $p_T$  bin.

$p_T$ (GeV/c)	Average $p_T$ ( $\langle p_T \rangle$ ) (GeV/c)
2.0-2.5	2.2801
2.5-3.0	2.7627
3.0-3.5	3.2507
3.5-4.0	3.7440
4.0-4.5	4.2401
4.5-5.0	4.7378
5.0-6.0	5.4460
6.0-7.0	6.4454
7.0-8.0	7.4454
8.0-9.0	8.4471
9.0-10.0	9.4512
10.0-12.0	10.824
12.0-15.0	13.140
15.0-20.0	16.627

## 5.2 Results and Discussion

### 5.2.1 Cross-Section

The invariant differential cross-section for  $\pi^0$  production is calculated according to the following Equation:

$$E \frac{d^3\sigma}{dp^3} = \frac{1}{\mathcal{L}} \frac{1}{2\pi p_T^*} \frac{C.N}{\Delta p_T \Delta y}, \quad (5.8)$$

where N is the number of  $\pi^0$ 's observed in a  $\Delta p_T$  wide bin at  $p_T^*$  defined as the  $p_T$  for which the cross-section equals its average over the bin;  $\Delta y$  is the rapidity range; C includes corrections for trigger efficiency, geometrical acceptance,  $\pi^0$  reconstruction efficiency, and detector resolution effects;  $\mathcal{L}$  is the integrated luminosity for the analyzed data sample.

Figure 5.1 shows the  $\pi^0$  cross-section versus  $p_T$  compared to NLO pQCD calculations performed with MSTW [75] parton distribution functions (PDF) and DSS14 [70] fragmentation functions (FF). Compared to earlier FF analysis [76], the DSS14 recent global fit results preferred a smaller fraction of pions produced from gluon hadronization, driven mainly by the latest LHC data. The theoretical calculation agrees with the presented data very well.

Table (5.5) Background fraction,  $r$ , in the  $\pi^0 + BG$  region for even and odd bunch

$p_T(\text{GeV}/c)$	Even	Odd
2.0-2.5	0.32	0.32
2.5 - 3.0	0.21	0.21
3.0 - 3.5	0.16	0.16
3.5 - 4.0	0.13	0.13
4.0 - 4.5	0.12	0.12
4.5 - 5.0	0.11	0.11
5.0 - 6.0	0.13	0.13
6.0 - 7.0	0.12	0.12
7.0 - 8.0	0.11	0.11
8.0 - 9.0	0.11	0.11
9.0 - 10.0	0.11	0.11
10.0 - 12.0	0.10	0.10
12.0 - 15.0	0.10	0.10
15.0 - 20.0	0.12	0.13

Due to this agreement between the data and the theory, the theory can be used to interpret the  $A_{LL}$  results.

### 5.2.2 Double Helicity Asymmetry ( $A_{LL}$ ) Results

Figure 5.2 shows the final double helicity asymmetry from the year 2013 at  $\sqrt{s} = 510$  GeV. Results from the year 2013 are combined with those from the year 2012 to enhance statistical accuracy. Figure 5.3 shows the  $\pi^0 A_{LL}$  asymmetries at  $\sqrt{s} = 510$  GeV from years 2012 and 2013 data combined and is compared with the DSSV14 calculation [70] based on a global fit of the world helicity asymmetry data including  $\pi^0 A_{LL}$  results at  $\sqrt{s} = 62$  and 200 GeV from PHENIX [68] and jet  $A_{LL}$  results at  $\sqrt{s} = 200$  GeV from STAR [69]. Comparing the data to the DSSV14 curve we obtain  $\chi^2/\text{NDF} = 8.0/14$ , while comparing to the  $A_{LL} = 0$  assumption we obtain  $\chi^2/\text{NDF} = 18.2/14$ ; the data prefer the DSSV14 curve by a little more than 3 standard deviations.

Figure 5.4 shows  $\pi^0 A_{LL}$  data from PHENIX at both  $\sqrt{s} = 200$  GeV [68] and 510 GeV, along with NLO pQCD analyses from three groups [71, 72, 70]. All three analyses predict

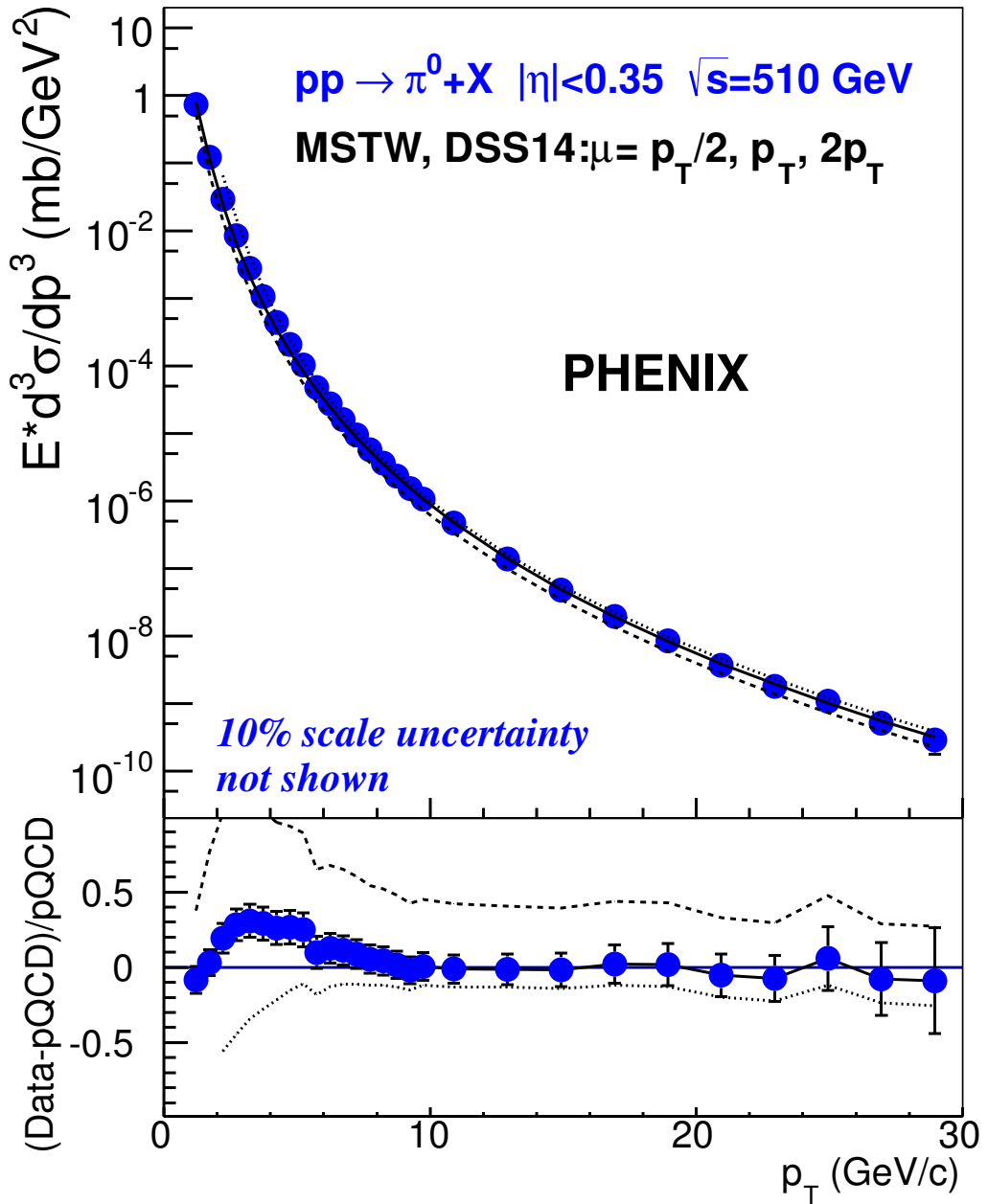


Figure (5.1) (color online). The neutral pion production cross section at  $\sqrt{s} = 510$  GeV as a function of  $p_T$  and the results of NLO pQCD calculations for theory scales  $\mu = p_T/2$  (dotted line),  $p_T$  (solid line) and  $2p_T$  (dashed line), with  $\mu$  representing equal factorization, renormalization, and fragmentation scales. Note that the error bars, representing the combined statistical and point-to-point systematic uncertainties, are smaller than the points. The bottom panel shows the relative difference between the data and theory for the three theory scales. Experimental uncertainties are shown for the  $\mu = p_T$  curve.

an increase in  $\pi^0 A_{LL}$  due to pQCD evolution. However, the asymmetries at  $\sqrt{s} = 510$  GeV are systematically above the 200 GeV data points in the overlapping  $x_T$  range, with  $x_T = 2p_T / \sqrt{s}$ . Also, Figure 5.4 shows  $A_{LL}$  as the function of  $p_T$ . From this Figure, it can be

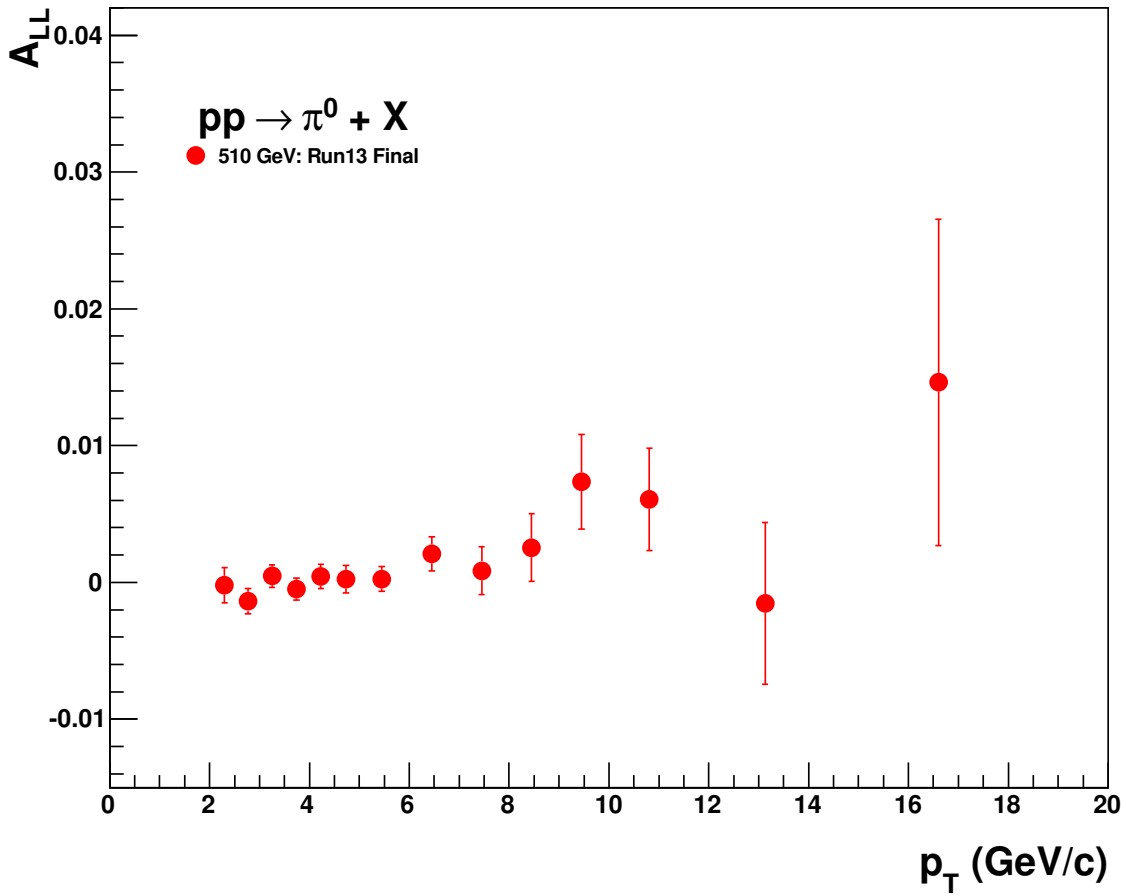


Figure (5.2)  $A_{LL}$  vs  $p_T$  for  $\pi^0$  production at mid-rapidity at  $\sqrt{s} = 510$  GeV from run 13.

seen that there is a non-zero asymmetry beyond the previous results [68]. Table 5.6 gives the double helicity asymmetry values at  $\sqrt{s} = 510$  GeV. The first and second columns are the covered  $p_T$  range and average  $p_T$ , the third and fourth columns are the double helicity asymmetries and the corresponding statistical uncertainties.

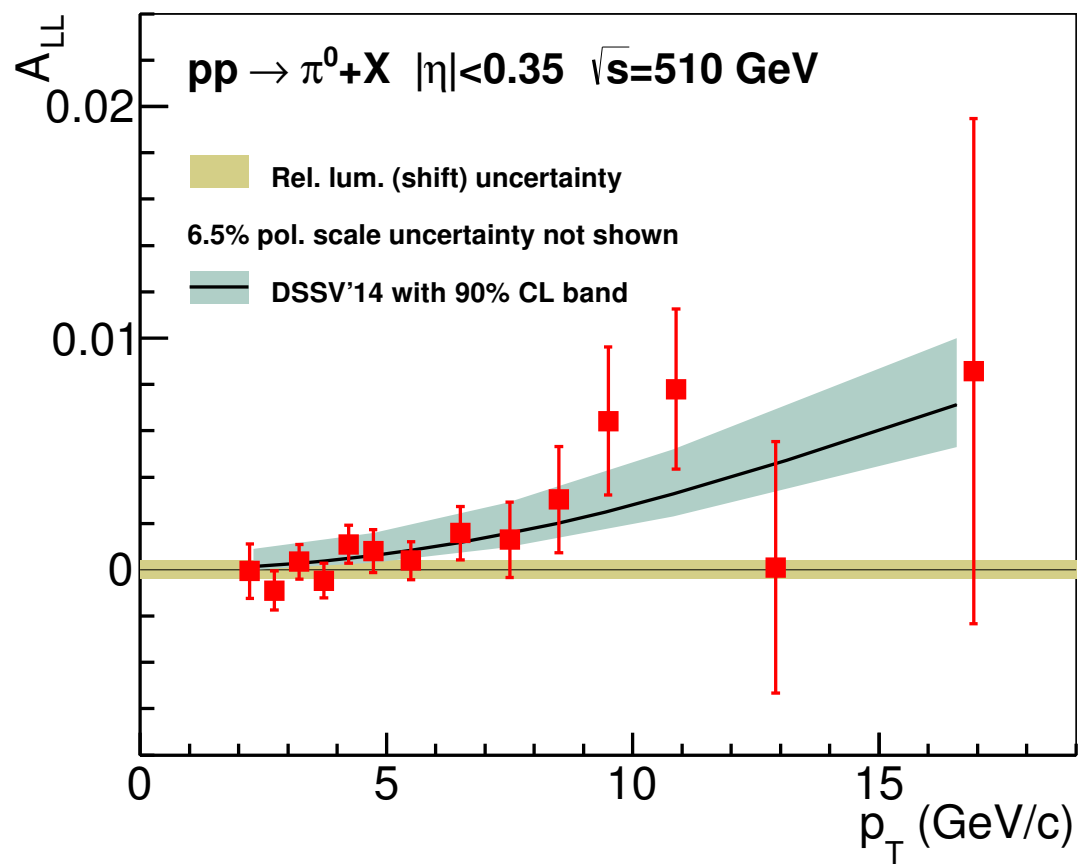


Figure (5.3)  $A_{LL}$  vs  $p_T$  for  $\pi^0$  production at mid-rapidity at  $\sqrt{s} = 510$  GeV. Shift uncertainty from relative luminosity is shown at  $A_{LL} = 0$ . Theoretical curve with 90% C.L. band is DSSV14 calculation [70].

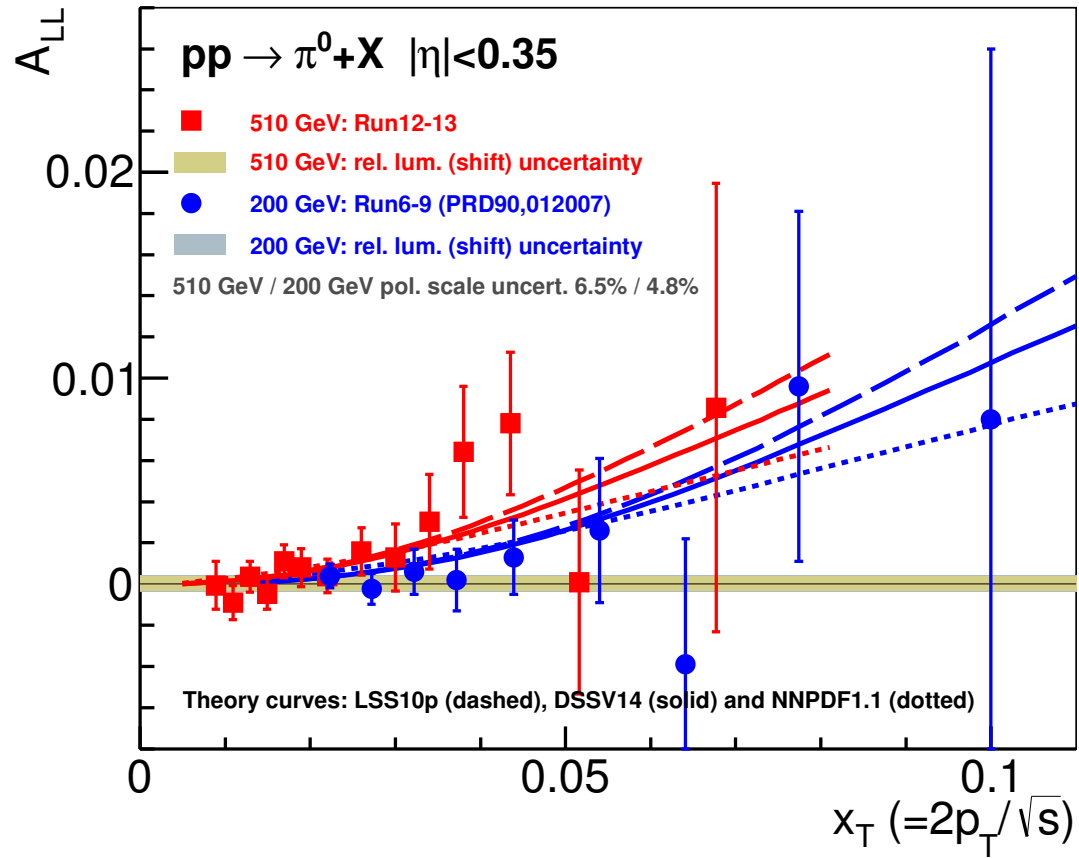


Figure (5.4)  $A_{LL}$  vs  $x_T$  for  $\pi^0$  production at mid-rapidity at  $\sqrt{s} = 200$  GeV from [68] and  $\sqrt{s} = 510$  GeV from this analysis. Note that the shift uncertainties from two data samples are about the same, hence indistinguishable in this plot. Theoretical curves are from recent NLO global analyses [64, 59, 70].

Table (5.6)  $A_{LL}^{\pi^0}$  at  $\sqrt{s} = 510$  GeV

$p_T$ (GeV/c)	Mean $P_T$ (GeV/c)	$A_{LL}^{\pi^0}$	$\Delta A_{LL}^{\pi^0}$
2.0-2.5	2.2801	$-2.2138 \times 10^{-4}$	$1.2918 \times 10^{-3}$
2.5-3.0	2.7627	$-1.3901 \times 10^{-3}$	$9.2251 \times 10^{-4}$
3.0-3.5	3.2507	$4.6369 \times 10^{-4}$	$8.1329 \times 10^{-4}$
3.5-4.0	3.7440	$-4.8270 \times 10^{-4}$	$8.1390 \times 10^{-4}$
4.0-4.5	4.2401	$4.4910 \times 10^{-4}$	$8.8162 \times 10^{-4}$
4.5-5.0	4.7378	$2.2152 \times 10^{-4}$	$1.0026 \times 10^{-3}$
5.0-6.0	5.4460	$2.5139 \times 10^{-4}$	$8.9455 \times 10^{-4}$
6.0-7.0	6.4454	$2.0970 \times 10^{-3}$	$1.2523 \times 10^{-3}$
7.0-8.0	7.4454	$8.5907 \times 10^{-4}$	$1.7673 \times 10^{-3}$
8.0-9.0	8.4471	$2.5418 \times 10^{-3}$	$2.4795 \times 10^{-3}$
9.0-10.0	9.4512	$7.3621 \times 10^{-3}$	$3.4539 \times 10^{-3}$
10.0-12.0	10.824	$6.0844 \times 10^{-3}$	$3.7467 \times 10^{-3}$
12.0-15.0	13.140	$-1.5295 \times 10^{-3}$	$5.9230 \times 10^{-3}$
15.0-20.0	16.627	$1.4624 \times 10^{-2}$	$1.1918 \times 10^{-2}$

## CHAPTER 6

### SUMMARY AND CONCLUSION

The double helicity asymmetry in  $\pi^0$  production in polarized proton-proton collisions at  $\sqrt{s} = 510$  GeV has been measured. The result is compared with similar measurements at  $\sqrt{s} = 200$  GeV. The systematic uncertainties were dominated by the uncertainty due to the relative luminosity at  $\sim 3.9 \times 10^{-4}$ . The result is also compared with the results obtained from DSSV global analysis. This results is especially important since it pushes the kinematic coverage down to  $x \sim 0.01$  and it is expected to provide better constrains on  $\Delta g(x)$  once included in a global analysis of the world data such as DSSV.

Previous PHENIX data at 200 GeV [68] were included in the DSSV global analysis [70] and significantly constrained  $\Delta g(x)$ . The gluon helicity distribution  $\Delta g(x, Q^2)$  at  $Q^2 = 10$  GeV<sup>2</sup> from new DSSV fit using  $\sqrt{s} = 200$  GeV data is shown in Figure 6.1 [70]. The solid line represents the central fit result while the dotted lines corresponds to additional fits that are within the 90% confidence level (C.L.) interval. Figure 6.2 shows the variation of the total  $\chi^2$  of the fit as a function of the truncated first moment in the RHIC  $x$ -range,  $\int_{0.05}^{0.2} dx \Delta g(x, Q^2)$ , for various values of  $Q^2$ . A similar analysis, although not as detailed, that included the 510 GeV results was carried out [77]. The  $\Delta\chi^2$  profile results obtained from this quick analysis compared with the DSSV14 [70] is shown in Figure 6.3. The minimum of  $\chi^2$  corresponds to the best fit value of  $\Delta G$ . The width corresponds to its uncertainty. The 510 GeV data provides better constrains on  $\Delta g(x)$  as the width becomes narrower which can be seen in Figure 6.3.

In summary, we presented recent PHENIX measurement of  $A_{LL}$  in  $\pi^0$  production in longitudinally polarized  $p + p$  collisions at  $\sqrt{s} = 510$  GeV based on the data collected in

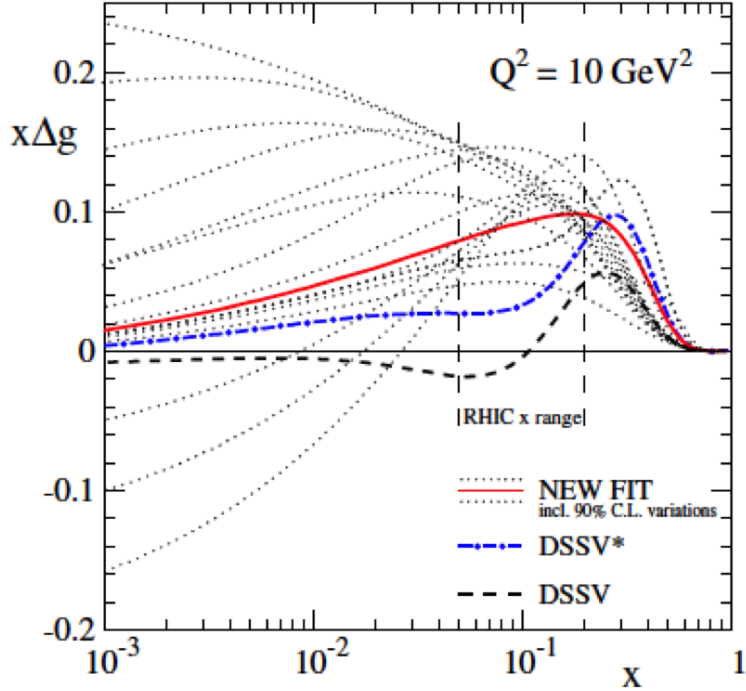


Figure (6.1) Gluon helicity distribution at  $Q^2 = 10 \text{ GeV}^2$ . The dotted lines represent the gluon densities for alternative fits that are within the 90% C.L. limit [70].

2013. A non-zero asymmetry is observed indicating a non-zero gluon contribution to the spin of the proton in the accessed kinematic range.

## 6.1 Outlook

The new polarized Electron Ion Collider (EIC) is currently under review. The EIC is expected to cover a large range in  $x$ , reaching a minimum  $x$  of  $10^{-4}$ . Such a collider will not only map the polarized gluon distribution but also offer insights into the orbital angular momentum (OAM) of quarks and gluons. Orbital angular momentum depends on the correlation between positions and momenta of the quarks and gluons. The EIC will provide three-dimensional images of the sea quark and gluon distributions which will provide insights into the overall spin structure of proton. The EIC machine design specifications are aimed at achieving higher polarization ( $\sim 70\%$ ) of electron and nucleon beams and high

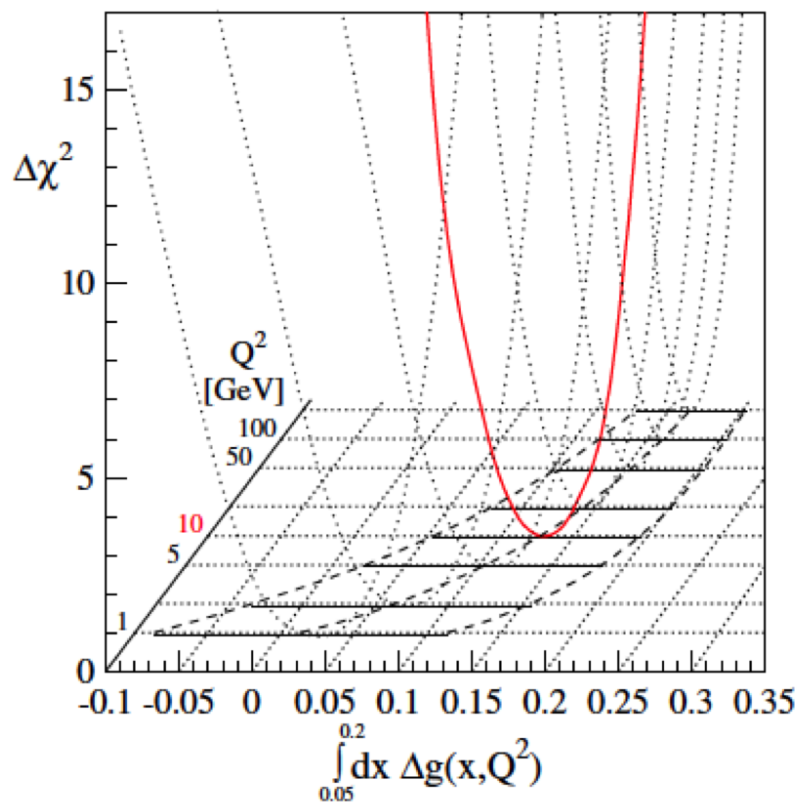


Figure (6.2) Change of the  $\Delta\chi^2$  profile of the truncated first moment of  $\Delta g$  in the  $x$ -range with  $Q^2$ . The solid lines at the base of the plot indicate the 90% C.L. interval [70].

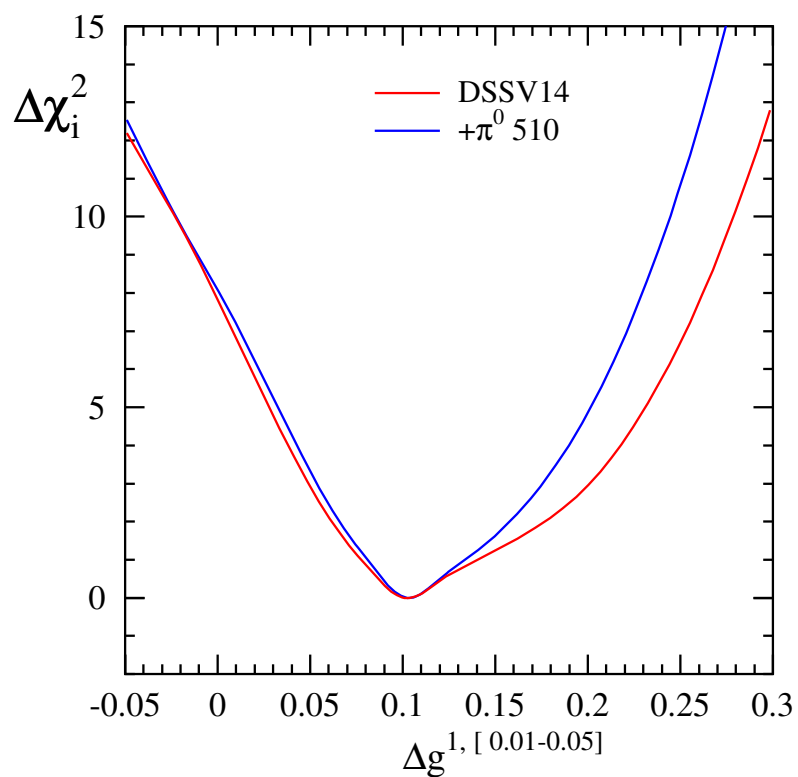


Figure (6.3) Variation of total  $\chi^2$  of the fit as a function of the truncated first moment of  $\Delta g$  in the  $x$ -range  $\sim [0.01 - 0.05]$ . The results obtained from  $\sqrt{s} = 510$  GeV is compared with the DSSV14 results [70]. This calculation is from [77].

detector capabilities. This will allow achieving a precision far beyond that of any other existing facilities in the world. It can collide ion beams from light nuclei like deuteron to the heaviest nuclei (uranium or lead). In addition, it provides high collision luminosity  $\sim 10^{33-34}$   $\text{cm}^{-2}\text{s}^{-1}$ . The projected correlated truncated integrals of  $\Delta\Sigma$  and  $\Delta g$  over  $0.001 \leq x \leq 1$  are shown in Figure 6.4. The light shaded area displays the present accuracies of the integrals of  $\Delta\Sigma$  and  $\Delta g$  over  $0.001 \leq x \leq 1$ , along with their correlations. The expected improvement on the precision of the measurement obtained from the EIC based on global analysis projections is represented by the inner areas in Figure 6.4. This results clearly highlight the power of the EIC in mapping out nucleon helicity structure.

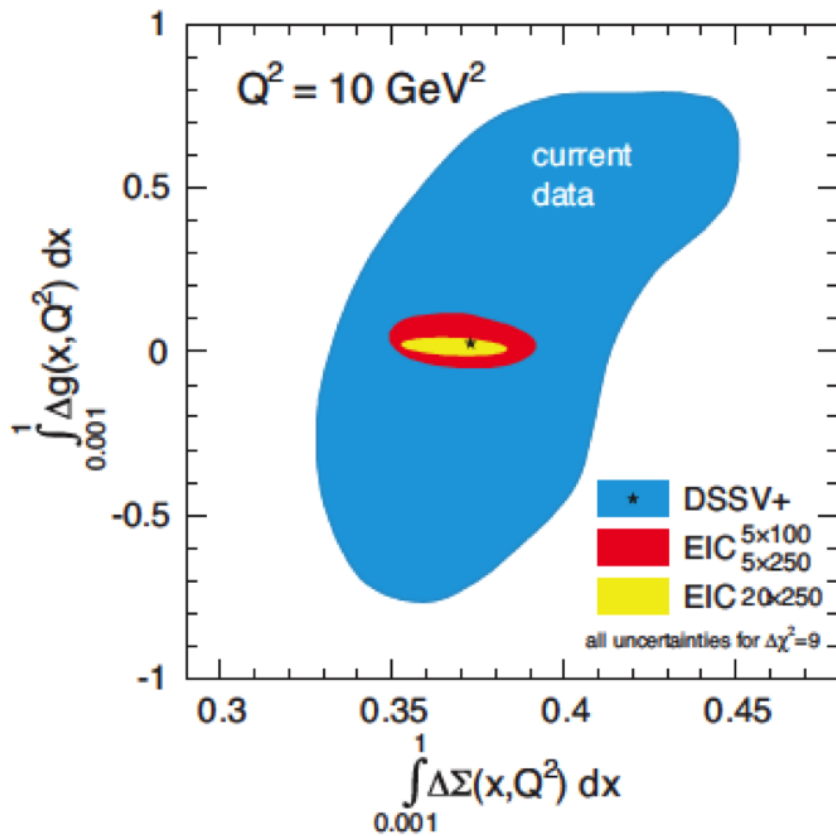


Figure (6.4) Accuracies for the correlated truncated integrals of  $\Delta\Sigma$  and  $\Delta g$  over  $0.001 \leq x \leq 1$ , on the basis of the DSSV+ analysis (outer area) and projected for an EIC (inner areas) [78].

## Bibliography

- [1] T. Y. Cao, *From Current Algebra to Quantum Chromodynamics*, Cambridge University Press (2010).
- [2] D. H. Perkins, *Introduction to High Energy Physics*, Addison-wesley publishing company (1971).
- [3] V. E. Barnes *et al.* Phys. Rev. Lett. **12**, 204 (1964).
- [4] R. E . Taylor, Rev . Mod . Phys. **63**, 573 (1991).
- [5] H. W. Kendall, Rev. Mod. Phys. **63**, 597 (1991).
- [6] J. I. Friedman, Rev. Mod. Phys. **63**, 615 (1991).
- [7] M. J. Alguard t, J. E. Clendenin, R. D. Ehrlich, V. W. Hughes, J. S. Ladish and Lubell. Nucl. Instrum. Meth. **163**, 29 - 59 (1979).
- [8] M. J. Alguard *et al.*, Phys. Rev. Lett. **37**, 1261 (1976).
- [9] J. Asman *et al.* (European Muon Collaboration), Phys. Lett. B **206**, 364 (1988).
- [10] N. F. Mott and H. S. W. Massey, *The Theory of Atomic Collisions*, Oxford University Press (1965).
- [11] K. Abe *et al.* (E154 Collaboration), Phys. Rev. Lett. **76**, 587 (1996).
- [12] A. Airapetian *et al.* (HERMES Collaboration), Phys. Rev. D **75**, 012007 (2007).
- [13] V. Yu. Alexakhin *et al.* (COMPASS Collaboration), Phys. Lett. B **647**, 8 (2007).
- [14] B. Adeva *et al.* (SMC Collaboration), Phys. Rev. D **58**, 112002 (1998).
- [15] G. Bunce, N. Saito, J. Soffer, and W. Vogelsang, Ann. Rev. Nucl. Part. Sci. **50**, 525 (2000).

- [16] J. Blümlein and H. Böttcher, Nucl. Phys. B **841**, 205 (2010).
- [17] I. Alekseev *et al.*, Nucl. Instr. Meth. A **499**, 392 (2003).
- [18] J. I. Friedman and H. W. Kendall , Ann. Rev. Nucl. Sci. **22** , 203 (1972); R. E. Taylor, Rev. Mod. Phys. **63**, 573 (1991); H. Kendall, Rev. Mod. Phys. **63** , 597 (1991); J. I. Friedman, Rev. Mod. Phys. **63**, 615 (1991).
- [19] B. R. Martin, *Nuclear and Particle Physics - An introduction*, John Wiley & Sons (2006).
- [20] S. D. Bass, *The Spin Structure of the Proton*, World Scientific (2008).
- [21] V. G. Soloviev, *Theory of atomic nuclei: Quasiparticles and phonons*, CRC Press (1992).
- [22] J. Ellis and M. Karliner, Phys. Lett. B **313**, 131 (1993).
- [23] R. L. Jaffe, Phys. Today **48** (9), 24 (1995).
- [24] J. D. Bjorken, Phys. Rev. **148**, 1467 (1966).
- [25] I. Alekseev *et al.*, Configuration Manual Polarized Proton Collider at RHIC, 2006
- [26] A. Kponou, A. Zelenski, S. Kokhanovski and V. Zubets, AIP Conf. Proc. **980**, 241 (2008).
- [27] V. I. Ptitsin and Yu. M. Shatunov, Proc. Third Workshop on Siberian Snakes and Spin Rotators (A. Luccio and Th. Roser Eds.) Upton, NY, Sept. 12-13, 1994, Brookhaven National Laboratory Report BNL-52453.
- [28] V. Bargmann, L. Michel and V. L. Telegdi, Phys. Rev. Lett. **2**, 435 (1959).
- [29] S. R. Mane, Yu. M. Shatunov and K. Yokoya, Journal of Physics G. **31**, R151 (2005).
- [30] M. Allen *et al.*, Nucl. Instrum. Meth. A **499**, 549 (2003).
- [31] L. Aphecetche *et al.*, Nucl. Instrum. Meth. A **499**, 521 (2003).

- [32] C. Adler *et al.*, Nucl. Instr. And Meth. A **470**, 488 (2000).
- [33] K. Adcox *et al.*, Nucl. Instr. Meth. A **497**, 2003.
- [34] F. E. Close and R. G. Roberts, Phys. Lett. B **316**, 165 (1993).
- [35] J. Ashman *et al.*, Nucl. Phys. B **328**, 1 (1989).
- [36] K. A. Olive *et al.*, (Particle Data Group), Chin. Phys. C, **38**, 010009 (2014).
- [37] M. Anselmino, arXiv:hep-ph/0302006.
- [38] K. Adcox *et al.*, Nucl. Instrum. Methods Phys. Res., Sect. A **499**, 469 (2003).
- [39] S. S. Adler *et al.* (PHENIX Collaboration), Phys. Rev. Lett. **91**, 241803 (2003).
- [40] Derbenev and A. M. Kondratenko, Sov. Phys. JETP **37**, 968 (1973).
- [41] Adler *et al.*, Phys. Rev. D **73**, 091102 (2006).
- [42] B. I. Abelev *et al.* (STAR Collaboration), Phys. Rev. Lett. **97**, 252001 (2006).
- [43] S. S. Adler *et al.* (PHENIX Collaboration), Phys. Rev. Lett. **98**, 012002 (2007).
- [44] P. Amaudruz *et al.*, Phys. Rev. Lett. **66**, 2712 (1991); A. Baldit *et al.*, Phys. Lett. **332**, 244 (1994); E. A. Hawker *et al.*, Phys. Rev. Lett. **80**, 3715 (1998); K. Ackerstaff *et al.*, Phys. Rev. Lett. **25**, 5519 (1998).
- [45] K. V. Dharmawardane *et al.*, Phys. Lett. B **641**, 11 (2006).
- [46] T. Gehrmann and W.J. Stirling, Phys. Rev. D **53**, 6100 (1996).
- [47] M. Gluck, E. Reya, M. Stratmann and W. Vogelsang, Phys. Rev. D **63**, 094005 (2001).
- [48] E. Leader, A. V. Sidorov, D. B. Stamenov, Phys. Rev. D **80**, 054026 (2009).
- [49] Y. Goto *et al.* (Asymmetry Analysis Collaboration), Phys. Rev. D **62**, 034017 (2000).
- [50] E. Leader, A. V. Sidorov and D. B. Stamenov, Phys. Rev. D **73**, 034023 (2006).

- [51] R. L. Jaffee and A. Manohar, Nucl. Phys. B **337**, 509 - 546 (1990).
- [52] M. Stratmann and W. Vogelsang, J. Phys. Conf. Ser., 012035, (2007).
- [53] D. de Florian, G. A. Navarro and R. Sassot, Phys. Rev. D **71**, 094018 (2005).
- [54] A. Airapetian *et al.*, Phys. Rev. D **75**, 012007 (2007).
- [55] B. I. Abelev *et al.* (STAR Collaboration), Phys. Rev. Lett. **97**, 252001 (2006).
- [56] S. S. Adler *et al.* (PHENIX Collaboration), Phys. Rev. D **76**, 051106 (2007).
- [57] A. Adare *et al.* (PHENIX Collaboration), Phys. Rev. D **79**, 012003 (2009).
- [58] S. S. Adler *et al.* (PHENIX Collaboration), Phys. Rev. D **73**, 091102(R) (2006).
- [59] R. D. Ball *et al.*, Nucl.Phys. B **874**, 36 (2013).
- [60] A. Adare *et al.* (PHENIX Collaboration), Phys. Rev. Lett. **103**, 012003 (2009).
- [61] Abelev *et al.*, Phys. Rev. Lett. **100**, 232003 (2008).
- [62] L. Aphecetche et al., Nucl. Instrum. Meth. A **499**, 521 (2003).
- [63] D. de Florian, R. Sassot, M. Stratmann, and W. Vogelsang, Phys. Rev. Lett. **101**, 072001 (2008).
- [64] E. Leader, A. V. Sidorov, and D. B. Stamenov, Phys. Rev. D **82**, 114018 (2010).
- [65] M. Hirai *et al.*, Nucl. Phys. B **813**, 106 (2009).
- [66] D. de Florian, R. Sassot, M. Stratmann, and W. Vogelsang, Phys. Rev. D **80**, 034030 (2009).
- [67] T. A. DeGrand, R. L. Jaffe, K. Johnson, and J. E. Kiskis, Phys. Rev. D **12**, 2060 (1975).
- [68] A. Adare *et. al.* (PHENIX Collaboration), Phys. Rev. D **90**, 012007 (2014).
- [69] L. Adamczyk *et. al.* (STAR Collaboration), Phys. Rev. Lett. **115**, 092002 (2015)

- [70] D. de Florian, R. Sassot, M. Stratmann, and W. Vogelsang, Phys. Rev. Lett. **113**, 012001 (2014).
- [71] E. Leader, A. V. Sidorov, and D. B. Stamenov, Phys. Rev. D **82**, 114018 (2010).
- [72] R. D. Ball *et al.*, Nucl.Phys. B **874**, 36 (2013).
- [73] P. Nilsson, Pad chamber hit reconstruction (2001).
- [74] A. Zelenski *et al.* Nucl. Instrum. Meth. **536(3)**, 248 (2005).
- [75] A. D. Martin, W. J. Stirling, R. S. Thorne, and G. Watt, Eur. Phys. J. C **63**, 189 (2009).
- [76] D. de Florian, R. Sassot, and M. Stratmann, Phys. Rev. D **76**, 074033 (2007).
- [77] R. Sassot (DSSV group), private communication (2015).
- [78] E. C. Aschenauer, R. Sassot, and M. Stratmann, Phys. Rev. D **86**, 054020 (2012).

## Appendix A

### DOUBLE HELICITY ASYMMETRY PLOTS

#### A.1 Spin Pattern Separated Asymmetries Results

There were four spin patterns namely SOOSSOO, OSSOOSS, SSOO and OOSS during the run year of 2013. The following figures show raw  $A_{LL}$  for each of the spin patterns as a function of run index for different crossings, signal and background regions and for different  $p_T$  bins. The results from each  $p_T$  bin data is fit with constant to get the average value of  $A_{LL}$ .

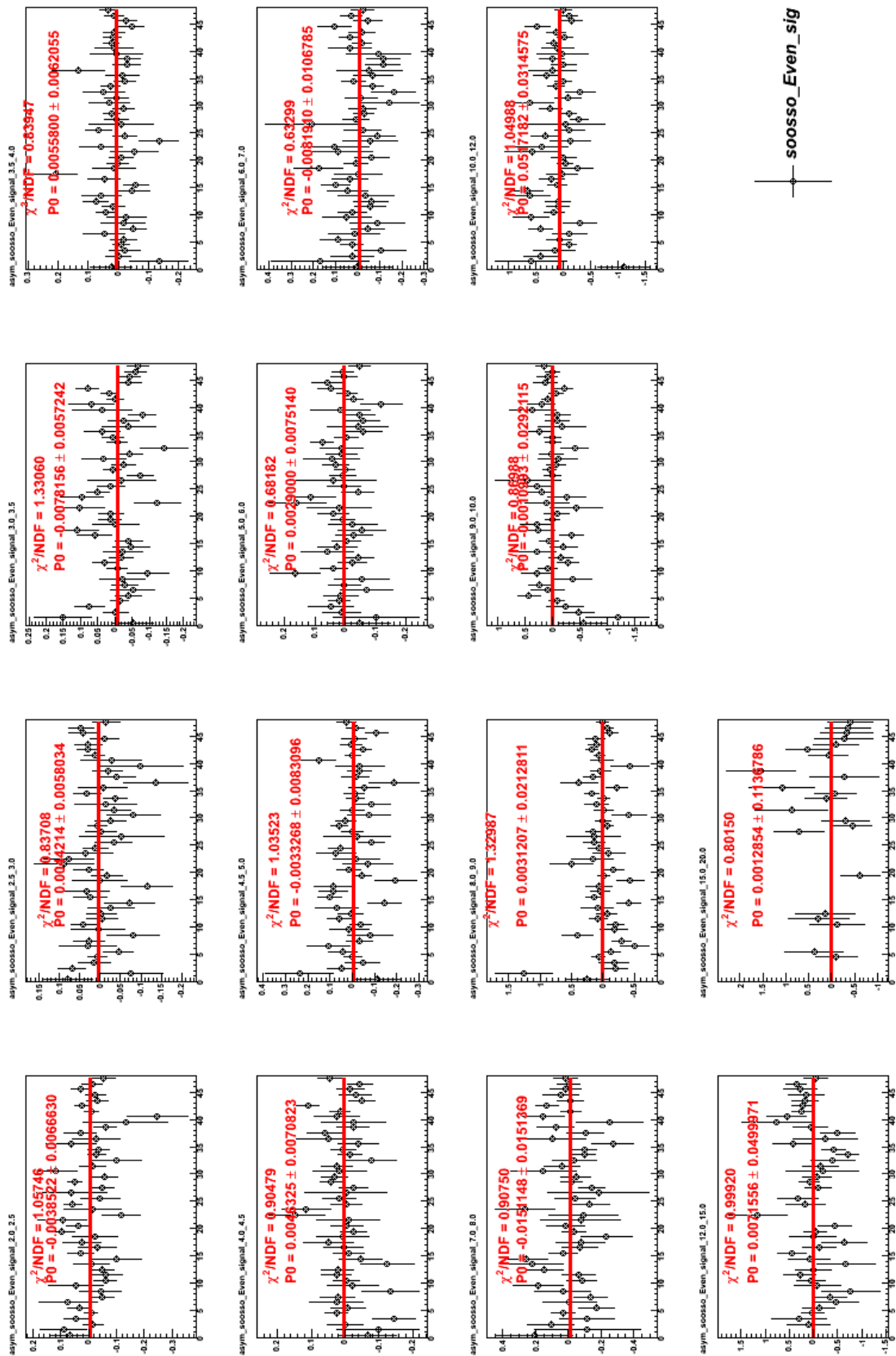


Figure (A.1) Double spin asymmetry for spin patterns SOOSSO and even crossing, signal region.

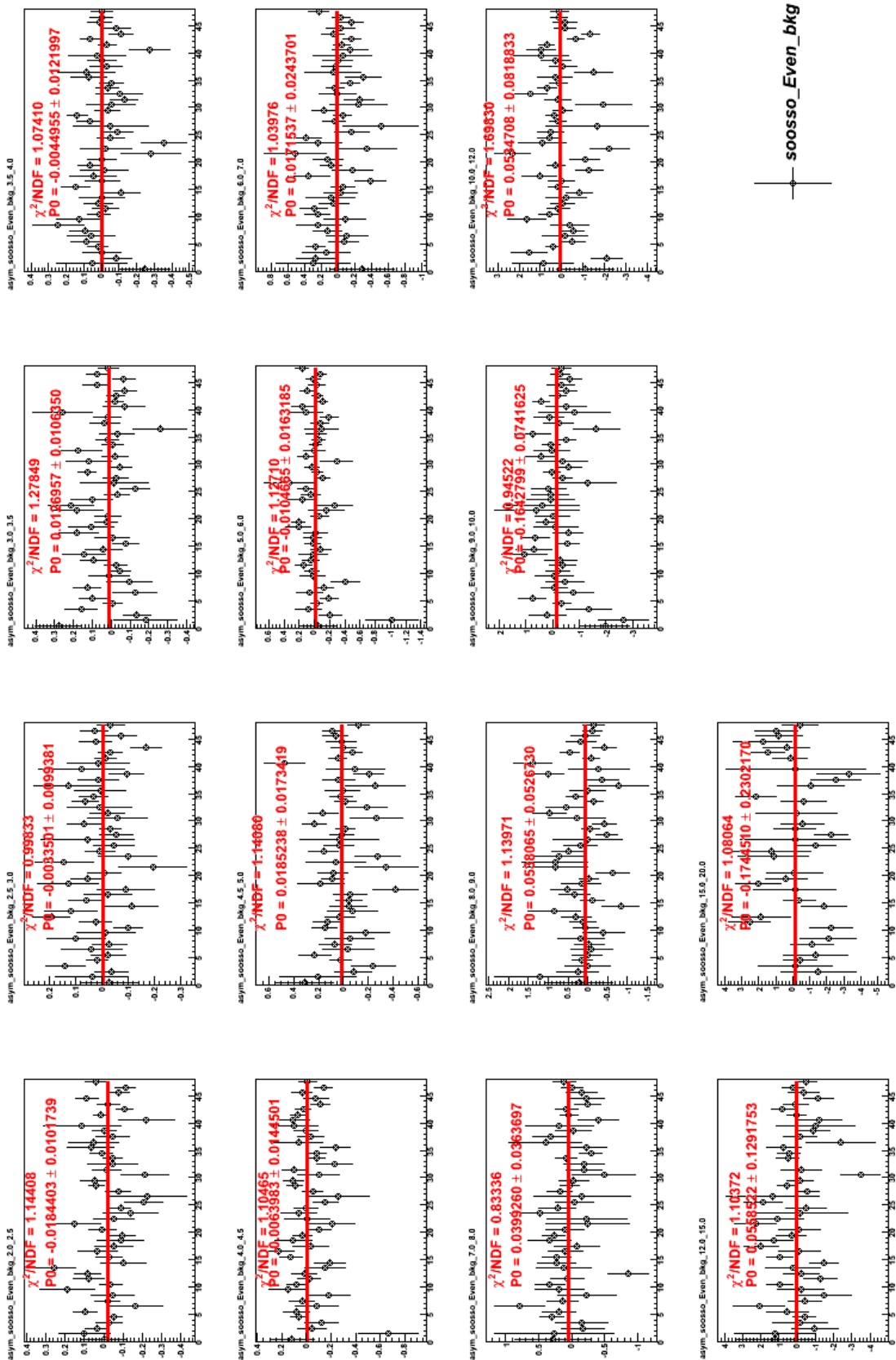


Figure (A.2) Double spin asymmetry for spin patterns SOOSSO and even crossing, background region.

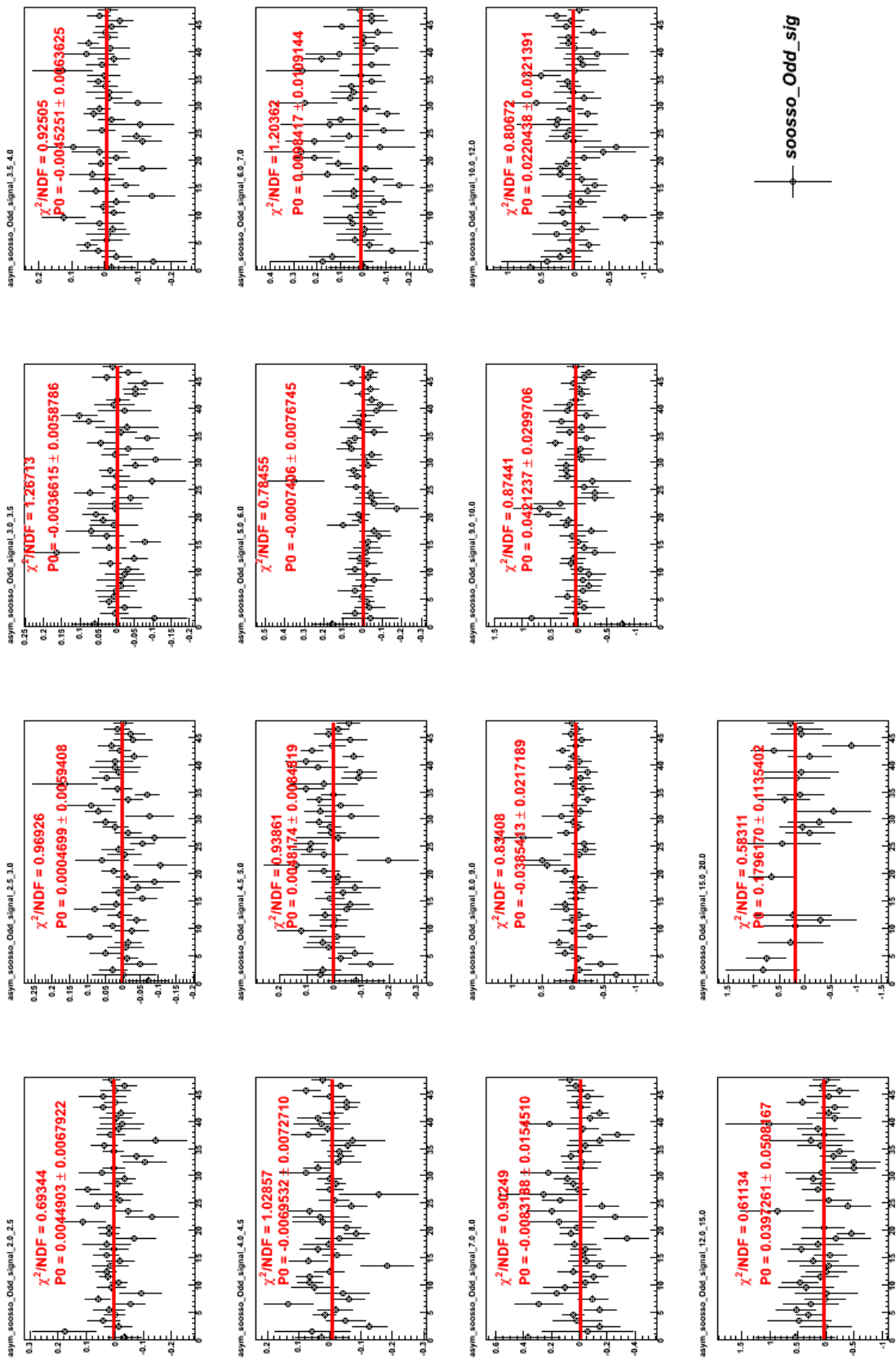


Figure (A.3) Double spin asymmetry for spin patterns SOOSSO and odd crossing, signal region.

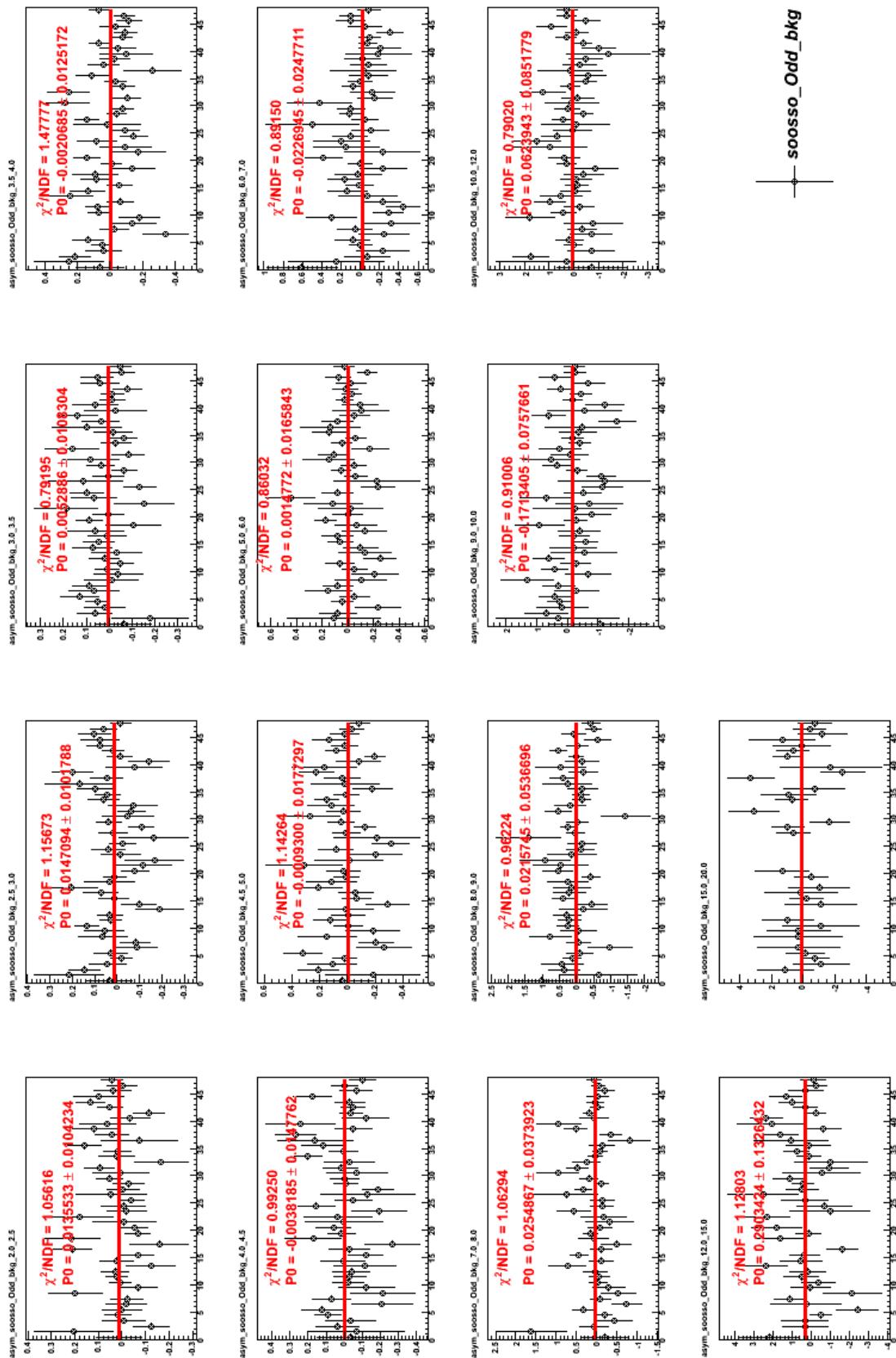


Figure (A.4) Double spin asymmetry for spin patterns SOOSSO and odd crossing, background region.

## A.2 Trigger Separated $A_{LL}$ Results

As a cross-check, the spin pattern separated  $A_{LL}$  for different triggers used in this analysis are presented in following figures. Here,  $A_{LL}$  results as a function of run index for different spin patterns, different triggers and different crossing for different  $p_T$  bins are shown.

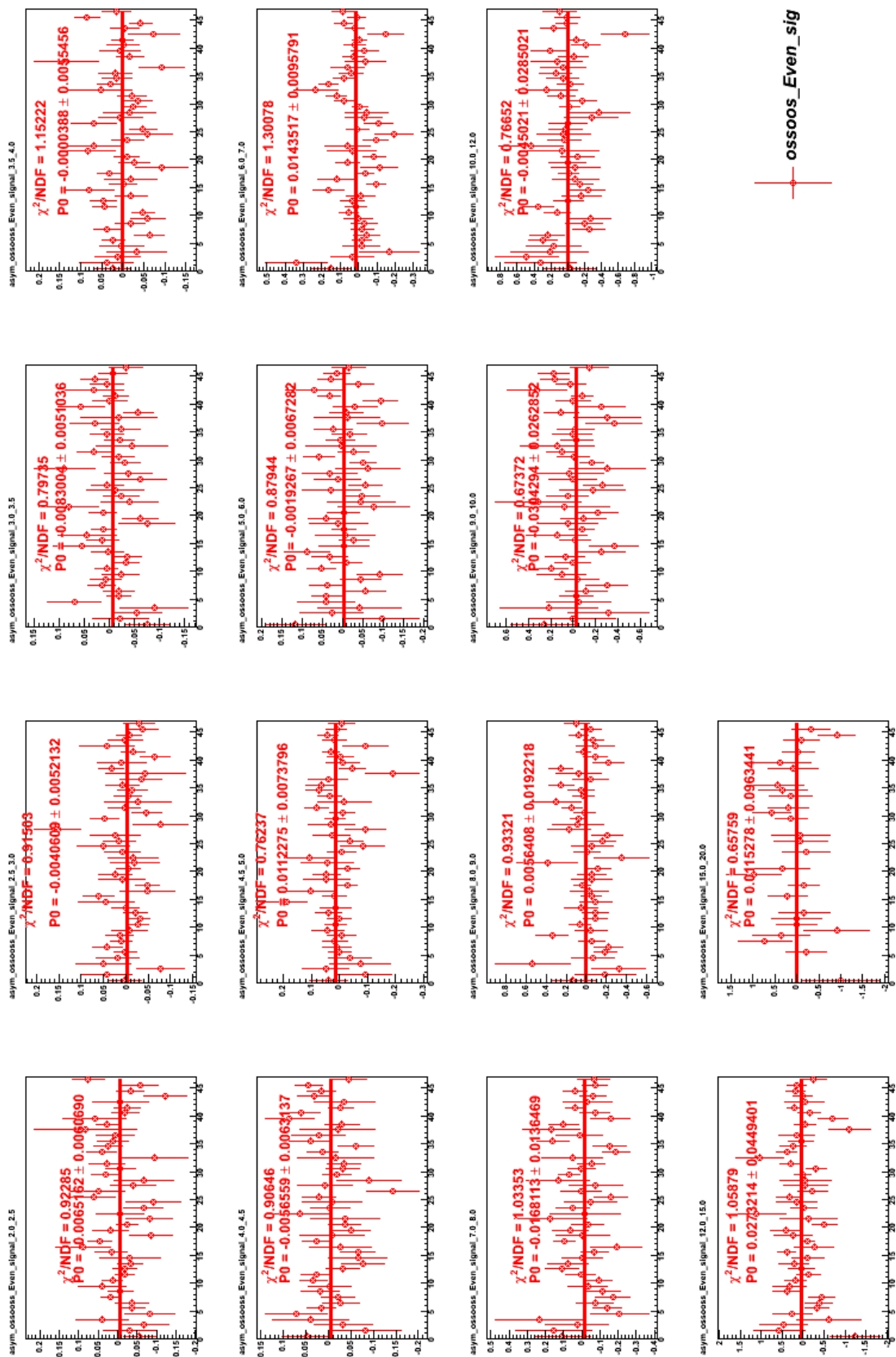


Figure (A.5) Double spin asymmetry for spin patterns OSOOOSS and even crossing, signal region.

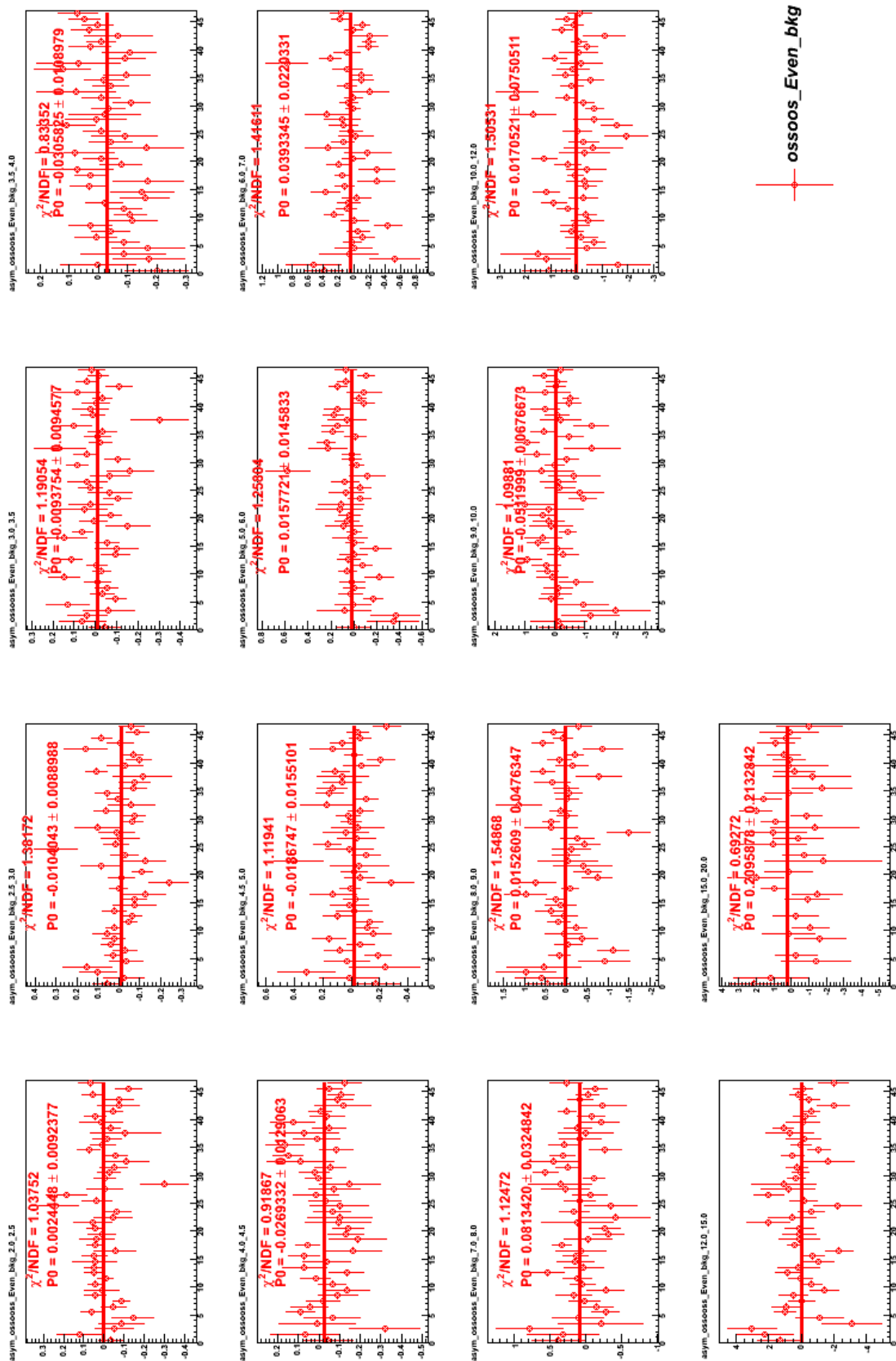


Figure (A.6) Double spin asymmetry for spin patterns OSSOOSS and even crossing, background region.

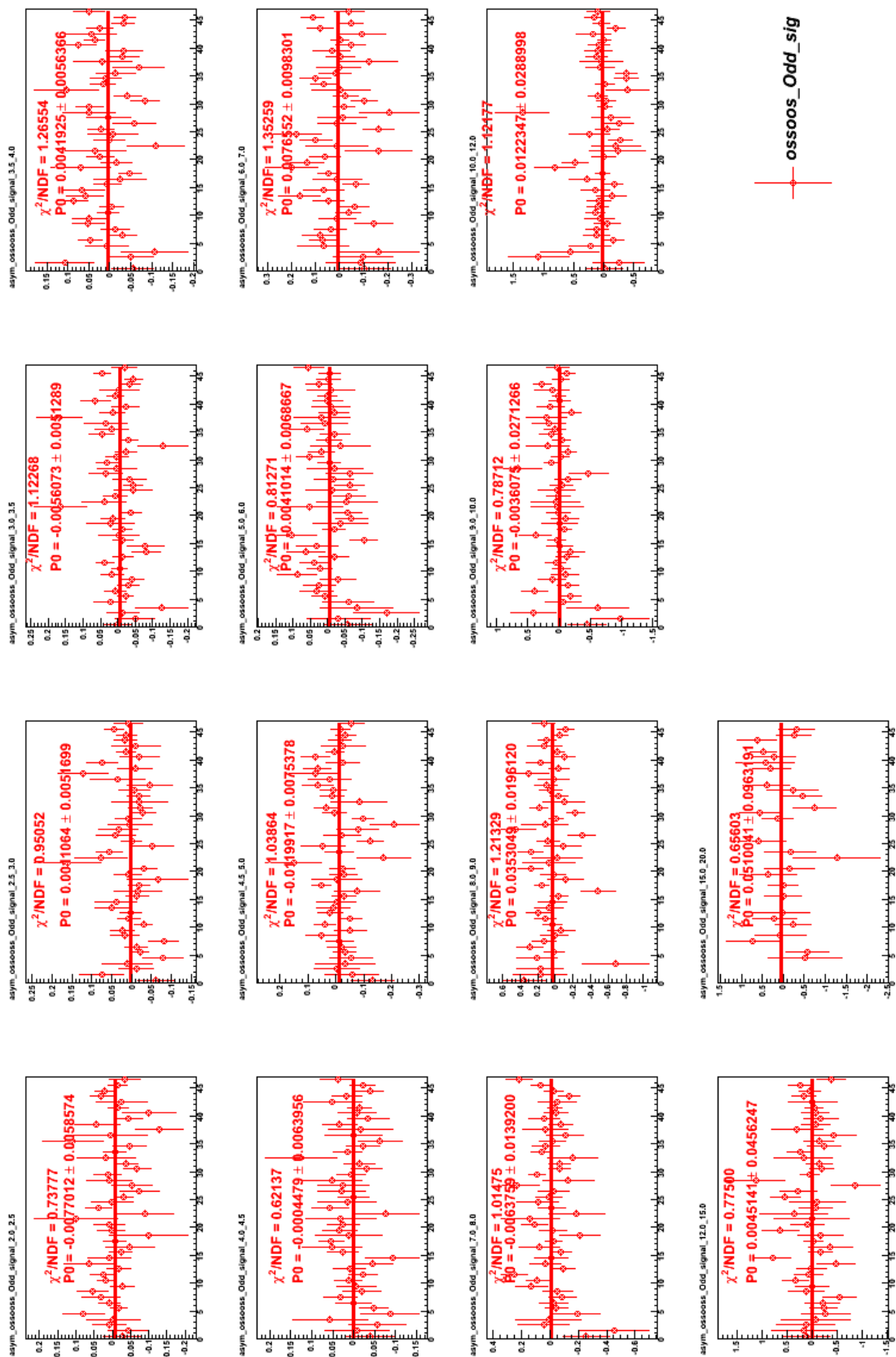


Figure (A.7) Double spin asymmetry for spin patterns OSSOOSS and odd crossing, signal region.

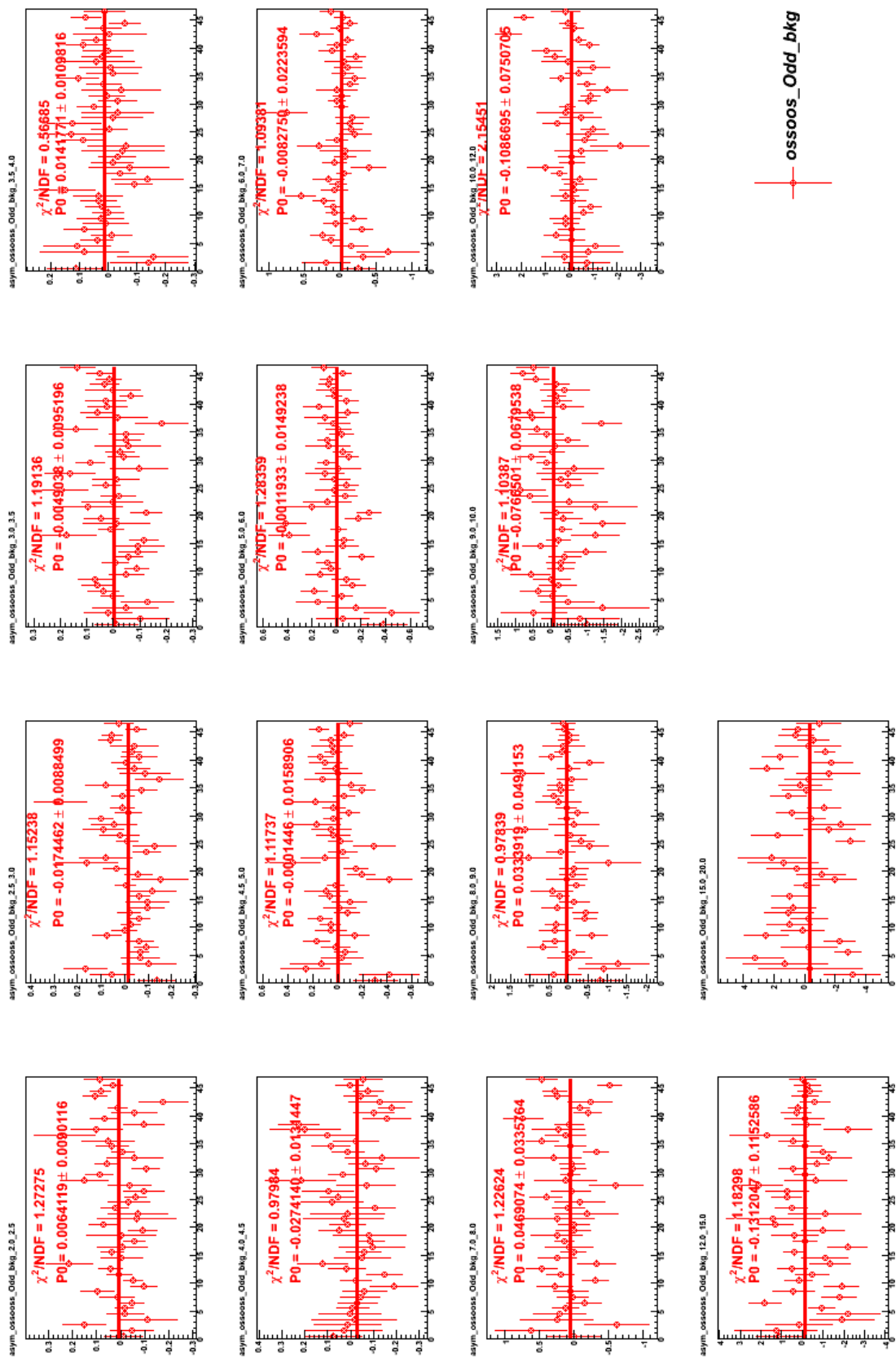


Figure (A.8) Double spin asymmetry for spin patterns OSOOOS and odd crossing, background region.

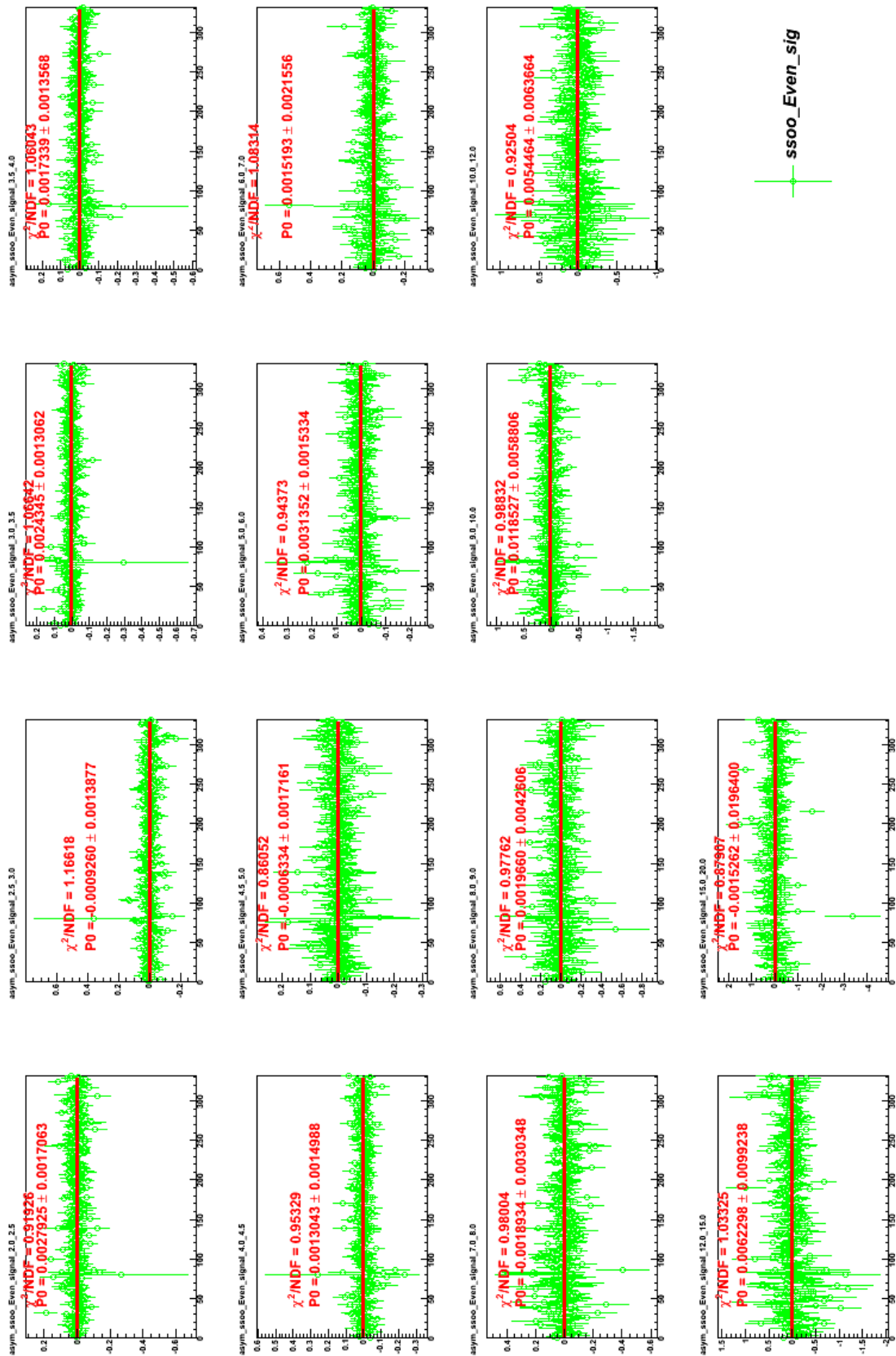


Figure (A.9) Double spin asymmetry for spin patterns SSOO and even crossing, signal region.

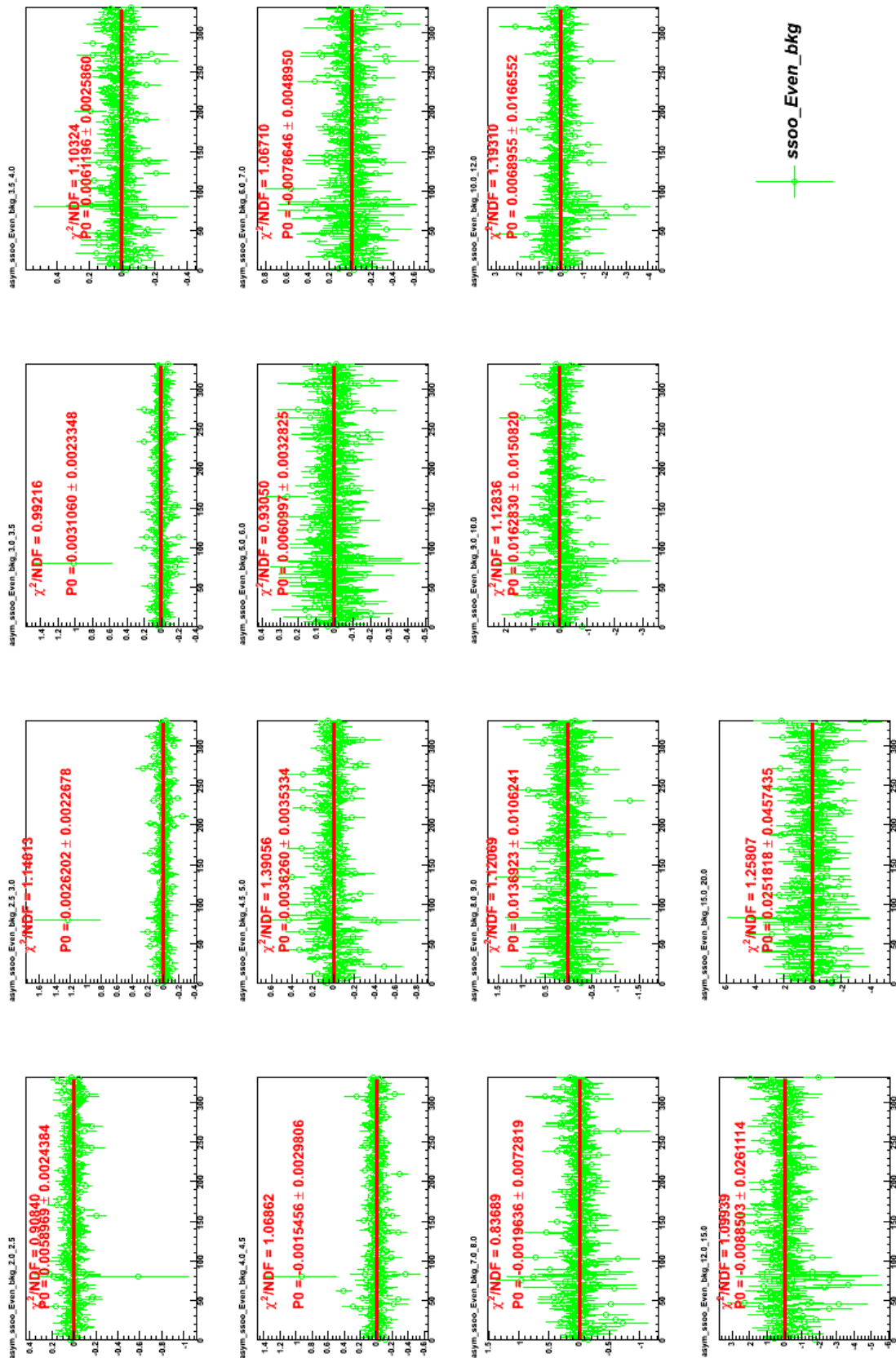


Figure (A.10) Double spin asymmetry for spin patterns SSOO and even crossing, background region.

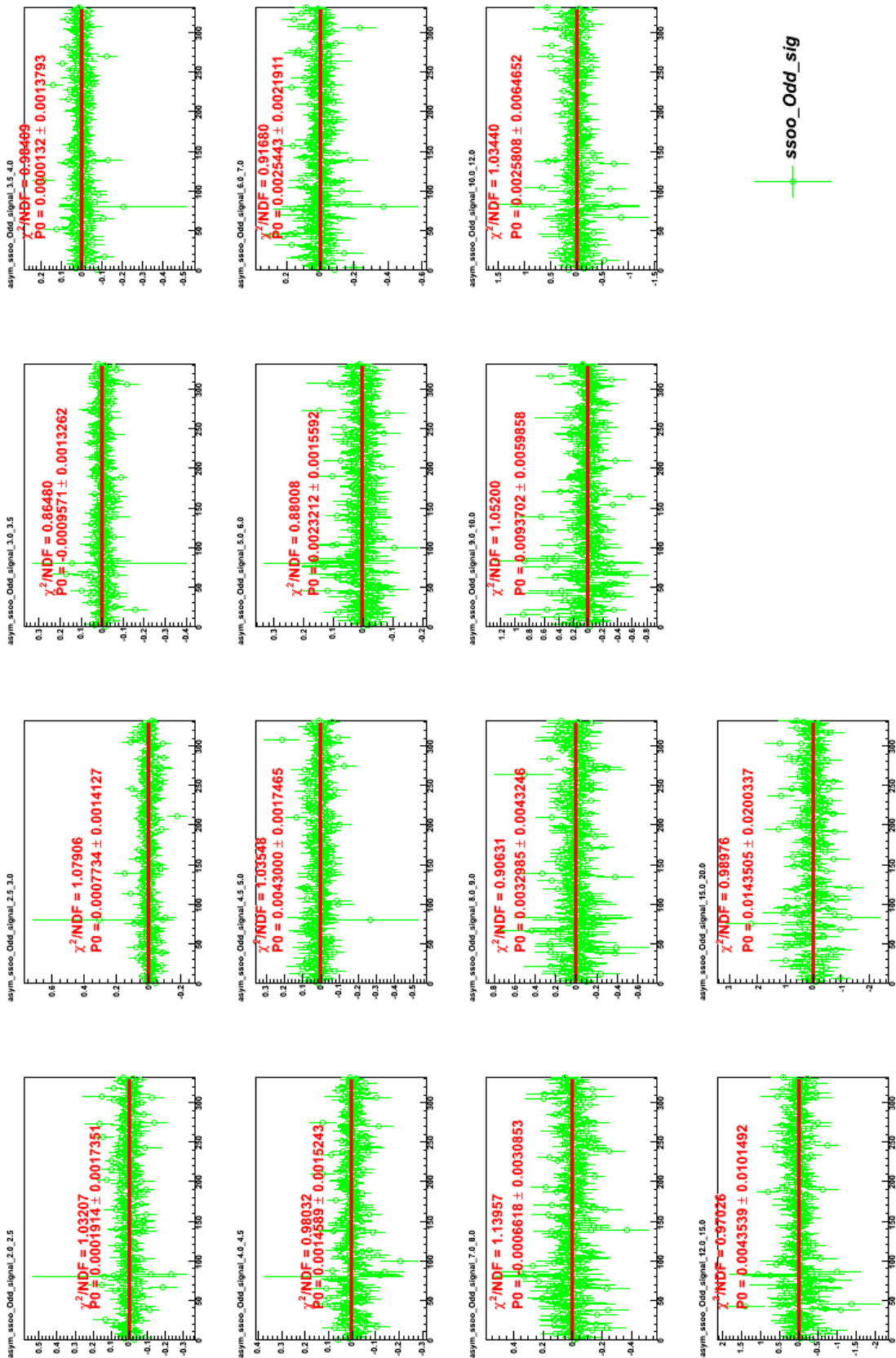


Figure (A.11) Double spin asymmetry for spin patterns SSOO and odd crossing, signal region.

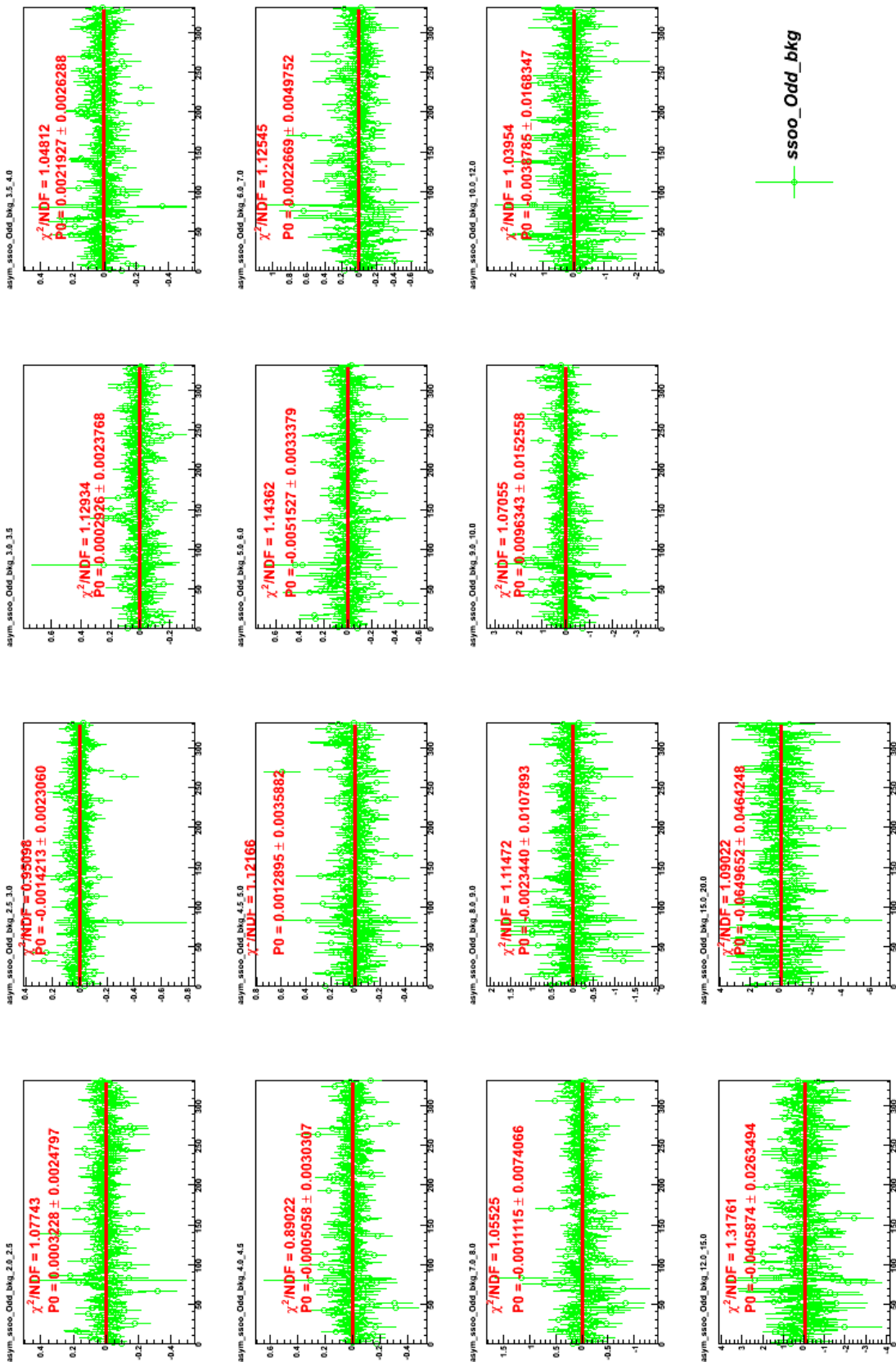


Figure (A.12) Double spin asymmetry for spin patterns SSOO and odd crossing, background region.

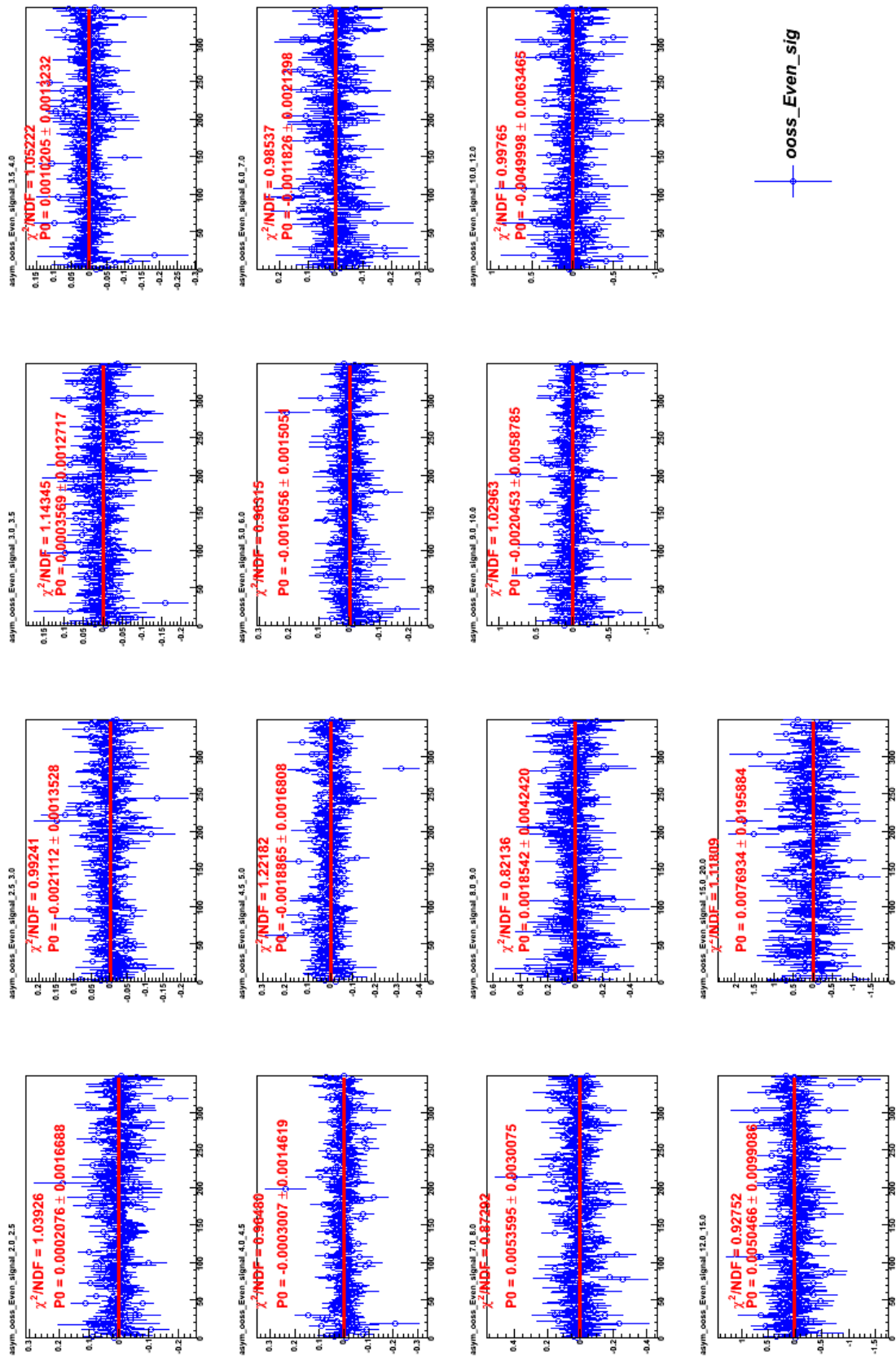


Figure (A.13) Double spin asymmetry for spin patterns OOSS and even crossing, signal region.

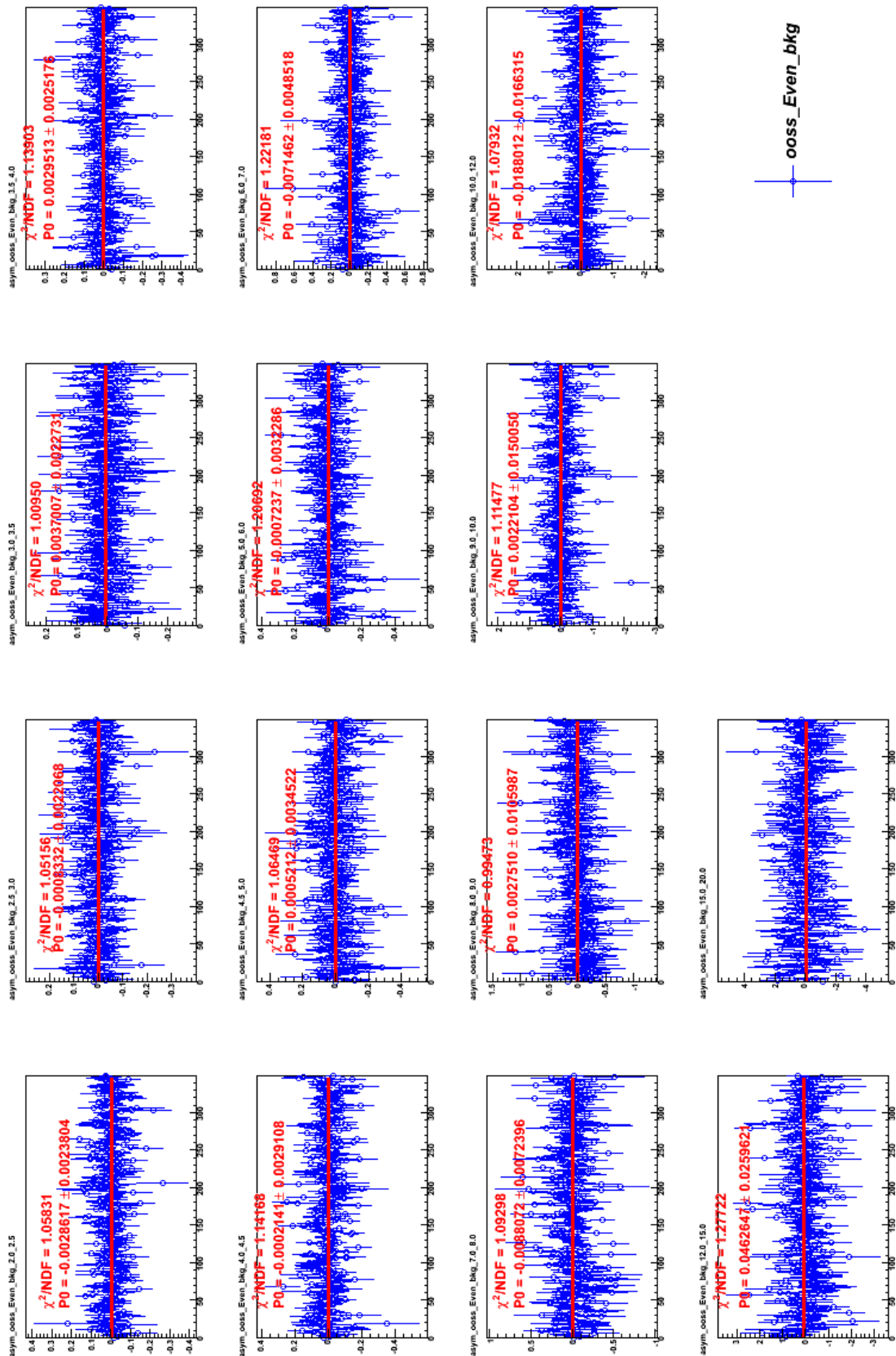


Figure (A.14) Double spin asymmetry for spin patterns OOSS and even crossing, background region.

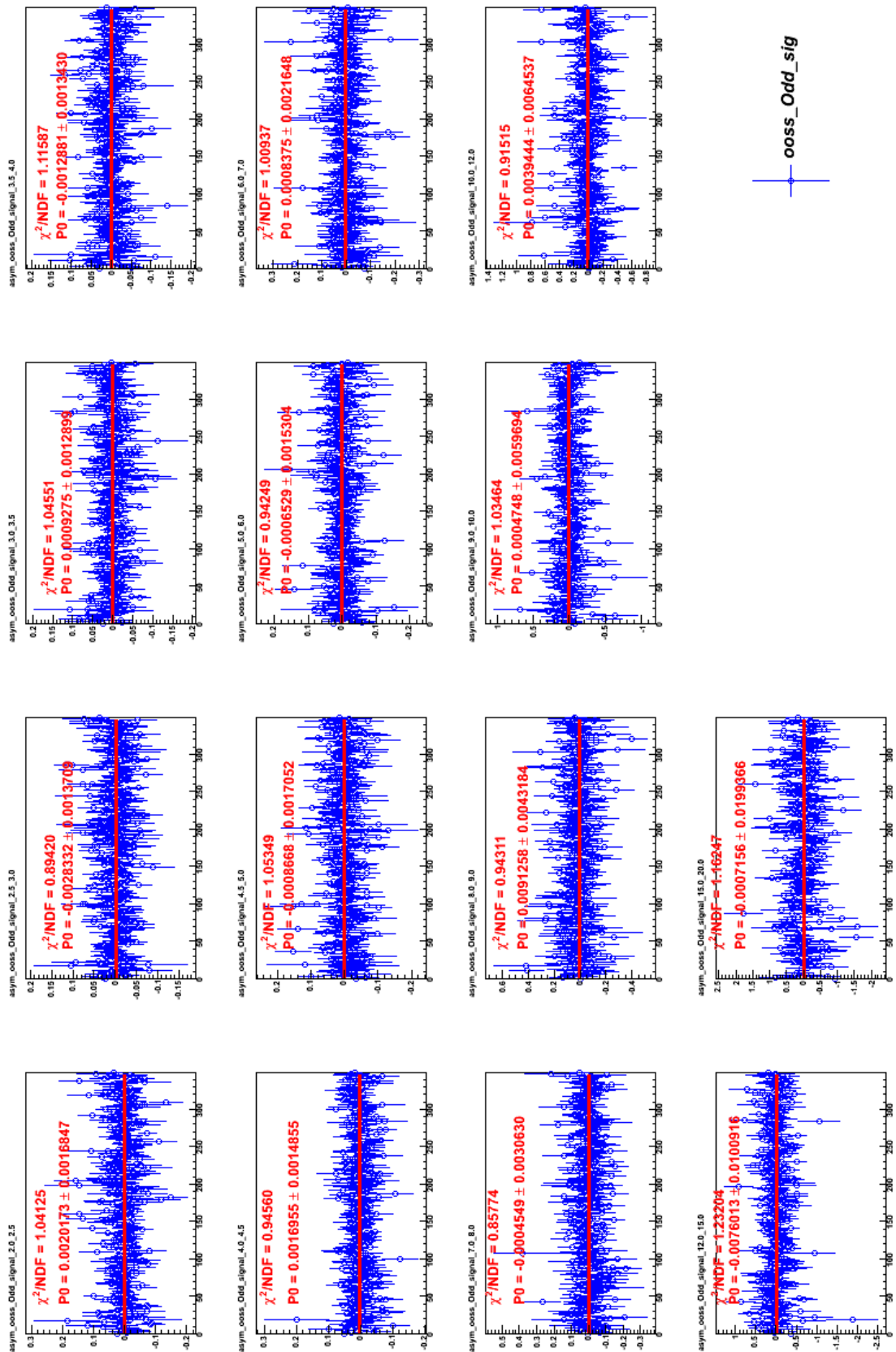


Figure (A.15) Double spin asymmetry for spin patterns OOSS and odd crossing, signal region.

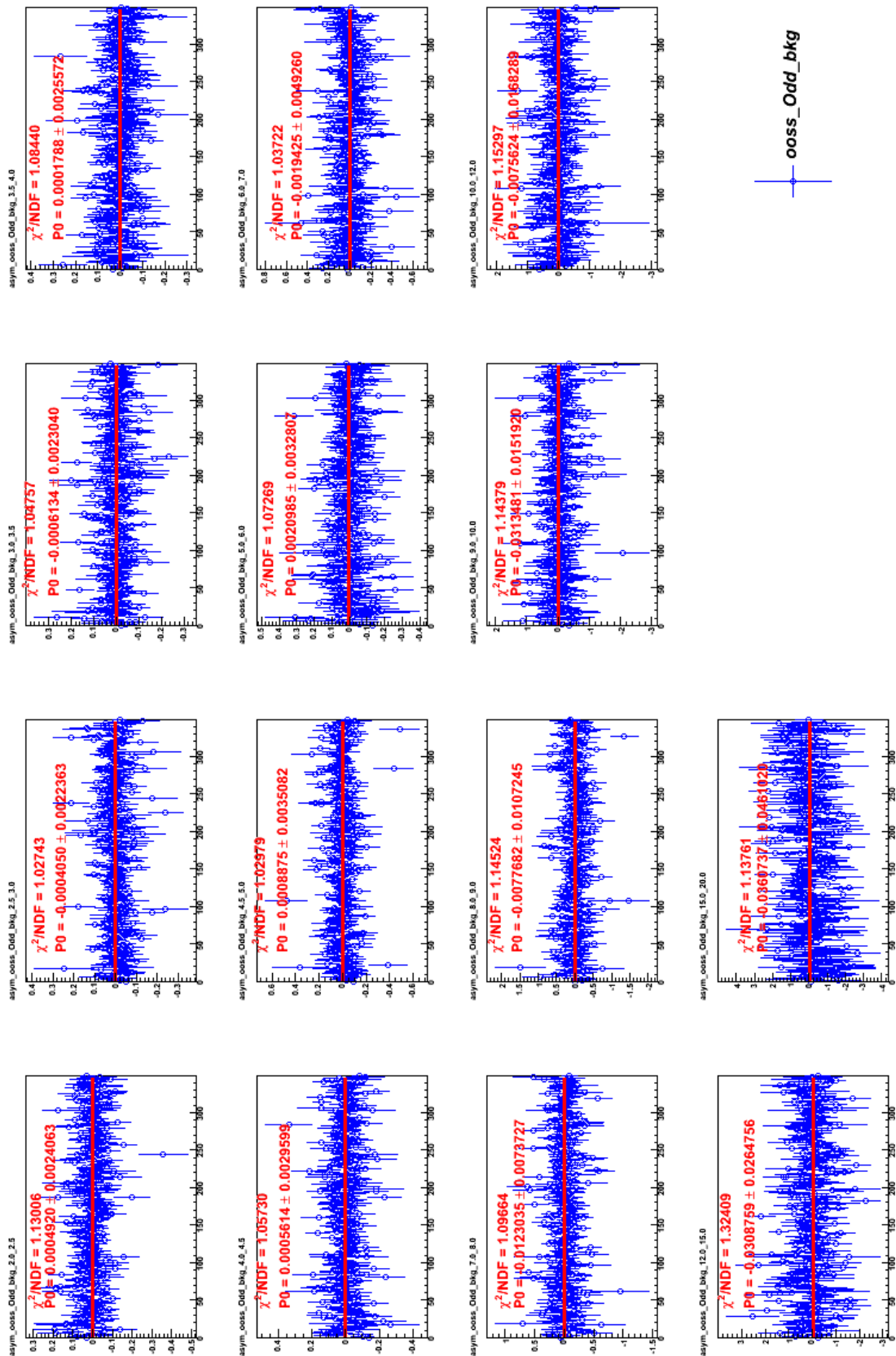


Figure (A.16) Double spin asymmetry for spin patterns OOSS and odd crossing, background region.

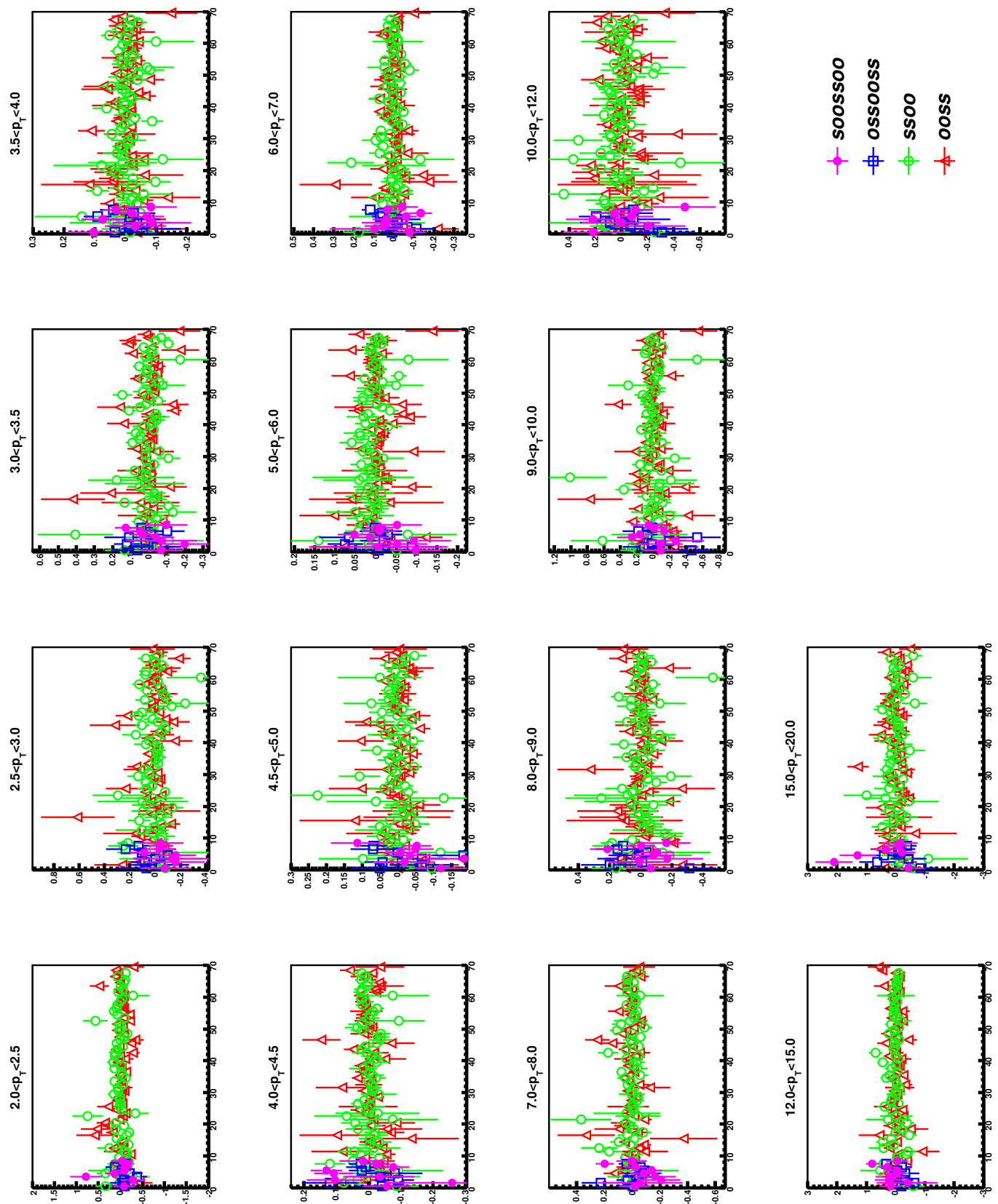


Figure (A.17) Double spin asymmetry for different spin patterns for 4x4a trigger and even crossing.

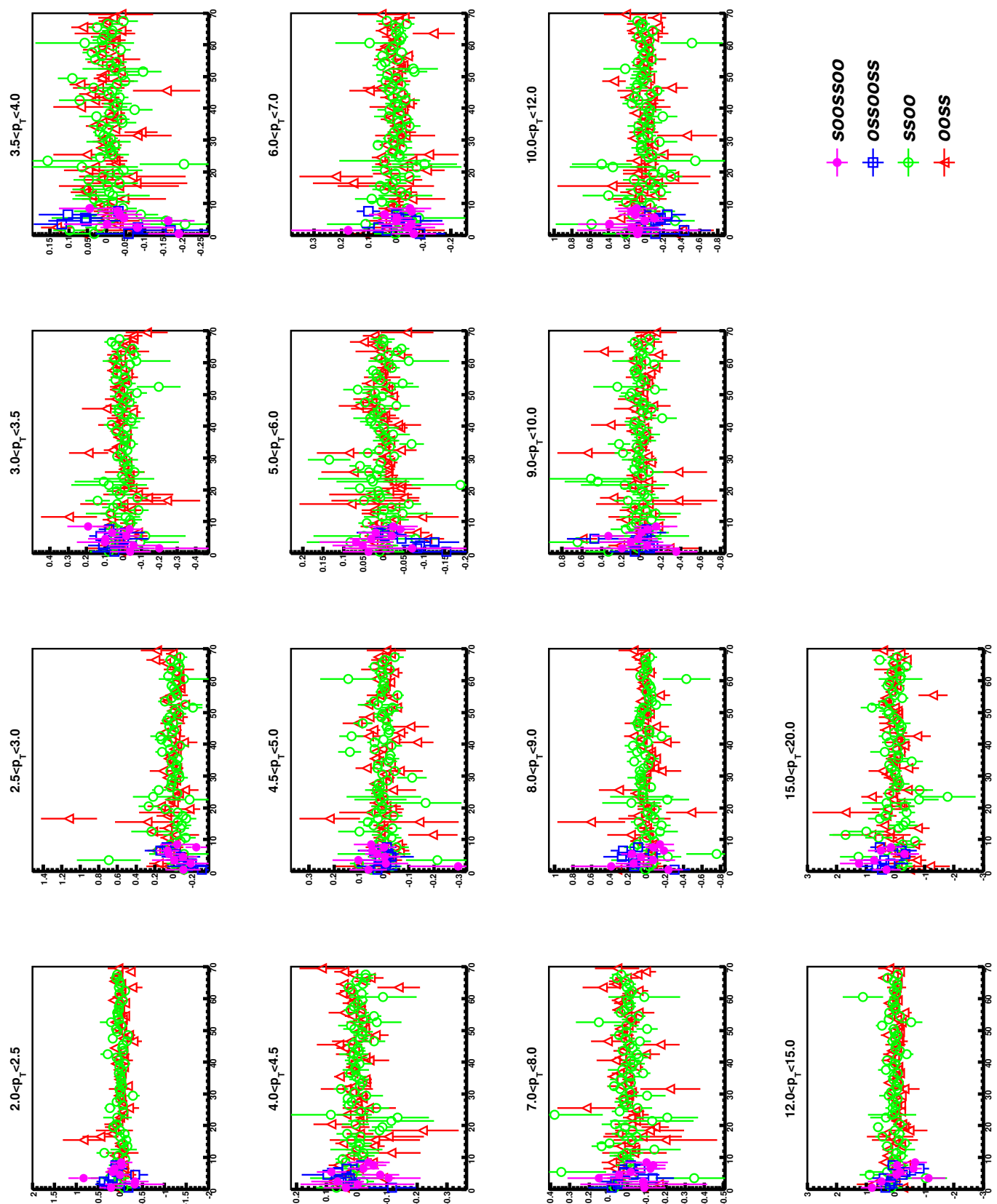


Figure (A.18) Double spin asymmetry for different spin patterns for 4x4a trigger and odd crossing.

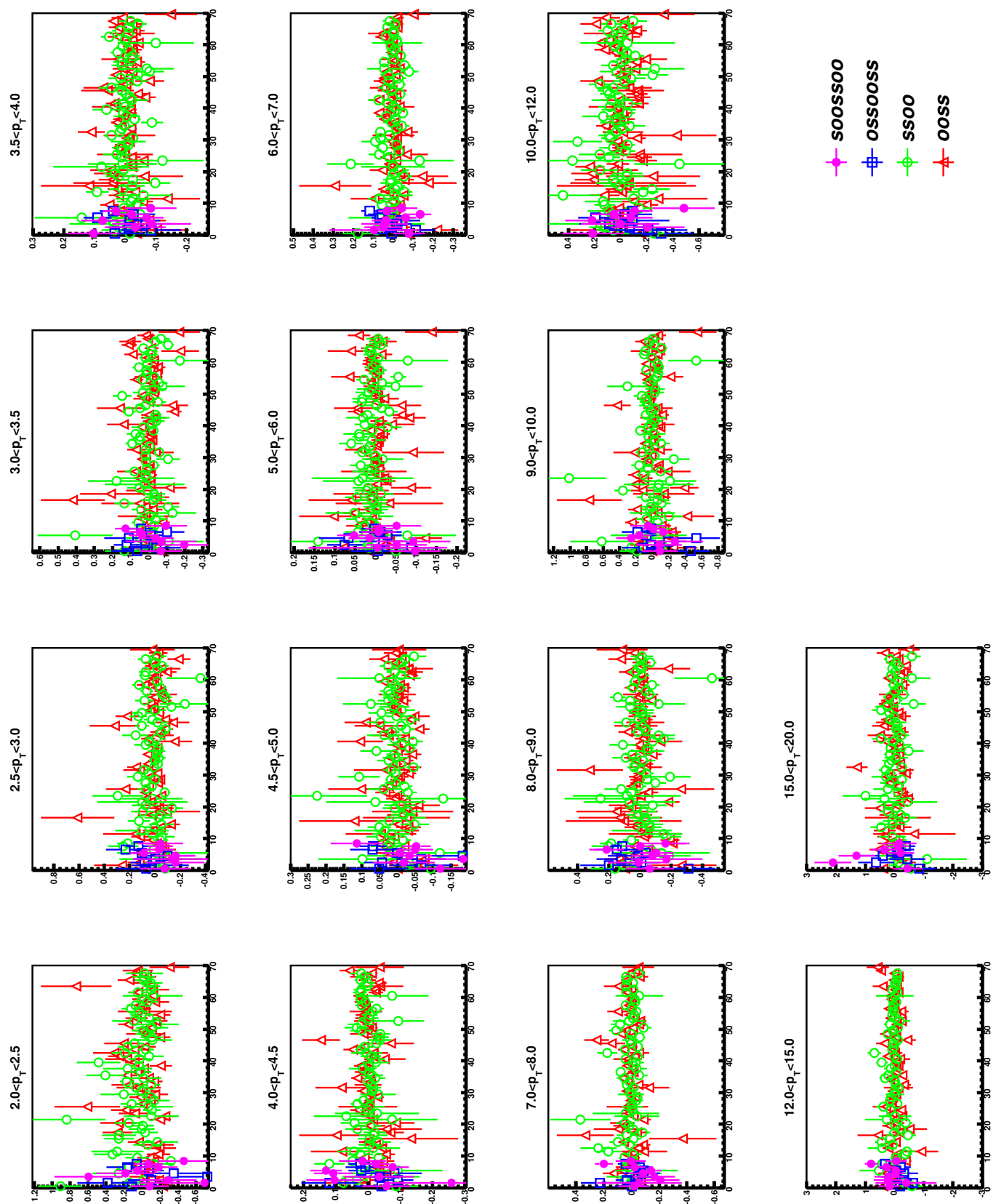


Figure (A.19) Double spin asymmetry for different spin patterns for 4x4b trigger and even crossing.

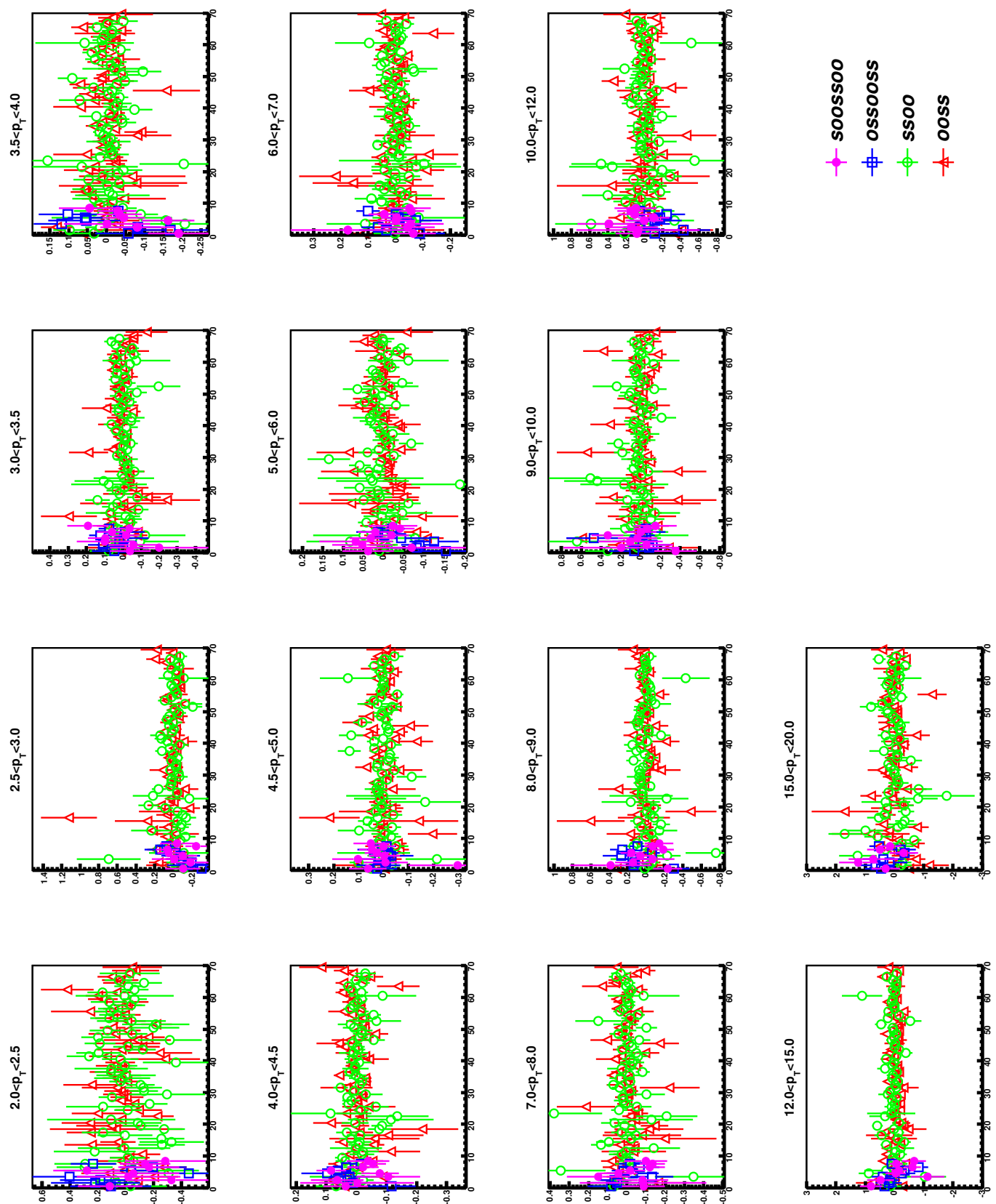


Figure (A.20) Double spin asymmetry for different spin patterns for 4x4b trigger and odd crossing.

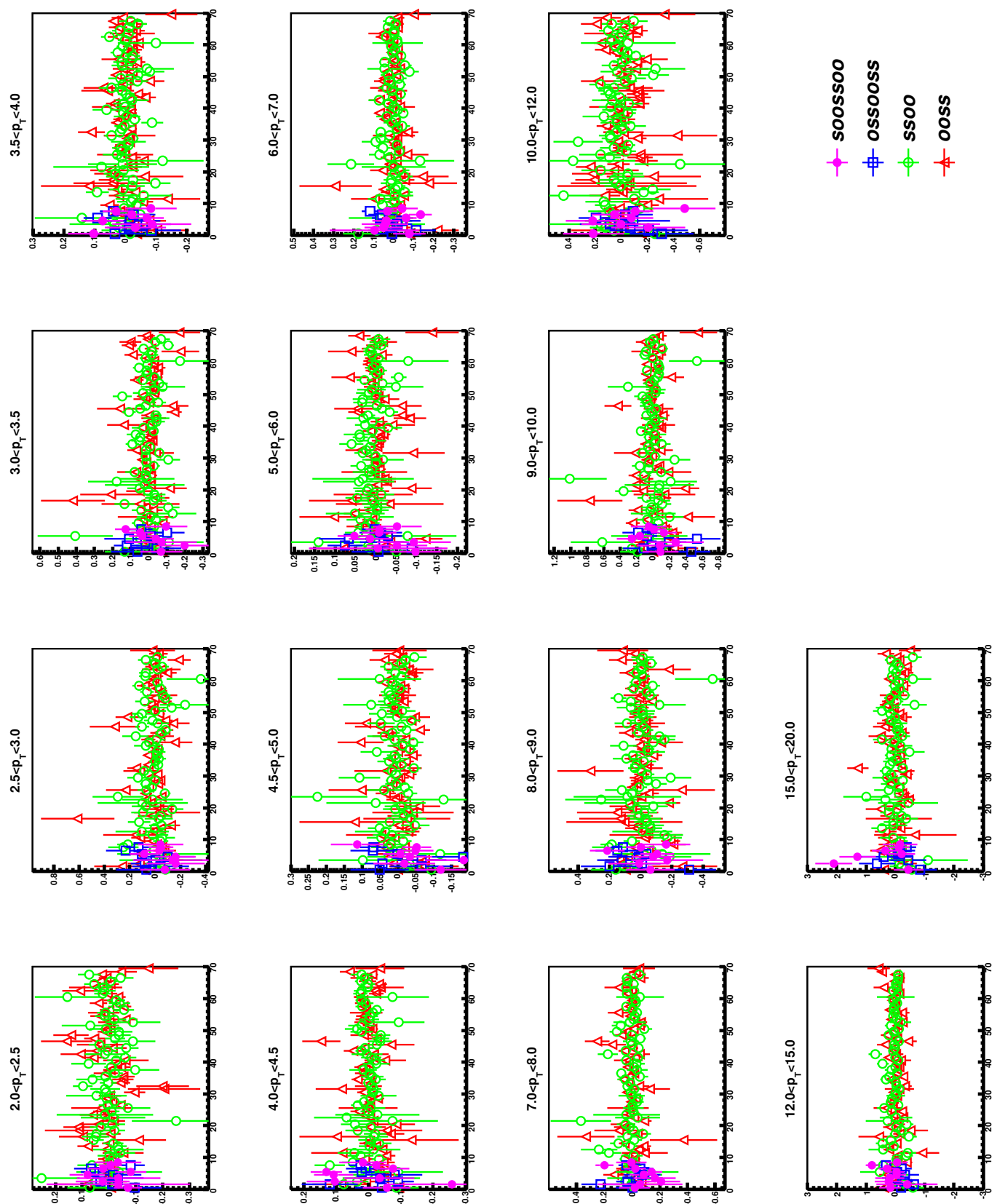


Figure (A.21) Double spin asymmetry for different spin patterns for 4x4c trigger and even crossing.

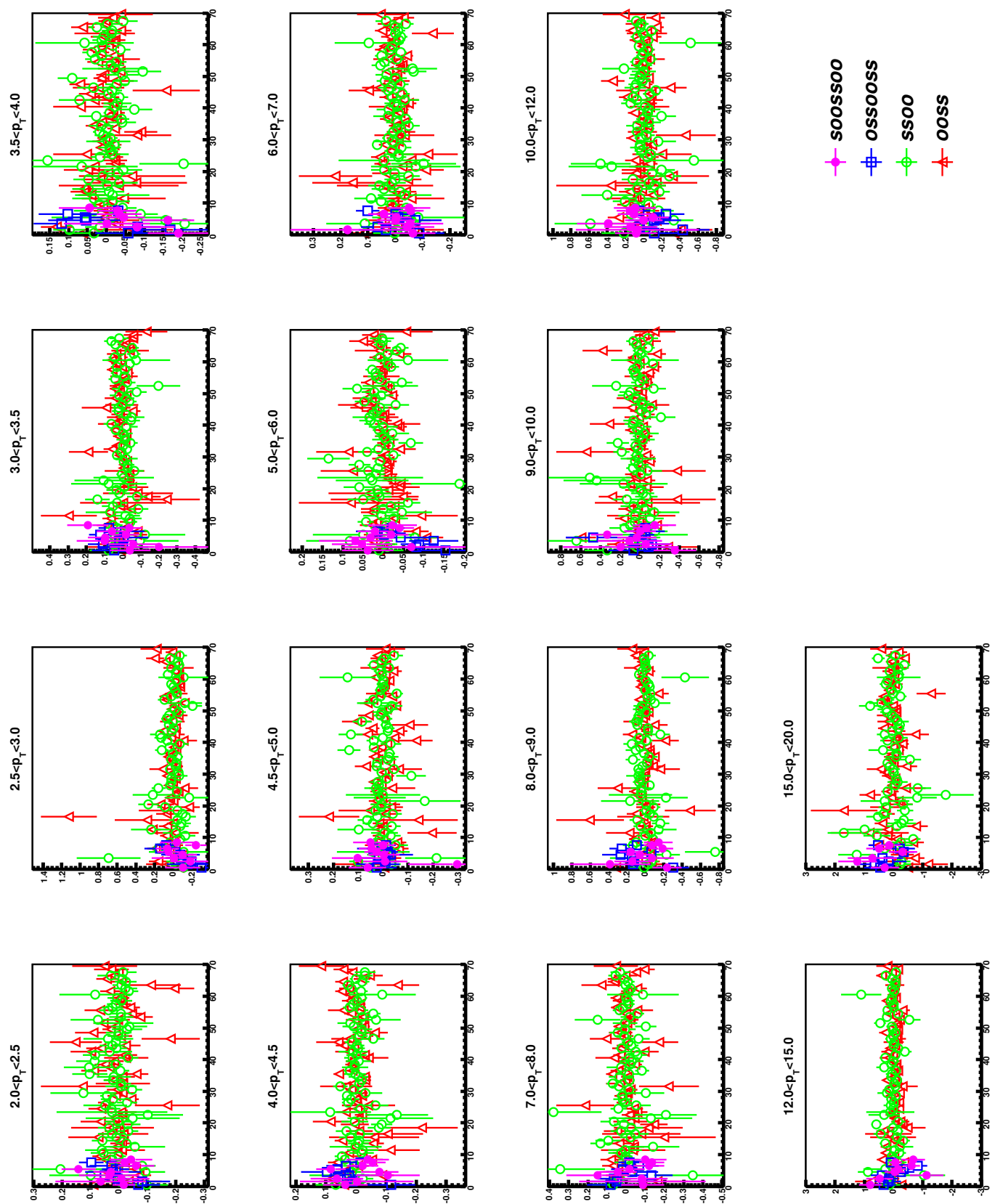


Figure (A.22) Double spin asymmetry for different spin patterns for 4x4c trigger and odd crossing.